

Functionalization of Graphene and Its Applications

Submitted in partial fulfillment of the requirements for the degree of

Doctor of Philosophy

by

Robin Singla

(Roll No. 134076016)

Under the guidance of

Prof. Anil Kottantharayil



Department of Electrical Engineering
Indian Institute of Technology Bombay

28th August, 2020

Dedicated to
my Family
and Teachers

Thesis Approval

This thesis entitled

Functionalization of Graphene and Its Applications

By

Robin Singla

(Roll No. 134076016)

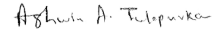
is approved for degree of

Doctor of Philosophy



Prof. Deleep Nair

(Examiner)



Prof. Ashwin Tulapurkar

(Examiner)



Prof. Anil Kottantharayil

(Supervisor)



Prof. Prabhu N

(Chairman)

Date: 01/02/2021

IIT Bombay

Declaration

I declare that this written submission represents my ideas in my own words and where others' ideas or words have been included, I have adequately cited and referenced the original sources. I also declare that I have adhered to all principles of academic honesty and integrity and have not misrepresented or fabricated or falsified any idea/data/fact/source in my submission. I understand that any violation of the above will be cause for disciplinary action by the Institute and can also evoke penal action from the sources which have thus not been properly cited or from whom proper permission has not been taken when needed.

ROBIN SINGLA
Roll No. 134076016
IIT BOMBAY

28th, August 2020.

Abstract

The aim of the thesis is graphene functionalization, and study of the changes in electrical, magnetic, optical, chemical and surface properties of graphene, and try to develop applications based on functionalized graphene.

In this pursuit, functionalization of chemical vapor deposited (CVD) monolayer graphene and exfoliated graphene is discussed. Using chemical and catalytic approach, hydroxyl functionalities (-OH) have been added covalently by treating graphene with hydrogen peroxide (H_2O_2). UV assisted and catalytic decomposition of H_2O_2 helps in producing hydroxyl-containing groups which are attached covalently on graphene surface. The chemical composition and structural changes were studied by X-ray Photoelectron Spectroscopy (XPS) and Raman spectroscopy. Graphene field effect transistors were fabricated using photo-lithography. Current-voltage characteristics of functionalized graphene shows p-doping of CVD graphene without much degradation in charge carrier mobility. Hydroxyl functionalization of exfoliated graphene helps in deposition of high-K dielectric Al_2O_3 by atomic layer deposition (ALD). For ALD of Al_2O_3 on graphene it is necessary to have -OH termination on its surface. Pristine graphene don't have -OH termination and hence ALD of Al_2O_3 is not possible on pristine graphene. Hydroxyl functionalization also changes optical properties of graphene and we have demonstrated UV sensing by hydroxyl functionalized graphene. Graphene became chemically active after functionalization and shows gas sensing property. -OH functionalized graphene was used for sensing ammonia and hydrogen sulfide.

Monolayer of CVD graphene was doped with nitrogen which make it ferromagnetic in nature. CVD graphene was first functionalized with hydroxyl groups by treating with

H_2O_2 in the presence of UV light and then annealed in ammonia to dope it with nitrogen. Magnetization measurements showed ferromagnetic hysteresis loop at low temperatures with a coercivity of 222 Oe at 2 K. We also investigated the effect of change in angle of applied magnetic field on anisotropic magnetoresistance effect (AMR) in the doped CVD graphene device. Graphene shows positive AMR for temperatures from 2 K to 50 K, negative AMR at 100 K and 150 K, and no AMR for temperatures higher than 150 K. A maximum AMR of 0.92% was observed at 2 K for in-plane magnetic field of 30 kOe. Electron Spin Resonance (ESR) spectroscopy shows resonance in nitrogen doped graphene which supports our hypothesis of availability of free electron as a reason of magnetism in graphene after doping. Magnetic Force Microscopy (MFM) also confirmed magnetization in nitrogen doped graphene. The process introduced for nitrogen doping of graphene with attendant magnetism could pave the way for the applications of graphene in spintronics and other devices.

Acknowledgements

I thank my guide Prof. Anil Kottantharayil for his valuable mentorship throughout the Ph. D. and giving me a topic related to graphene, which would really help in my future career. Without his mentorship it would never been possible to complete Ph. D. work. He taught me how to approach a problem and how to benchmark the results. I also thank my RPC members, Prof. Ashwin Tulapurkar and Prof. Saurabh Lodha, for their valuable suggestions during the annual progress seminars.

I acknowledge IIT Bombay Nanofabrication Facility (IITBNF), Electrical Engineering Department, IIT Bombay where all experimental work of this thesis was carried out and staff of IITBNF for their help in operating various processing and characterization tools. I would like to thank, Center of Excellence in Nanoelectronics (CEN) phase-II and Nanoelectronics Network for Research and Application (NNetRA) for supporting my Ph.D. fellowship. I acknowledge Central Facility in the Center for Research in Nano Technology and Science (CRNTS), IIT Bombay for Raman spectroscopy, Sophisticated Analytic Instrument Facility (SAIF) ESR characterization and Industrial Research and Consultancy Centre (IRCC), IIT Bombay central facilities for SQUID and AFM characterization.

I would like to thank all my group members, Dr. Abhishek Misra, Preamsai, Dr. Poonam Jangid, Dr. Sanchar Acharaya, Dr. Trupti Warang, Dawuth Pathan and Shahul Nath, for their support and help in conducting experiments and for discussions. I acknowledge Prof. Ashwin Tulapurkar for his inputs for conducting magnetization experiments and his student Mr. Ambika Shankar Shukla for the support while operating SQUID and PPMS tools.

I am also thankful to IIT Bombay and Electrical Engineering Department of IIT Bombay for giving me admission in Ph.D. program in this institute. I am also thankful to Prof. Anil Kottantharayil and Prof. Abhay Karandikar for helping me to defer my Ph. D. admission from June, 2013 to January, 2014.

In the last but not the least, I would like to thank my parents and my wife for their unconditional support through out the Ph. D. Without their moral support it would have been difficult to go through the long journey of Ph. D.

Robin Singla

Contents

Abstract	ii
Acknowledgements	iv
List of Figures	xi
List of Tables	xix
List of Symbols	xx
List of Abbreviations	xxi
1 Introduction	1
1.1 Motivation	2
1.2 Thesis Organization	3
2 Literature Review	5
2.1 Introduction	5
2.2 Mechanism of Graphene Functionalization	5
2.3 Types of Graphene Functionalization	7
2.3.1 Hydrogenation	7
2.3.2 Oxidation	8

2.3.3	Fluorination	10
2.3.4	Hydroxylation	10
2.3.5	Other Organic Molecules	10
2.4	Techniques for Graphene Functionalization	11
2.4.1	Wet Chemical Reactions	11
2.4.2	Plasma Exposure	11
2.4.3	Nanolithography Using AFM	12
2.5	Characterization of Functionalized Graphene	13
2.5.1	Raman Spectroscopy	14
2.5.2	X-ray Photoelectron Spectroscopy (XPS)	15
2.6	Applications of Functionalized Graphene	16
2.6.1	Electronic and Optoelectronic Applications	16
2.6.2	Applications in Magnetism	18
2.6.3	Chemical Applications	19
2.6.4	Biomedical Applications	19
2.6.5	Summary	20
3	Functionalization of Graphene	21
3.1	Graphene Sample Preparation	21
3.1.1	CVD graphene	22
3.1.2	Exfoliated Graphene	24
3.2	Functionalization of Graphene with Hydroxyl Groups and Characterization	24
3.2.1	Thermal Treatment in H ₂ O ₂	24
3.2.2	UV Assisted Photo-chemical Method	29
3.3	Summary and Conclusions	38

4	Electrical Applications of Functionalized Graphene	39
4.1	Workfunction Engineering	39
4.2	Atomic Layer Deposition of Al ₂ O ₃	42
4.3	Graphene Field Effect Transistors (GFETs)	44
4.3.1	GFET Fabrication Process Flow	44
4.3.2	Electrical Characterization of Functionalized Graphene FETs	48
4.4	Improvement of Contact Resistance	54
4.4.1	Transfer Length Measurement (TLM)	54
4.4.2	Dependence on Metal-Graphene Overlap Length	57
4.5	Summary and Conclusions	59
5	Ferromagnetism in Functionalized Graphene	60
5.1	Nitrogen Doping of Graphene	60
5.2	Magnetization Measurement	62
5.2.1	Superconducting Quantum Interference Device (SQUID) Magnetometer	62
5.2.2	Magnetic Force Microscopy (MFM)	66
5.2.3	Electron Spin Resonance (ESR)	68
5.3	Anisotropic Magnetoresistance (AMR)	69
5.4	Discussions	73
5.5	Summary and Conclusions	74
6	Sensors Based on Functionalized Graphene	76
6.1	UV Sensor	77
6.2	Gas Sensor	81
6.2.1	Ammonia Sensor	82

6.2.2	Hydrogen Sulfide Sensor	85
6.3	Discussions	86
6.4	Summary and Conclusions	87
7	Conclusions and Future Work	88
7.1	Conclusions	88
7.2	Future Work	90
	Appendix	92
A	Experimental Techniques	92
A.1	Laminar Flow Chemical Wet Bench	92
A.2	Ellipsometer	92
A.3	UV Exposure Unit	93
A.4	Raman Spectroscopy	94
A.5	X-ray Photoelectron Spectroscopy (XPS)	95
A.6	Atomic Force Microscope (AFM)	96
A.7	Scanning Electron Microscope (SEM)	98
A.8	Photolithography Tool	99
A.9	E-beam Metal Evaporator	100
A.10	Electrical Characterization	101
A.11	Graphene Annealing and Sensing Setup	103
A.12	Superconducting Quantum Interference Device (SQUID)	105
A.13	Physical Property Measurement System (PPMS)	106
A.14	Electron Spin Resonance (ESR)	107
B	Surface Treatment of SiO₂ Before Graphene Transfer	109

B.1	SiO ₂ Surface Treatment	110
B.2	Characterization of SiO ₂ Surface After Treatment	113
B.2.1	Contact Angle Measurement	113
B.2.2	AFM Characterization	114
B.2.3	XPS Characterization	115
C	Mobility Extraction by FTM Method	120
	References	122
	Publications	147

List of Figures

1.1	Left: energy spectrum of graphene calculated by tight-binding approach. Right: zoom-in of band close to one Dirac point [16].	2
2.1	A schematic of chemical bonds in (a) pristine graphene (dashed lines show delocalized double bonds), (b) single hydrogen atom chemisorbed by graphene (white circle represents an hydrogen atom and black circle represents an unpaired electron due to broken bond), (c) a pair of hydrogen atoms chemisorbed on graphene [20].	6
2.2	Graphene FET device characteristics of (a) Pristine graphene, (b) measured at different temperatures after hydrogen plasma exposure for different time periods, and (c) after annealing at 450°C [5].	8
2.3	Graphene oxide structure proposed by Nasrollahzadeh et al. [32].	9
2.4	A schematic of oxidation using AFM. In humid environment a water meniscus forms between graphene and AFM tip [47].	12
2.5	AFM image of electrically isolated region on the graphene surface (a) using hydrogenation (b) using oxidation [48].	13
2.6	Raman spectra of pristine graphene (red), after hydrogen plasma exposure (blue), and after annealing (green) [5].	14
2.7	XPS spectra for (a) pristine graphene (b) after functionalization (c) after annealing of functionalized graphene [13].	16

3.1	A schematic of transfer of CVD graphene onto SiO ₂ /Si substrate from copper foil (dimensions are not upto the scale).	23
3.2	An optical image of CVD graphene transferred onto SiO ₂	23
3.3	An optical image of exfoliated graphene on SiO ₂ . Here different colors indicate different numbers of graphene layers present.	24
3.4	Schematic representation of two types of functionalized CVD graphene samples prepared via thermal process (a) hydroxylation of graphene on copper foil and then transfer onto SiO ₂ /Si. (b) hydroxylation of CVD graphene after transfer onto SiO ₂ /Si.	25
3.5	Raman spectra for pristine graphene on Cu foil and graphene on Cu foil after treatment with H ₂ O ₂ for different time periods and temperatures, an increase in D peak intensity can be noticed with treatment.	26
3.6	I _D /I _G ratio for pristine graphene on Cu foil and graphene on Cu foil after treatment with H ₂ O ₂ for different time periods and temperatures, I _D /I _G ratio increases after increasing reaction time and temperature.	27
3.7	C 1s XPS spectra of (a) pristine CVD graphene on copper foil and (b) CVD graphene on copper foil after hydroxylation shows increase of C-OH bonds after reaction with H ₂ O ₂	28
3.8	An optical image of (a) as transferred CVD graphene on SiO ₂ (b) transferred graphene on SiO ₂ after heating in H ₂ O ₂ at 60°C for 30 minutes, circular shape damage to graphene can be seen after heating in H ₂ O ₂ . . .	29
3.9	Schematic representation of (a) hydroxylation of CVD graphene via treatment with H ₂ O ₂ in the presence of UV light, (b) hydroxylation of exfoliated graphene via treatment with H ₂ O ₂ in the presence of UV light, (c) graphene after hydroxylation.	30

3.10 (a) C 1s XPS spectra of pristine CVD graphene and CVD graphene after treatment with only H ₂ O ₂ for 30 minutes at RT shows no affect of H ₂ O ₂	
(b) deconvoluted C 1s XPS spectra of pristine CVD graphene, and (c,d) CVD graphene after 15 minutes and 30 minutes of H ₂ O ₂ treatment in the presence of UV light shows increase in oxygen containing functional groups.	32
3.11 Raman spectra of CVD graphene before hydroxylation and after hydroxylation for different time periods.	33
3.12 Raman spectra of exfoliated graphene before and after hydroxylation for different time periods.	34
3.13 Raman map of I _D /I _G ratio for 4 μm x 4 μm scan area of CVD graphene (a) before hydroxylation, and (b) after hydroxylation.	34
3.14 Raman spectra of exfoliated graphene after three hours of H ₂ O ₂ treatment in the presence of UV light. Inset shows the deconvoluted G peak. The black line is measured spectrum, the green and blue lines are the deconvoluted peaks.	35
3.15 Raman map of G peak position of (a) pristine CVD graphene (b) hydroxyl functionalized CVD graphene. Shows shift in G peak position after hydroxylation.	36
3.16 Mechanism of -OH radical addition to one ring of graphene. -OH radical generated via decomposition of H ₂ O ₂	37
3.17 Optical image of CVD graphene on SiO ₂ (a) after treatment of transferred graphene with H ₂ O ₂ in the presence of UV light and (b) with only H ₂ O ₂ at room temperature for 30 minutes, no damages to graphene in both the cases.	38
4.1 (a) Height image, obtained from AFM scan and (b) CPD image of HOPG to calculate workfunction of KPFM tip, obtained from KPFM scan.	40
4.2 (a) Height image, obtained from AFM scan and (b) CPD image of pristine graphene, obtained from KPFM scan.	40

4.3	(a) Height image, obtained from AFM scan and (b) CPD image of functionalized graphene, obtained from KPFM scan.	41
4.4	Analysis of KPFM scan for pristine graphene and functionalized graphene.	42
4.5	AFM line profile of the samples with Al ₂ O ₃ deposition on the surface (a) before hydroxylation (b) after hydroxylation.	42
4.6	SEM images of pristine exfoliated graphene after Al ₂ O ₃ deposition on (a) pristine graphene and (b) functionalized graphene	43
4.7	(a) Schematic of GFET device structure and (b) schematic representation of fabrication steps.	44
4.8	(a) SEM image of patterned AZ5214E resist when used as positive photoresist. (b) SEM image of patterned AZ5214E resist when used in image reversal mode, a retrograde sidewall slope can be seen.	48
4.9	An optical image of the fabricated graphene FET.	48
4.10	Transfer characteristics of CVD GFETs before and after hydroxylation when measured in air.	49
4.11	Transfer characteristics of CVD GFETs before and after hydroxylation when measured in vacuum.	50
4.12	C 1s XPS spectra of hydroxyl functionalized CVD graphene before and after vacuum annealing at 150°C for 30 minutes.	52
4.13	Hysteresis of gate response for pristine and hydroxyl functionalized graphene FETs.	52
4.14	Transfer characteristics of functionalized graphene FETs in different conditions	53
4.15	Schematic of TLM devices used for contact resistance measurements. . . .	54
4.16	Process flow for TLM device fabrication.	55
4.17	An optical image of as fabricated TLM devices.	56

4.18	Total resistance values for different channel length devices before and after H ₂ O ₂ treatment.	56
4.19	Schematic of device with different metal-graphene overlap length.	57
4.20	An optical photograph of device with different metal-graphene overlap lengths.	58
4.21	Total resistance vs metal-graphene overlap length.	58
5.1	N 1s XPS spectra of (a) Only -OH functionalized graphene, no signature of nitrogen, and (b) Graphene after two step process of hydroxylation and ammonia annealing, confirm presence of nitrogen, the measured spectrum was deconvoluted into three peaks.	61
5.2	Raman spectra of pristine CVD graphene (black), and after hydroxylation (red) and after nitrogen doping via ammonia annealing after -OH functionalization (blue).	62
5.3	Magnetization as a function of magnetic field at 2 K for pristine graphene shows diamagnetic behavior, (a) as measured (b) after background subtraction.	63
5.4	M-H curve for hydroxyl functionalized graphene.	63
5.5	(a) Magnetic moment as a function of magnetic field for different temperatures from 2 K to 300 K for N doped graphene. (b) Magnified image for lower magnetic field values at 2 K.	64
5.6	Magnetization as a function of temperature at a magnetic field of 1.5 kOe for nitrogen doped graphene.	65
5.7	(a) Topography AFM image (b) 2D MFM image (c) 3D MFM image (c) line section of 2D MFM scan for pristine graphene.	67
5.8	(a) Topography AFM image (b) 2D MFM image (c) 3D MFM image (c) line section of 2D MFM scan for -OH functionalized graphene.	67

5.9	(a) Topography AFM image (b) 2D MFM image (c) 3D MFM image (c) line section of 2D MFM scan for nitrogen doped graphene.	68
5.10	ESR spectra for (a) nitrogen doped graphene, shows good resonance curve, (b) for only -OH functionalized graphene (c) for pristine graphene, no resonance can be seen in (b) and (c).	69
5.11	Schematic of devices fabricated for angular AMR measurements (dimensions are not upto the scale).	70
5.12	Schematic of devices inside the PPMS tool shows in-plane magnetic field at an angle of 0° with respect to the graphene.	70
5.13	(a) AMR as a function of angle of applied magnetic field (70 kOe) at different temperatures from 2 K to 200 K, beyond 150K devices didn't show any AMR. (b) Maximum AMR value as a function of temperature at constant magnetic field of 70 kOe and angle of 35°	71
5.14	(a) AMR measured at 2 K for in-plane magnetic field in the range from 3 kOe to 70 kOe. (b) Maxima AMR value at 35° as function of in-plane magnetic field at 2 K. (c) Resistance as a function of magnetic field at 2 K for 0° , 120° and 210°	72
6.1	UV-Vis spectra of pristine CVD graphene and -OH functionalized CVD graphene on quartz.	76
6.2	(a) Flow chart of sensor device fabrication (b) A schematic of the sensor device (top view).	78
6.3	Photograph of a sensor device at different zoom levels.	79
6.5	Response measured in quantum efficiency tool.	79
6.4	(a) Current measured in dark after 15 sec exposure of light. (b) rate of recovery of current in dark with time after 15 sec exposure of light. (c) current measured in presence of light until 5 minute of exposure. (d) rate of decrease in current in continuous exposure of light.	80

6.6	Response to UV light of hydroxyl functionalized graphene device.	81
6.7	Pristine graphene device is behaving randomly and shows no response to UV light.	81
6.8	(a) Response vs time for NH ₃ at room temperature for 20 sec pulses of NH ₃ gas. (b) Response vs time for NH ₃ at 50°C for 20 sec pulses of NH ₃ gas. . .	83
6.9	(a) Comparison of response at room temperature and 50°C. (b) Saturation for NH ₃ gas at room temperature and 50°C.	84
6.10	Response vs time for NH ₃ at room temperature for back-to-back gas pulses of 10 sec, to check the repeatability of sensor.	85
6.11	Response vs time for H ₂ S gas at room temperature for a 40 sec pulse. . .	86
6.12	Schematic of electron donation from NH ₃ to graphene.	87
7.1	Summary of work.	90
A.1	Photograph of ellipsometer [148].	93
A.2	Photograph of UV exposure unit.	94
A.3	Photograph of Raman spectroscopy instrument [149].	95
A.4	Photograph of X-ray Photoelectron Spectroscopy instrument.	96
A.5	Photograph of AFM measurement instrument.	97
A.6	Photograph of Raith150 ^{two} SEM equipment [148].	98
A.7	A photograph of EVG 620 photolithography tool [148].	100
A.8	Photograph of (a) I-V measurement setup (b) probe manipulators (c) chuck.	102
A.9	Photograph of Keithley 2450 connected with a laptop for current measurement.	103
A.10	Drawing of in-house built graphene annealing and sensing setup (a) side view. (b) top view.	104

A.11 Photograph of (a) Graphene annealing ad sensing setup (b) BNC connectors for electrical measurements.	105
A.12 Photograph of PPMS instrument.	107
A.13 Photograph of horizontal rotator and sample mounting chips [150].	107
A.14 Photograph of electron spin resonance spectrometer [149].	108
B.1 Process flow showing different types of surface treatments.	110
B.2 (a) Comparison of the transfer characteristics of GFETs fabricated on SiO ₂ without any treatment and with FGA. (b) Comparison of shift in Dirac point position with multiple measurement runs back-to-back on the same device.	111
B.3 (a) Transfer characteristics of GFETs fabricated on three types of SiO ₂ - FGA, O ₂ plasma treated and Ar plasma treated (b) shift in CNP with multiple measurement runs back-to-back.	112
B.4 Raman spectra of graphene transferred onto three types of SiO ₂	113
B.5 Contact angles for different samples prepared with different types of SiO ₂ surface treatment.	114
B.6 (a) Ar 2p XPS spectra of the sample treated with Ar plasma (b) Comparison of C 1s XPS spectrum of the surface of SiO ₂ for the FGA, O ₂ plasma and Ar plasma treated, (c) Ar 2p spectra for FGA SiO ₂ , and (d) Ar 2p spectra for O ₂ plasma treated SiO ₂	115
B.7 Deconvoluted O 1s XPS spectrum of the surface of SiO ₂ for (a) FGA, (b) Ar plasma and (c) O ₂ plasma treated samples.	116
B.8 Comparison of area percentage values of deconvoluted peaks of O 1s XPS spectrum of the surface of SiO ₂ for FGA, Ar plasma and O ₂ plasma treated.	117
C.1 R_{total} vs V_G curve fitted for pristine graphene FET, when I-V is measured in air.	121

List of Tables

3.1	C 1s XPS peak positions and bond configuration of graphene on Cu foil before and after functionalization.	28
3.2	Relative peak area for each deconvoluted peak of C 1s spectra of CVD graphene before and after different H ₂ O ₂ treatments at room temperature.	31
5.1	I _D /I _G values for pristine, only -OH functionalized, and nitrogen doped graphene.	62
B.1	RMS roughness and max height values for three samples calculated through 5 μm AFM scan	114
B.2	Comparison of different surface treatment techniques reported in literature. FGA sample without any surface treatment shows better results	118

List of Symbols

C_{ox}	Oxide gate capacitance ($F\ m^{-2}$)
e	Charge of an electron (C)
I	Current (A)
L	Transistor channel length (μm)
W	Transistor channel width (μm)
n	Charge carrier density (cm^{-2})
n_{imp}	Charged impurity density (cm^{-2})
R	Resistance (ohms)
V	Voltage (V)
V_G	Gate voltage (V)
V_{Dirac}	Gate voltage at Dirac point (V)
V_{Fermi}	Fermi velocity ($m\ s^{-1}$)
μ	Mobility ($cm^2/V.s$)
μ_p	Hole mobility ($cm^2/V.s$)
μ_n	Electron mobility ($cm^2/V.s$)
μ_B	Bohr magneton (emu)
σ	Conductivity ($S\ cm^{-1}$)
σ_{min}	Minimum conductivity ($S\ cm^{-1}$)
σ_{res}	Residual conductivity ($S\ cm^{-1}$)

List of Abbreviations

AFM	Atomic Force Microscopy
ALD	Atomic Layer Deposition
AMR	Anisotropic Magnetoresistance
ARPES	Angle Resolved Photoelectron Spectroscopy
BDE	Bond Dissociation Enthalpy
CDA	Compressed Dry Air
CNP	Charge Neutrality Point
CNT	Carbon Nanotube
CPD	Contact Potential Difference
C-V	Capacitance - Voltage
CVD	Chemical Vapour Deposition
DI	De-ionized Water
EBID	Electron Beam-Induced Deposition
ESR	Electron Spin Resonance
FGA	Forming Gas Annealing
FTM	Fitting Method
FWHM	Full Width Half Maximum
GFET	Graphene Field Effect Transistor
GO	Graphene Oxide
HMDS	Hexamethyldisilazane
HOPG	Highly Oriented Pyrolytic Graphite
IPA	Isopropyl Alcohol
I-V	Current-Voltage

KPFM	Kelvin Probe Force Microscopy
MFC	Mass Flow Controller
MFM	Magnetic Force Microscopy
MR	Magneto Resistance
NGr	Nitrogen doped Graphene
PMMA	Poly(methyl methacrylate)
ppb	parts per billion
ppm	parts per million
PPMS	Physical Property Measurement System
RCA	Radio Corporation of America
RGO	Reduced Graphene Oxide
RMSE	Root Mean Square Error
RMS	Root Mean Square
RT	Room Temperature
sccm	standard cubic centimeters per minute
SEM	Scanning Electron Microscope
SSE	The Sum of Square due to Error
SQUID	Superconducting Quantum Interference Device
TLM	Transfer Length Measurement
TMD	Transition Metal Dichalogenides
UV	Ultra-Violet
XPS	X-ray Photoelectron Spectroscopy

Chapter 1

Introduction

In solid state physics, carbon is one of the most intensively studied elements. Graphene is a two dimensional allotrope of carbon and monolayer of graphene contains single atomic layer of carbon atoms. Physical existence of monolayer graphene was first discovered by K. S. Novoselov and A. K. Geim [1] in 2004 and they were awarded the Nobel prize in physics for 2010 for this discovery. Graphene has very high charge carrier mobility and due to its planar geometry, it is a very promising material for nanoelectronics applications [1, 2]. Graphene possesses zero band gap [2] and it is not chemically reactive [3] and diamagnetic in nature [4], restricting its use in the field of semiconductor devices, sensors and spintronics. Through functionalization it is possible to modify the electronic [5, 6], magnetic [7, 8, 9] and chemical properties of graphene [10]. Methods to functionalize graphene can be divided into two categories, physical and chemical. The physical methods include plasma and heat treatments. Various plasma processes reported in the literature include hydrogen plasma for hydrogen characterization [5], fluorine plasma for fluorination [11], ammonia plasma for nitrogen functionalization [12] and oxygen plasma for oxidation [13, 14]. Thermal annealing in NH_3 for nitrogen functionalization and n-type doping of graphene were also reported [15].

Graphene is made of sp^2 hybridized carbon atoms where strong σ bonds form between s, p_x and p_y orbitals. And p_z orbitals of carbon atom overlap with the neighboring carbon atom and produce two bands, π and π^* . Band π is completely filled with electrons, called as valence band and π^* is empty band, called as conduction band. At Brillouin zone

corners these two bands touch and therefore make graphene a zero band-gap nanostructure as shown in figure 1.1 [16].

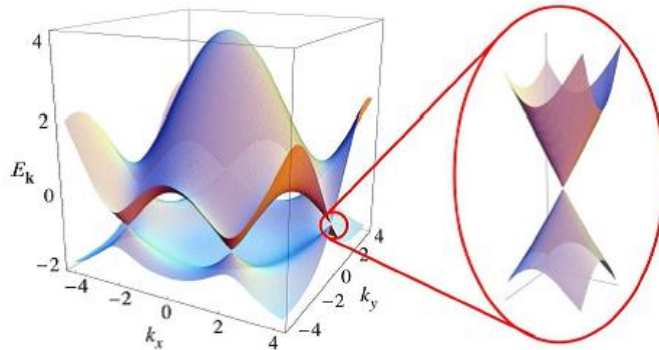


Figure 1.1: Left: energy spectrum of graphene calculated by tight-binding approach. Right: zoom-in of band close to one Dirac point [16].

1.1 Motivation

Abhishek Misra had shown that workfunction of graphene oxide (GO) varies after GO is reduced by annealing at different temperatures [17]. This workfunction tuning of graphene can fulfill the contact electrode requirements in several device technologies, like CMOS, organic photovoltaics (OPVs), and organic light-emitting diodes (OLEDs) [18]. Hydroxyl functionalized graphene is biocompatible and reduced GO (RGO) can be used for sensing different types of chemicals and gases. But it is difficult to reduce GO completely and deposit monolayer of GO on any type of substrate. For thin film applications it is difficult get a continuous large area layer of GO and RGO. Reduction of graphene through thermal annealing and chemical process results in defects like vacancy and contamination in RGO. Synthesis process of GO through Hummer's method [19] itself use chemicals which leave their traces in GO. GO has very low charge carrier mobility of around 1 to $10 \text{ cm}^2\text{V}^{-1}\text{s}^{-1}$. Whereas CVD graphene and exfoliated graphene have very good carrier mobility and their synthesis process does not leave any contamination in them. It is also very easy to synthesize single layer CVD graphene and use it in semiconductor fabrication as it is compatible with many of the standard fabrication techniques.

The motivation of this thesis to develop a process to functionalize CVD and exfoliated graphene to obtain graphene somewhat similar to RGO in terms of properties, but with high charge carrier mobility, large area single layer film, and without any contamination, and further use this functionalized graphene for different applications in the field of electronics, spintronics and sensing.

1.2 Thesis Organization

This thesis contains total 8 chapters providing steps involved in graphene functionalization, characterization and applications. In chapter 2, literature survey on different types of graphene functionalization, methods and techniques involved in graphene functionalization, characterization of functionalized graphene and applications of functionalized graphene are presented in brief. Chapter 3 discuss in details the chemical methods used for functionalization of graphene with hydroxyl groups. Two chemical methods have been discussed along with mechanism of functionalization, their advantages and drawbacks followed by characterization of functionalized graphene with Raman spectroscopy and XPS. The goal was to functionalize graphene without any physical damage and to minimise degradation of the carrier mobility. Chapter 4 starts with applications of functionalized graphene, and workfunction engineering. Atomic Layer Deposition (ALD) of Al_2O_3 and graphene field effect transistor fabrication are also discussed in this chapter. Graphene field effect transistors were fabricated using photo-lithography using both types of graphene, pristine and functionalized graphene. The steps involved in transistor fabrication, results showing change in current-voltage (I-V) characterization, mobility values of both types of graphene and vacuum stability of -OH groups are also discussed in chapter 4. In chapter 5, introduction of ferromagnetism in functionalized graphene via nitrogen doping, magnetization measurement using superconducting quantum interference device (SQUID), ESR, MFM and anisotropic magnetoresistance measurement using physical property measurement system (PPMS) have been discussed. Chapter 6 shows two more applications of functionalized graphene, one is UV sensor and another is gas sensor based on -OH functionalized graphene. Chapter 7 summarizes the work done along with fu-

ture outlook. Appendix-A gives an overview of different experimental techniques used in this work, appendix-B shows the effect of surface treatment of SiO₂ on graphene device performance, and appendix-C shows method for calculation of charge carrier mobility for graphene field effect transistors.

Chapter 2

Literature Review

2.1 Introduction

After discovery of graphene, the researchers start looking for techniques to tune the graphene from its ideal properties for different applications. The functionalization of graphene is the most popular method for alteration of graphene's properties [20]. Functionalization is a process of adding new functions, features, capabilities, or properties to a material by changing the surface chemistry of that material. In this chapter, a literature survey on functionalization of graphene is presented and we will discuss different mechanisms for graphene functionalization, types of graphene functionalization, different techniques which have been used so far for graphene functionalization and characterization, and applications of functionalized graphene. Functionalization of all types of graphene which includes graphene oxide (GO), reduced graphene oxide (RGO), mechanically exfoliated graphene and CVD graphene has been discussed.

2.2 Mechanism of Graphene Functionalization

Two types of mechanisms are involved in functionalization of graphene, one is non-covalent which is due to the weak interactions of graphene's carbon atoms with other atoms or molecules via Van der Waals forces and different types of π interactions. Another is covalent type functionalization, when graphene's carbon atoms make strong covalent bond with atoms and molecules of functional groups to be attached. Covalent bonding is

of more interest than non-covalent because covalent bonds are much stronger and stabler than non-covalent and most of the organic (e.g. dienophiles) and non organic molecules (e.g. hydrogen, fluorine, oxygen) make covalent bond with graphene. We will focus mainly on covalent bonding in this literature review.

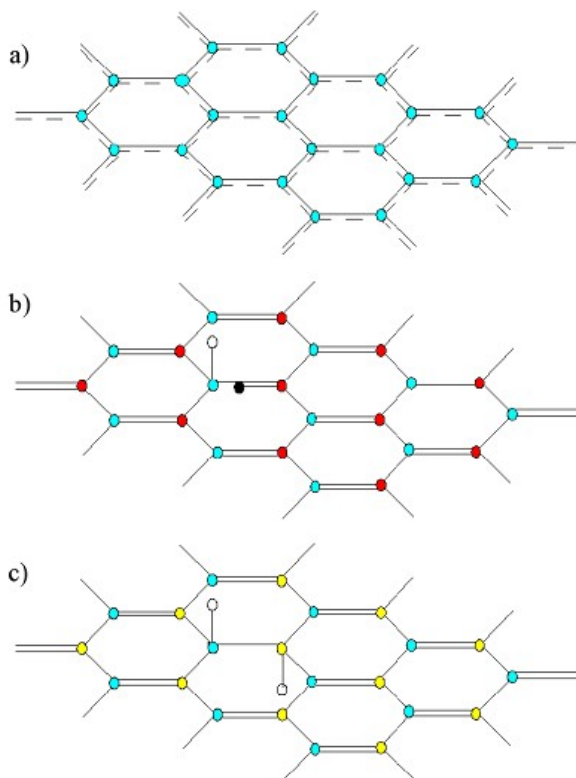


Figure 2.1: A schematic of chemical bonds in (a) pristine graphene (dashed lines show delocalized double bonds), (b) single hydrogen atom chemisorbed by graphene (white circle represents a hydrogen atom and black circle represents an unpaired electron due to broken bond), (c) a pair of hydrogen atoms chemisorbed on graphene [20].

Covalent attachment of free radicals, hydrogen, halogens or dienophiles form covalent bonds with sp^2 bonded carbon atoms of graphene [21]. This chemisorption of a molecule or atom results in breakage of a π bond and transformation of hybridization from sp^2 to sp^3 . Also at the same time for each broken π bond, an electron remains unpaired at the neighboring carbon which changes the properties of graphene, figure 2.1 [20].

Covalent bonding of a functional group is a surface transfer process where electron exchange occurs between graphene and adsorbed functional group on the surface of graphene, which results in doping of graphene. Depending upon the type of functional

group attached, the doping is either p-type or n-type. If an electron acceptor group is attached to graphene, it will dope graphene with holes, i.e. graphene will become p-type. If an electron donor group is adsorbed then graphene would be n-type doped [6].

2.3 Types of Graphene Functionalization

In this section different types of functionalization, based on functional group to be attached, are briefly reviewed.

2.3.1 Hydrogenation

Carbon based materials are attractive for hydrogen storage [22] and researchers have already shown hydrogen storage in carbon nanotubes (CNTs) [23]. After hydrogen functionalization, the graphene cannot only be used for hydrogen storage but it also open a bandgap [5] and introduce magnetism in graphene [9, 24, 25]. Schematic of hydrogen atom adsorption on graphene surface is shown in figure 2.1. Hydrogen plasma can be used to functionalize graphene with hydrogen in a controlled and reversible way [5].

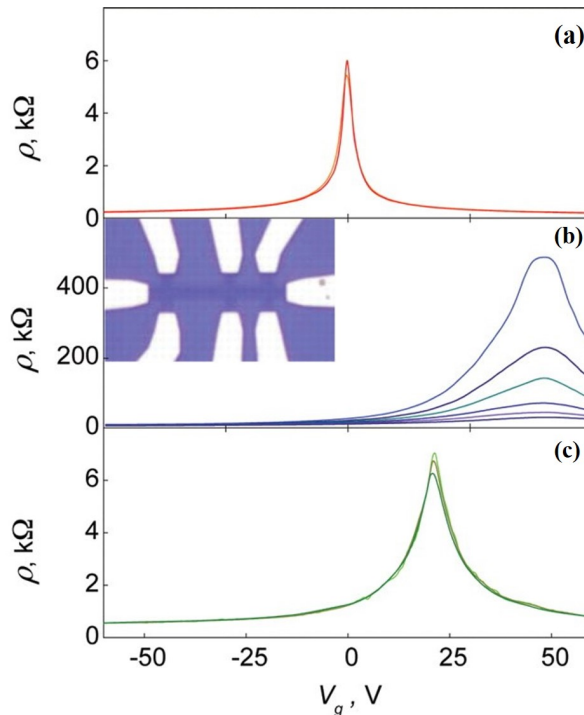


Figure 2.2: Graphene FET device characteristics of (a) Pristine graphene, (b) measured at different temperatures after hydrogen plasma exposure for different time periods, and (c) after annealing at 450°C [5].

Hydrogen is chemisorbed on the graphene surface and results in breakage of bond symmetry, and hybridization change to sp^3 [5]. Changes in the behavior of graphene devices with different plasma exposure time is shown in figure 2.2 (b). Devices start showing insulating behavior as the resistivity increase by two orders of magnitude when temperature decreases from 300 K to 4 K. Also there was a shift of charge neutral point (Dirac point, V_{Dirac}) to gate voltage (V_G) ≈ 50 V. This positive shift of Dirac point shows that graphene is now doped with holes which means hydrogenation result in p-type doping of graphene. After 24 hours of annealing at 450°C in Ar atmosphere D. C. Elias et al. were able to restore the metallic property of graphene, figure 2.2 (c) [5].

2.3.2 Oxidation

Oxidation of graphene can be achieved through a wet chemical process wherein graphite is oxidized to obtain GO [19]. The GO can be subsequently reduced to obtain RGO [18]. GO is a wide bandgap, insulating material [26] whereas RGO shows

semiconducting behavior [27]. RGO is hydrophilic in nature [28] and shows intrinsic photoluminescence [29]. Field Effect Transistors (FET) made of RGO shows on-off current ratio lower than 10 and charge carrier mobility in the range of 0.001 to $10 \text{ cm}^2 \text{ V}^{-1} \text{ s}^{-1}$ [30], because it is difficult to reduce GO completely. Oxidation also change hybridization and open a band gap in graphene. Attachment of one oxygen atom consumes two unpaired p_z electrons whereas hydrogen and fluorine each consumes only one electron each [31]. GO and RGO not only contains oxygen atoms bonded to it but also other oxygen containing groups like hydroxyl (-OH) and carboxyl (-COOH).

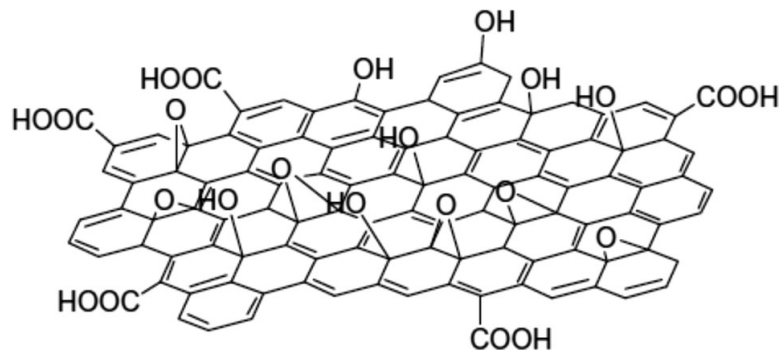


Figure 2.3: Graphene oxide structure proposed by Nasrollahzadeh et al. [32].

GO and RGO are chemically active materials and can be used in the field of biosensors, gas sensors and chemical sensors. In many applications of GO or RGO in sensors, the changes in conductivity is monitored [33, 34, 35]. Conductivity is proportional to the mobility of the charge carriers in the material. Hence functionalized graphene with higher mobility can be expected to result in sensors with higher sensitivity. Graphene can be oxidized using oxygen plasma in a controlled way but it also damages the graphene as graphene is a few atom thick layer which could be easily sputtered by plasma [13]. Resultant structural defects affect the mobility [5]. Chemical reduction of GO insert impurities and contamination in RGO [36] whereas thermal reduction leaves behind vacancies and topological defects by the release of CO and CO₂ [37]. Another problem with the GO and RGO route to synthesis of oxygen functionalization is that large area continuous films may not be achieved [38]. So it is better to start with large area graphene and functionalize it with oxygen in a controlled way.

2.3.3 Fluorination

Fluorographene is a fluorine functionalized form of graphene. Graphene can be functionalized with fluorine by treating it with fluorine plasma [13] or by exposure to fluorine containing gas XeF_2 [39]. Fluorination also changes the optical and electrical properties of graphene. Fluorine atom adsorption on graphene surface rehybridizes carbon atoms to sp^3 . Fluorographene starts behaving like insulator due to forming of large band gap in graphene [11].

2.3.4 Hydroxylation

Hydroxylation is attachment of hydroxyl group (-OH) on the surface of graphene. Hydroxyl functionalized graphene (G-OH) synthesised by chemical functionalization of GO or RGO is biocompatible [40, 41], and can be used as a catalyst [42], energy storage material [43], gas sensor and nanoscale ionic material [44]. One-side coverage of graphene with -OH groups is predicted to introduce magnetization in graphene [45]. For deposition of high-k dielectric through ALD, the substrate surface should be -OH termination. Thus deposition of high-k dielectric on graphene is not possible unless graphene is functionalized with hydroxyl. Experimental evidence of functionalization of graphene with hydroxyl groups by any physical or chemical routes other than those describe in section 2.3.2 for GO and RGO are available to the best of our knowledge.

2.3.5 Other Organic Molecules

Diazonium salt, e.g. 4-nitrobenzene diazonium tetrafluoroborate, produce a highly reactive free radical upon heating and this radical can attach on sp^2 hybridized carbon atoms of graphene by forming a covalent bond [46]. Dienophiles, which are electron withdrawing groups, also react with graphene and results in change of hybridization, open a bandgap and dope graphene with holes, e.g. Azomethine Ylides which are nitrogen-based 1,3-dipoles [31].

2.4 Techniques for Graphene Functionalization

Graphene can be functionalized using different types of chemical and physical methods.

2.4.1 Wet Chemical Reactions

Oxygen functionalized graphene or RGO can be synthesised chemically after reduction of GO, where GO is produced by chemical oxidation and exfoliation of graphite [19]. As explained in section 2.3.2, there are many drawbacks to this route of functionalization. Apart from oxidation, researchers have achieved functionalization of graphene with fluorine [11, 39], free radicals [46] and dienophiles [31] using chemical reaction based methods. The main advantage of this technique is that we can achieve functionalization of graphene without much damages to graphene structure. Thus there is a possibility of achieving high charge carrier mobility after functionalization of graphene by chemical route if there is no physical damage to graphene after chemical reactions.

2.4.2 Plasma Exposure

Elias et al. used DC plasma to functionalize graphene with hydrogen [5]. Graphene was treated with cold hydrogen plasma at a pressure of 0.1 mbar where a mixture of argon/hydrogen (10% H₂) was used to generate plasma. But disadvantage of using DC or RF plasma is that plasma energy is so high that carbon atoms may be removed from the graphene surface and affect the charge carrier mobility of functionalized graphene. Even after annealing, Elias et al. were not able to recover graphene completely which confirms the permanent defects in graphene structure.

As a solution to this, M. Barket et al. [13] used electron beam generated plasma for oxidation and fluorination of graphene. Electron beam generated plasma offer high density of plasma and have low electron temperature. This result in a large flux of ions with a low energy delivered to graphene surface thus result in oxidation/fluorination of graphene without etching or with low damage to graphene structure.

2.4.3 Nanolithography Using AFM

Giesbers et al. [47] and Ik-Su Byun et al. [48] showed that nanoscale lithography using AFM on graphene surface results in selective hydrogenation and oxidation of graphene.

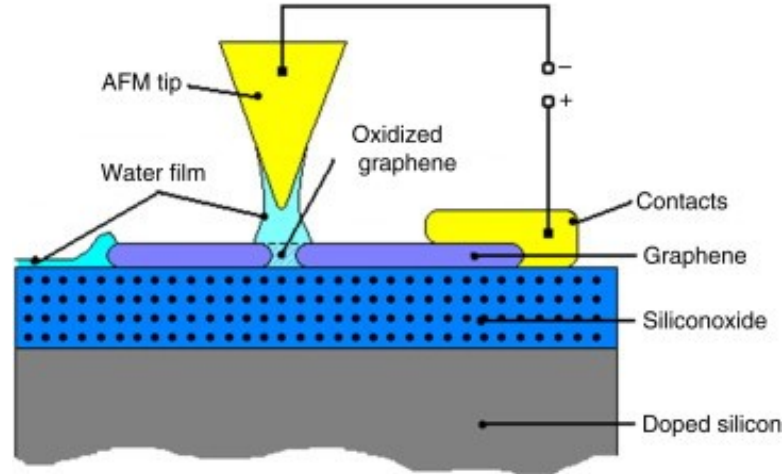


Figure 2.4: A schematic of oxidation using AFM. In humid environment a water meniscus forms between graphene and AFM tip [47].

A water layer from ambient moisture form a meniscus between AFM tip and graphene surface, and after applying a DC bias on graphene using AFM tip results in electrical dissociation of water, figure 2.4 [47]. When negative voltage was applied to graphene, hydrogen ions (H^+) were adsorbed on the surface and when positive voltage was applied to graphene, oxygen (OH^- & O^-) ions were adsorbed on graphene surface which oxidized it.

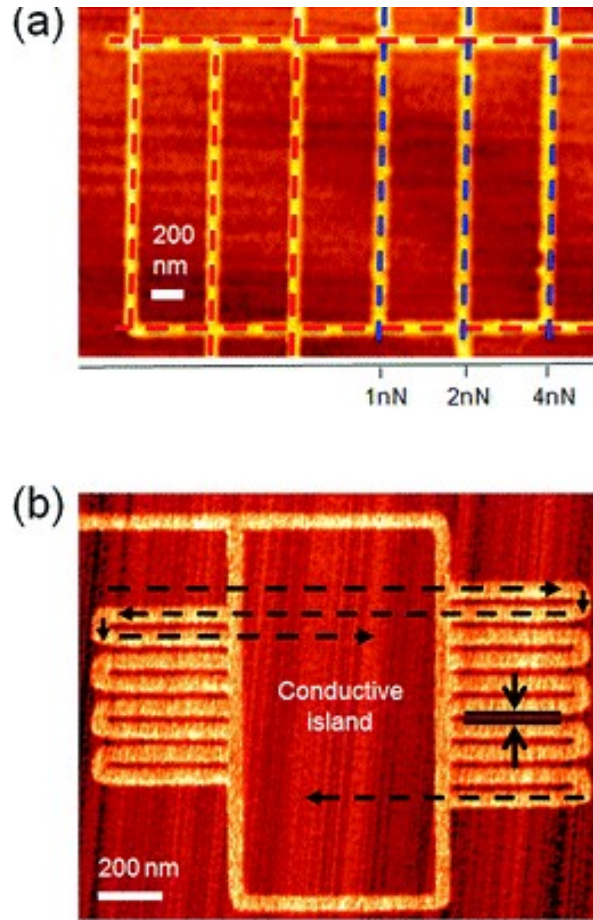


Figure 2.5: AFM image of electrically isolated region on the graphene surface (a) using hydrogenation (b) using oxidation [48].

This technique of functionalization is highly selective and purely non-destructive because it doesn't cause any damage to graphene structure. It makes possible to functionalize graphene selectively and to write functionalized lines (insulating lines) in nano scale on graphene surface which can be used for isolation between devices, figure 2.5 [48]. However this is a low throughput method which limits its practical applicability.

2.5 Characterization of Functionalized Graphene

In this section main characterization techniques that have been used to characterize structural, chemical, and electronic properties of graphene reported in the literature are reviewed.

2.5.1 Raman Spectroscopy

Raman spectroscopy can be used to detect the functionalization induced structural changes in graphene. After chemical functionalization the graphene basal plane are distinct from pristine graphene due to localized, physical defects in sp^2 -conjugated carbon atoms. In-plane vibrations of the conjugated π bonds have characteristic Raman spectra [49]. Raman spectroscopy of graphene have three main features, D peak at 1350 cm^{-1} , G peak at 1580 cm^{-1} and 2D peak at 2680 cm^{-1} and after chemical functionalization changes in the G, 2D and D peaks can be seen. Figure 2.6 shows the Raman spectroscopy results of after hydrogenation of graphene, after the process explained in section 2.3.1 [5].

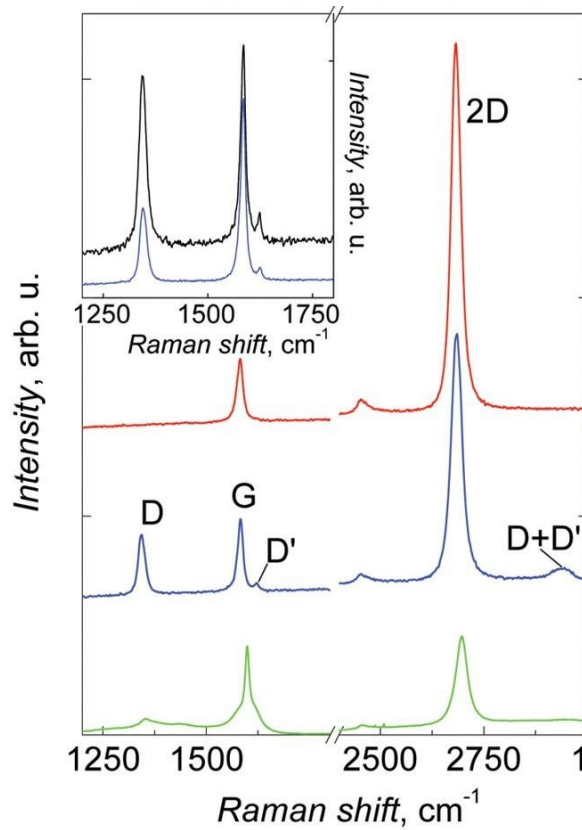


Figure 2.6: Raman spectra of pristine graphene (red), after hydrogen plasma exposure (blue), and after annealing (green) [5].

Red curve is for pristine graphene, blue is for hydrogenated graphene and green is after annealing. Raman spectra of pristine graphene don't show any D peak which corresponds to defects in graphene. After functionalization, sharp D' and D peaks appear and

height of 2D peak relative to G peak decreases. 2D peak doesn't need defects for activation whereas both D and D' peaks require a defect for their activation. The D peak intensity represents the amount of disorder in graphene [50]. It appears after plasma treatment because functionalization breaks the translation symmetry of sp^2 carbon atoms bonds after formation of carbon-hydrogen sp^3 bonds [49]. D' peak appears due to intravalley double resonance process in the presence of defects [49]. Degree of functionalization can be calculate by the ratio of carbon atom bonded with sp^2 to the carbon atoms bonded with sp^3 hybridization. This ratio can be estimated from the ratio of intensity of D peak (I_G) and G peak (I_D), (I_D/I_G). I_D/I_G increases after functionalization which means conversion of sp^2 to sp^3 hybridization. After annealing, (green curve) Raman spectra recovered to almost similar to pristine graphene spectra. Peaks corresponding to defects (D, D', D + D') are highly suppressed. But 2D peak was not recovered back to its original, and remain at low intensity compare to pristine graphene. Also both 2D and G peak shift to higher wave number even after annealing, which means graphene is p-doped [51].

2.5.2 X-ray Photoelectron Spectroscopy (XPS)

By examining XPS spectra, the chemical changes introduced by functionalization can be observed. C 1s XPS spectra of graphene can be used to differentiate atoms and molecules attached to graphene after functionalization. Baraket et al. used electron beam generated plasma for functionalization of graphene, and examined C 1s XPS spectra before and after plasma treatment [13]. The changes in chemical composition of graphene reported in [13] is shown in figure 2.7. The C 1s XPS spectra of as grown pristine graphene shows a peak at 284.4 eV which corresponds to the sp^2 C-C bond and the full width half maximum (FWHM) of peak is very low and hence it cannot be deconvoluted to multiple peaks. After plasma treatment the peak become broad and after deconvolution to multiple peaks it shows peaks for C-O at 285.5 eV, C=O at 287.3 eV, and O-C=O at 286.6 eV along with sp^2 C-C at 284.4 eV. This clearly shows the different atomic/molecular species attached to carbon atoms of graphene after functionalization. Atomic percentage of functional group can also be calculated from XPS. For this particular example atomic % of oxygen increased from 6 % to 30 % after functionalization. Similarly nitrogen spectra

for nitrogen functionalization and fluorine spectra for fluorine functionalization can be analysed.

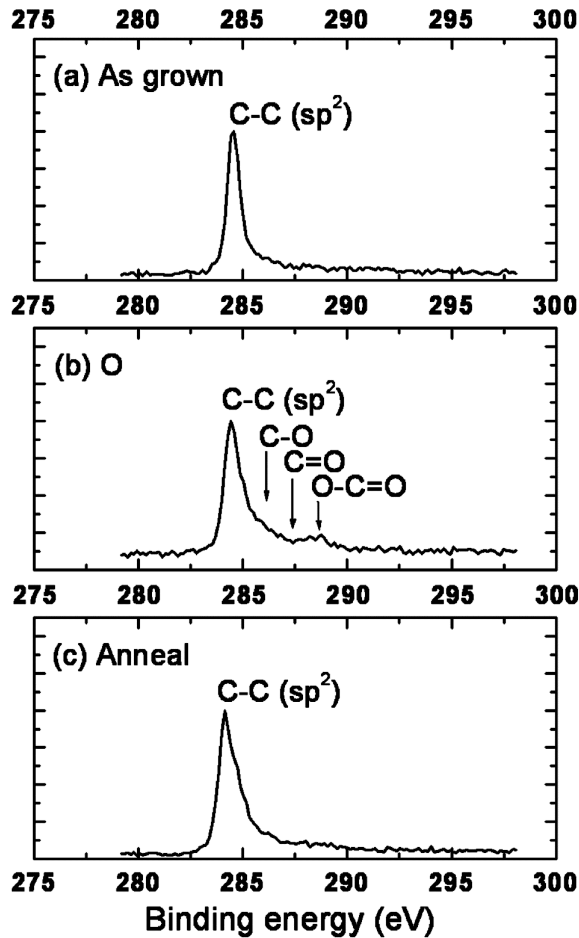


Figure 2.7: XPS spectra for (a) pristine graphene (b) after functionalization (c) after annealing of functionalized graphene [13].

2.6 Applications of Functionalized Graphene

2.6.1 Electronic and Optoelectronic Applications

Covalent functionalization of graphene can open a bandgap and dope graphene with electrons or holes, which makes functionalized graphene a very interesting material for use in semiconductor devices. Pristine graphene has very high charge carrier mobility hence it has a great potential to be used as a channel material in transistors. However in the absence of energy bandgap, the transistors cannot be turned off. Functionalization

may open a bandgap. But simultaneously it may reduce the charge carrier mobility due to creation of structural defects, during functionalization process [5]. If functionalization can be done by a process that do not introduce any defects or damage or with minimal damage, then there is a possibility of no or a feeble affect on the charge carrier mobility of graphene. This may result in a graphene with sufficient energy bandgap and high carrier mobility.

After functionalization it is also possible to dope graphene with holes or electrons, depending upon the type of functional groups. For example, oxygen and NO_2 functionalization make graphene p-type doped [52] and nitrogen functionalization make graphene n-type doped [51, 53]. Functionalized graphene has also been used as electrodes in battery and supercapacitors [54, 55, 56, 57, 58].

Ideally bilayer graphene has zero bandgap. In the presence of on-site energy difference between top and bottom layer in a Bernal-stacked bilayer graphene an energygap can be developed [16]. This can be achieved either by applying vertical electric field using an extra gate electrode or by inducing an inter layer electric field by charge redistribution [59] or by placing charge on top and bottom layers [60]. Wenjing Zhang et al. decorated bilayer graphene with triazine, $\text{C}_3\text{H}_3\text{N}_3$, which breaks the inversion symmetry between top and bottom layers of bilayer graphene and results in increase of on state current (I_{ON}) to off state current (I_{OFF}) ratio from around 10 to 30-65 and a permanent bandgap of ≈ 111 meV [61].

Apart from these, researchers have also shown application of functionalized graphene in optoelectronics, like in solar cells [62], as UV sensors [63, 64, 65, 66] and photodetectors [67, 68]. Guanyu Zhao et al. have shown application of RGO for efficient dye-sensitized solar cells [62]. Rahman et al. used cobalt sulfide grafted graphene nanosheet as counter electrode for dye-sensitized solar cells [69]. Iqbal et al. used RGO/tin oxide composite as transparent electrode for perovskite solar cells [70]. Vaqueiro-Contreras et al. have shown field effect surface passivation of silicon for solar cells by using GO films [71].

2.6.2 Applications in Magnetism

Magnetism is an important property being explored in graphene since its discovery [72]. Recently the research community has shown great interest in graphene spintronics via twisted bilayer graphene at moiré angle (magic angle) [73] and graphene - transition metal dichalogenide (TMD) heterostructures [74, 75, 76, 77]. Graphite is a diamagnetic material [78], and pristine graphene has inherited the property of diamagnetism from graphite [4]. Graphene consist of sp^2 hybridized carbon atoms with an electron cloud of delocalised π electrons and these electrons freely move in the graphene crystal plane. In the absence of unpaired electrons, pristine graphene does not show any type of magnetization at any temperature [4].

Magnetization can be introduced in graphene if the π - π bond symmetry in delocalised π network is broken, as this would lead to unpaired free electrons with net magnetic moment which will contribute to the net magnetization in graphene. Many experimental and theoretical studies have been reported on magnetization in graphene and GO via creating various types of defects [79, 80, 81, 82], hydrogen adsorption [9, 24, 25], thermal annealing [83, 84], nitrogen doping [7, 85, 86, 87, 88, 89, 90], and sulfur doping [8]. When defects are created in biparticle graphene lattice by adding or removing an atom from the lattice, it gives a net magnetic spin of $|N_A - N_B|/2$ by Lieb's theorem [91, 92], where $N_A - N_B$ is the difference between number of atoms in the sublattice imbalanced by defects. Xie et al. [9] showed that after partial hydrogenation, unpaired π electrons results in magnetization in epitaxial graphene. However magnetization was not possible when the epitaxial graphene was fully hydrogenated because of the disappearance of both paired and unpaired π electrons after complete hydrogenation. Liu et al. [7] prepared nitrogen doped RGO after annealing of RGO in NH_3 gas and showed increase in magnetization after nitrogen doping. With the increase of pyrrolic nitrogen magnetization increases whereas increase of pyridinic and graphitic nitrogen decreases magnetization. Nitrogen doping of GO and RGO introduce ferromagnetism but the exact mechanism behind this is still not clear.

For modern thin film spintronics devices anisotropic magneto resistance (AMR) is

one of the important properties. AMR effect is a measure of resistivity dependency on the angle of intrinsic magnetization and angle of current flow in the magnetic material. Both negative [93, 94] and positive [95] magnetoresistance (MR) were reported in graphene nanoribbons. Liu et al. reported AMR in multilayer exfoliated graphene due to anisotropic scattering of carriers from the asymmetric edges of irregularly shaped graphene sample and the boundaries of voltage electrodes [96]. Magnetization or AMR are not reported so far in monolayer CVD graphene.

Synthesis of nitrogen doped graphene has been reported experimentally [10, 97] but no evidence of ferromagnetism has been reported. Introduction of magnetization in CVD graphene, which is scalable, would open up avenues for graphene in nano-magnetic applications, such as in spin logic devices.

2.6.3 Chemical Applications

Functionalization make graphene chemically active. Functionalized graphene can be used in the field of chemical engineering as catalyst [98, 99, 100, 101] and for sensing gases and chemicals, like NO₂ gas [102, 103], NH₃ gas [104], CH₄ gas [105], hydrogen gas [106], acetone [107], and formaldehyde [108]. Functionalized graphene has also been used for the measurement of humidity [109], and pH [110, 111].

2.6.4 Biomedical Applications

Functionalized graphene can be used for biomedical applications [112]. Non-covalent functionalization is due to weak bonding and doesn't affect the electronic properties of graphene but increase the reactivity of graphene. So it can be used in sensing applications. Organic molecules like DNA form non-covalent bonding easily with graphene and can be used for bio imaging [21, 113], biosensing [114, 111, 115, 116], and drug delivery [117, 118, 119].

2.6.5 Summary

Graphene can be functionalized with different atoms and molecules via different functionalization techniques include chemical and physical methods. Functionalization change the hybridization of graphene and manipulate the properties of pristine graphene, which can be used in many applications such as in electronics, sensing, and spintronics. Most of the functionalization techniques used for graphene degrade the graphene performance mainly in terms of charge carrier mobility. Most important is to functionalize graphene with out any damages and with less or no degradation in graphene performance.

Based on the literature review, we identify the following opportunities for further explorations:

1. Functionalization of graphene without any damages and degradation in the performance of graphene.
2. Hydroxylation of CVD and exfoliated graphene is not yet reported.
3. Possibility of opening a bandgap in graphene after functionalization.
4. Possibility to dope the graphene after functionalization.
5. Application of functionalized graphene for hydrogen storage.
6. High ON to OFF current ratio in functionalized graphene FET.
7. Applications of functionalized graphene in the field of gas sensors.
8. Applications of functionalized graphene in the field of spintronics.
9. Applications of functionalized graphene for biosensors and bio-medical devices.

This thesis address (1), (2), (4), (7) and (8).

Chapter 3

Functionalization of Graphene

As discussed in chapters 1 and 2, graphene possesses zero band gap and defect free graphene is not chemically reactive, which restrict the use of pristine graphene in the field of semiconductors and sensors. Via functionalization, one can manipulate the electronic, chemical, magnetic and physical properties of graphene. This chapter describe two methods for hydroxyl functionalization of graphene: (i) by heating in H_2O_2 [120] and (ii) by a UV assisted photo-chemical method [121]. Heating method was found to damage the graphene whereas the photo-chemical method result in functionalization without any physical damage to graphene. As-grown graphene on copper foil and transferred graphene on SiO_2/Si were functionalized. characterization of hydroxyl functionalized graphene was carried out using Raman spectroscopy and XPS.

3.1 Graphene Sample Preparation

Two types of graphene were used, (i) CVD graphene and (ii) exfoliated graphene. Before proceeding to actual experimental techniques of graphene functionalization, graphene samples preparation process for both types of graphene are described in this section. The same sample preparation process was followed throughout the thesis work.

3.1.1 CVD graphene

Large area monolayer CVD graphene on copper foil was procured from Graphenea S.A. Spain. For functionalization, the CVD graphene was used on copper foil as well as transferred onto the SiO₂/Si. For transfer of CVD graphene from Cu foil, standard wet chemical etching procedure was used [122]. Schematic of transfer process is shown in figure 3.1 and step by step transfer process is describe below:

1. Radio Corporation of America (RCA) cleaning was done on p-type (100) silicon substrate of 0.001–0.005 Ω -cm resistivity.
2. A 90 nm thick layer of SiO₂ was grown on Si in the O₂ ambient at 1100°C.
3. Forming Gas Annealing (FGA) was done after oxidation at 300°C for 1 hour in H₂ + N₂ (5% H₂) ambient.
4. A 2 μ m layer of PMMA (4%) was spin coated on to the graphene/Cu at a speed of 3200 rpm for 60 sec and baked at 180°C for 3 minutes.
5. Stack of PMMA/graphene/Cu was allowed to float onto an iron trichloride based copper etchant in a petri dish which results in etching of copper foil from the bottom of the graphene and a semitransparent PMMA/graphene stack remained floating.
6. PMMA/graphene stack was scooped onto the SiO₂/Si substrate after three times rinsing with DI water.
7. Now PMMA/graphene/SiO₂/Si sample was kept for drying naturally for 12 hours in a low humid environment to remove water from the graphene - SiO₂ interface.
8. PMMA layer was removed subsequently in acetone, by heating in acetone at 70°C for 30 minutes followed by cleaning with IPA and DI water. To remove PMMA residues from graphene surface, samples were also kept in acetone overnight.

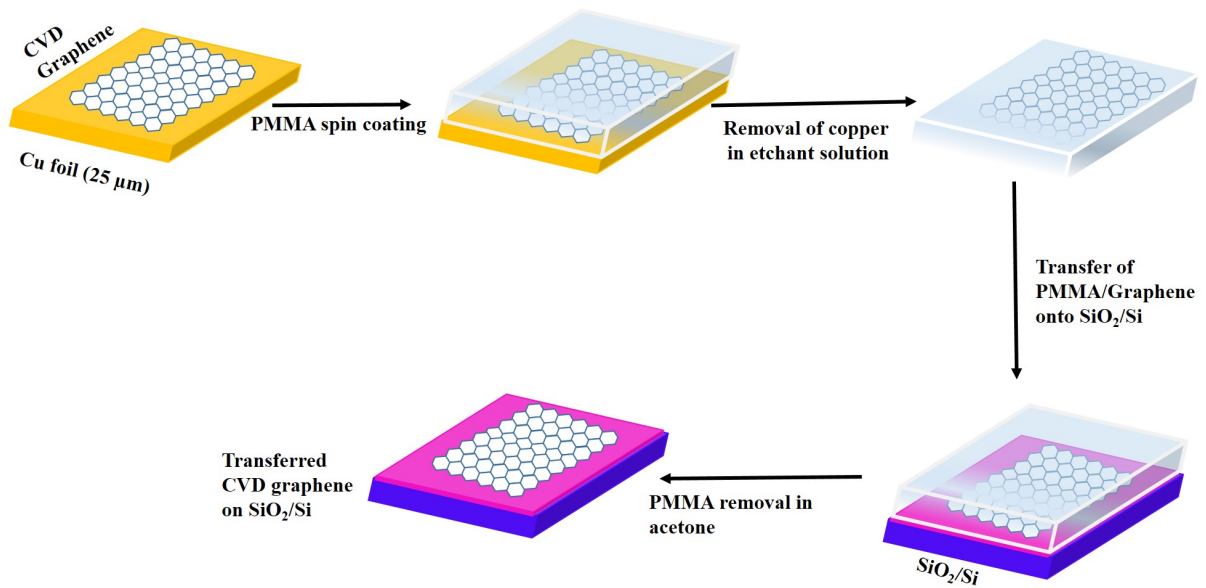


Figure 3.1: A schematic of transfer of CVD graphene onto SiO₂/Si substrate from copper foil (dimensions are not upto the scale).

An optical image of transferred CVD graphene on SiO₂ is shown in figure 3.2. Surface treatment of SiO₂ with oxygen plasma was done before graphene transfer to remove any contamination from the surface and make the SiO₂ surface rough, which enhanced the adhesion of CVD graphene with SiO₂ surface. But this practice of plasma treatment was discontinued later because it affect the graphene transistors performance, as explained in detail in Appendix B.

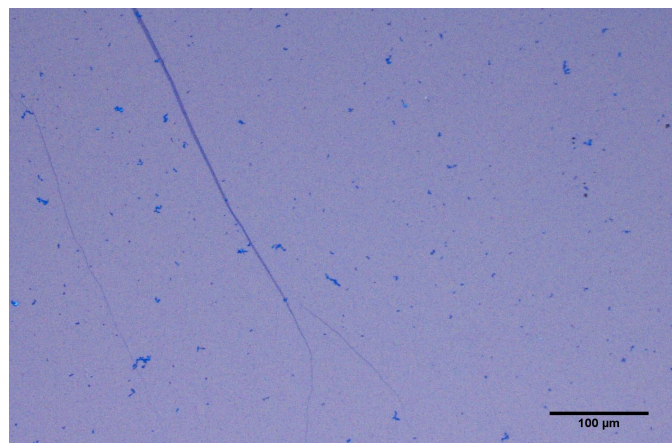


Figure 3.2: An optical image of CVD graphene transferred onto SiO₂.

3.1.2 Exfoliated Graphene

Exfoliated graphene samples were prepared using scotch tape method by mechanical exfoliation of graphene flakes from Highly Oriented Pyrolytic Graphite (HOPG) and transferred onto the SiO₂/Si substrate. The SiO₂/Si substrate was prepared by the same procedure as describe in section 3.1.1. An optical microscope image of exfoliated graphene on SiO₂/Si is shown in figure 3.3. Different colors can be seen in the images, this is because of different number of graphene layers present on SiO₂ surface. Color contrast between SiO₂ surface and graphene is dependent on the numbers of layers of graphene present on the SiO₂ surface, and it is helpful for examining the number of layers and identify the monolayers.

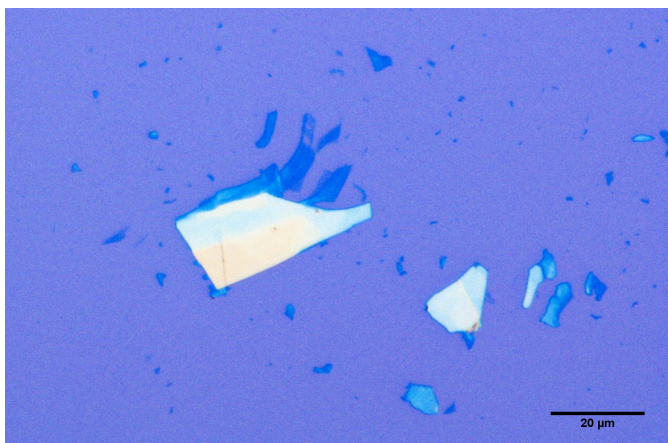


Figure 3.3: An optical image of exfoliated graphene on SiO₂. Here different colors indicate different numbers of graphene layers present.

3.2 Functionalization of Graphene with Hydroxyl Groups and Characterization

3.2.1 Thermal Treatment in H₂O₂

Functionalization of CVD graphene by hydroxyl groups was achieved by heating CVD graphene in H₂O₂ at different temperatures and for different time periods. Two types of samples were prepared (i) heating of CVD graphene on copper foil and then transfer onto SiO₂/Si substrate, figure 3.4 (a), and (ii) CVD graphene was first transferred onto

3.2. FUNCTIONALIZATION OF GRAPHENE WITH HYDROXYL GROUPS AND CHARACTERIZATION

SiO₂/Si substrate and then heated in H₂O₂, figure 3.4 (b). Thermal treatments were performed at temperatures in the range of room temperature (RT), 45°C and 60°C for duration of 30 min and 1 hr. Functionalized graphene was transferred onto SiO₂/Si substrates using method explained in section 3.1.1.

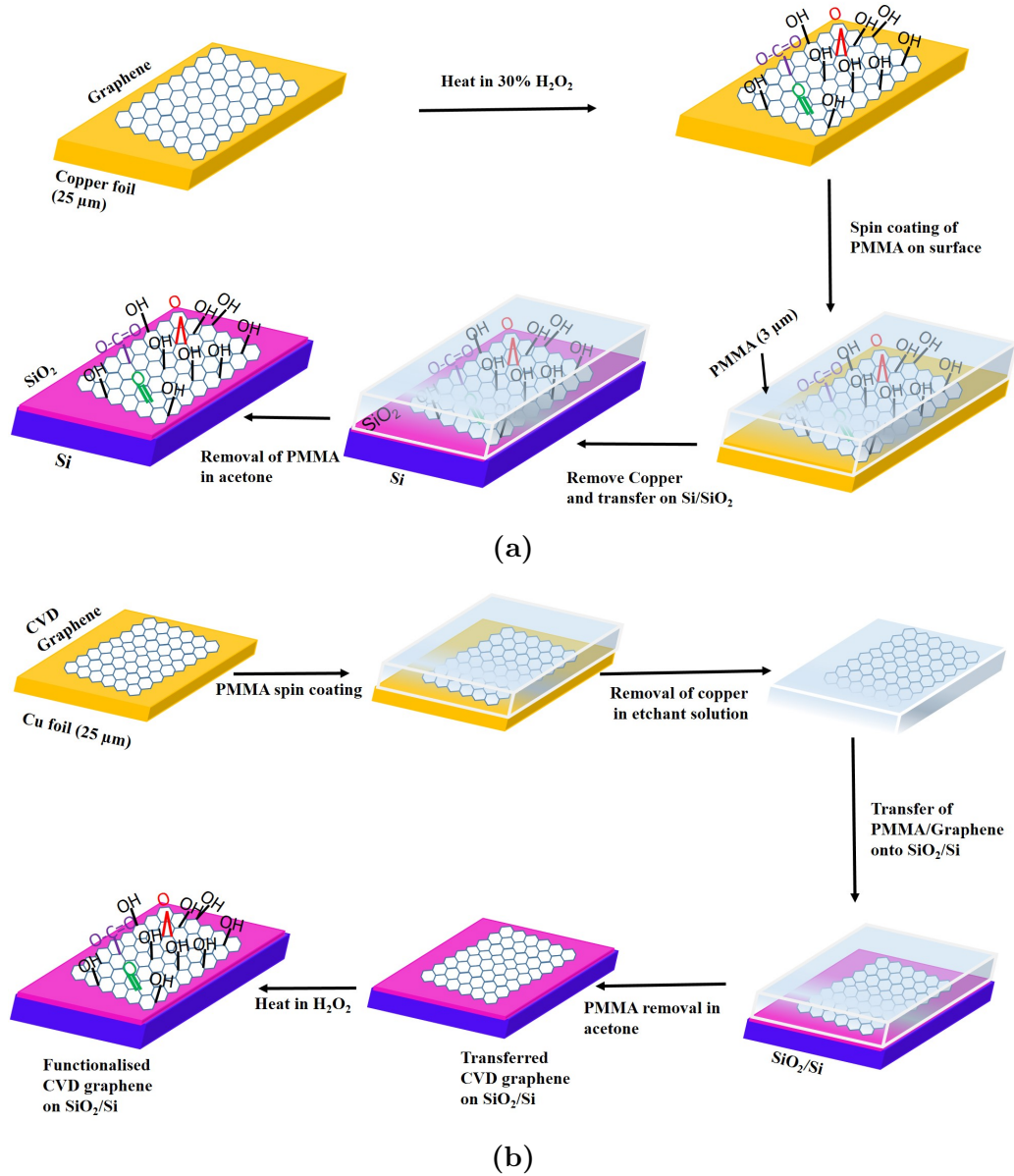


Figure 3.4: Schematic representation of two types of functionalized CVD graphene samples prepared via thermal process (a) hydroxylation of graphene on copper foil and then transfer onto SiO₂/Si. (b) hydroxylation of CVD graphene after transfer onto SiO₂/Si.

Characterization

Raman spectroscopy and XPS were used to characterize the graphene before and after functionalization.

Raman Spectroscopy

Pristine single layer graphene comprises of six-member hexagonal rings of carbon atoms in the sp^2 -hybridized state where each carbon atom is attached to three other carbon atoms. Raman spectroscopy is a well-established technique for investigating the properties of graphene[49, 122] . This technique is able to identify graphene from graphite and the number of layers in graphene. It is sensitive to defects, excess charge (doping), strain and to the atomic arrangement of the edges.

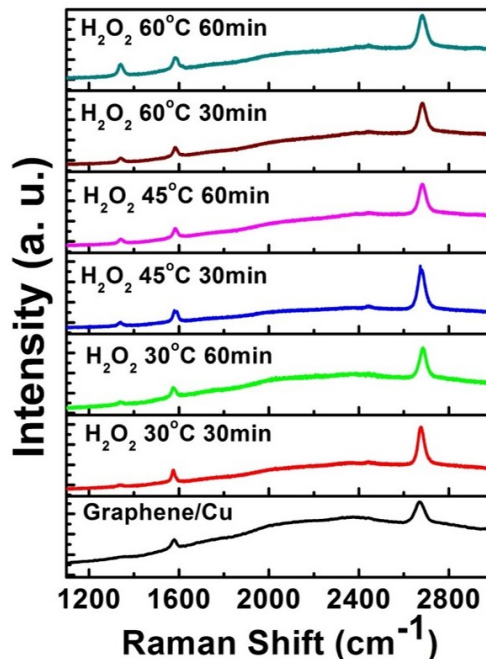


Figure 3.5: Raman spectra for pristine graphene on Cu foil and graphene on Cu foil after treatment with H_2O_2 for different time periods and temperatures, an increase in D peak intensity can be noticed with treatment.

Raman spectrum of pristine graphene on copper substrate shows characteristic vibrational modes as G band and 2D band and Raman intensity is negligible for D mode in case of perfect graphene, figure 3.5. Hydroxylation results in disorder in graphene and D peak becomes active in the presence of disorder. D peak intensity increases monotonously

3.2. FUNCTIONALIZATION OF GRAPHENE WITH HYDROXYL GROUPS AND CHARACTERIZATION

with increase in temperature and time of H_2O_2 treatment as shown in figure 3.5. This implies more hydroxyl groups are attached on graphene with the increase in temperature and time. The degree of functionalization due to various treatment conditions of H_2O_2 is estimated from I_D/I_G ratio, where I_D and I_G are the intensities of D peak and G peak respectively, as shown in figure 3.6. The ratio of I_D/I_G for perfect graphene on copper sample is 0.16 which increases to 0.7 for graphene on copper sample treated with H_2O_2 at 60°C for 60 mins. This indicates hydroxyl functionalization changes sp^2 hybridized carbon atom to sp^3 hybridized [13].

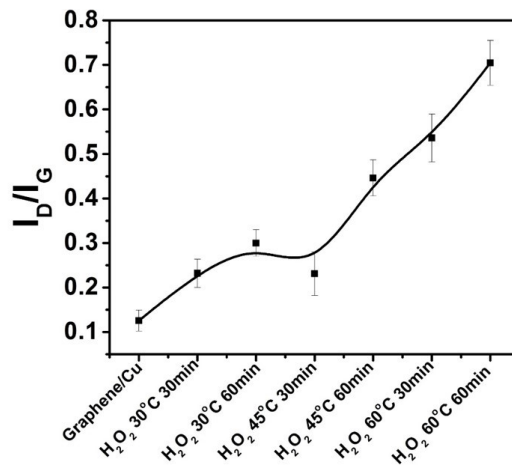


Figure 3.6: I_D/I_G ratio for pristine graphene on Cu foil and graphene on Cu foil after treatment with H_2O_2 for different time periods and temperatures, I_D/I_G ratio increases after increasing reaction time and temperature.

X-ray Photoelectron Spectroscopy

Surface chemical composition and bonding of graphene and functionalized graphene were studied using XPS. Figure 3.7 shows C 1s XPS spectra for pristine graphene on Cu foil and graphene on Cu foil after H_2O_2 treatment at 60°C for 60 minutes. The C 1s XPS spectra was deconvoluted into five peaks corresponding to sp^2 hybridized carbon atoms, C-OH, C-O-C, C=O, and -O-C=O at 284.4 eV, 285.3 eV, 286.2 eV, 287.4 eV, and 288.6 eV respectively. In table 3.1 C 1s XPS peak positions and bond configuration of graphene before and after functionalization for different time periods and at different temperatures is shown. Chemical changes introduced in graphene due to H_2O_2 treatment are easily observed by examining C 1s XPS spectra. H_2O_2 treatment at 60°C increases the C-OH

3.2. FUNCTIONALIZATION OF GRAPHENE WITH HYDROXYL GROUPS AND CHARACTERIZATION

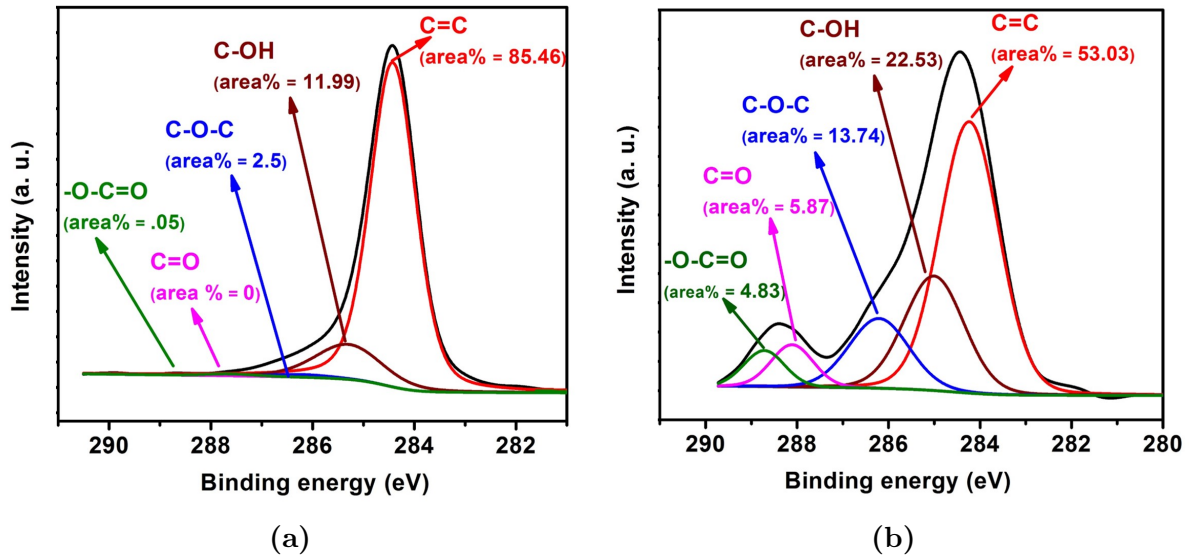


Figure 3.7: C 1s XPS spectra of (a) pristine CVD graphene on copper foil and (b) CVD graphene on copper foil after hydroxylation shows increase of C-OH bonds after reaction with H_2O_2 .

concentration from 11.99 % to 27.64 % and 22.53 % for 30 minutes and 60 minutes of treatment respectively.

Table 3.1: C 1s XPS peak positions and bond configuration of graphene on Cu foil before and after functionalization.

Bond position(eV)	Bond Name	Pristine Graphene	30 °C, 30 min	30 °C, 60 min,	60 °C, 30 min	60 °C, 60 min
284.4	sp^2	85.46	72.37	78.67	60.3	53.03
285.3	C-OH	11.99	12.52	10.85	27.64	22.53
286.2	C-O-C	2.50	6.38	1.52	6.23	13.74
287.4	C=O	0	1.51	1.11	2.52	5.87
288.6	-O-C=O	0.05	7.23	7.85	3.31	4.83

Heating in H_2O_2 results in delamination of CVD graphene from some area, as can be seen in figure 3.8 (b) and complete removal of exfoliated graphene from SiO_2 surface. Thermal treatment damages both CVD graphene on copper foil and on SiO_2/Si substrate. As-transferred CVD graphene on SiO_2 is shown in figure 3.8 (a) and after heating in H_2O_2 at $600^\circ C$ for 30 minutes in figure 3.8 (b). Physical damages (mostly circular in shape) to transferred graphene is clearly visible. These damages are mainly due to rigorous

3.2. FUNCTIONALIZATION OF GRAPHENE WITH HYDROXYL GROUPS AND CHARACTERIZATION

decomposition of H_2O_2 when heated. In case of copper foil, Cu act as catalyst for H_2O_2 dissociation. H_2 and O_2 bubbles formed by the rigorous reaction scratch the surface of the sample, resulting in damage to graphene.

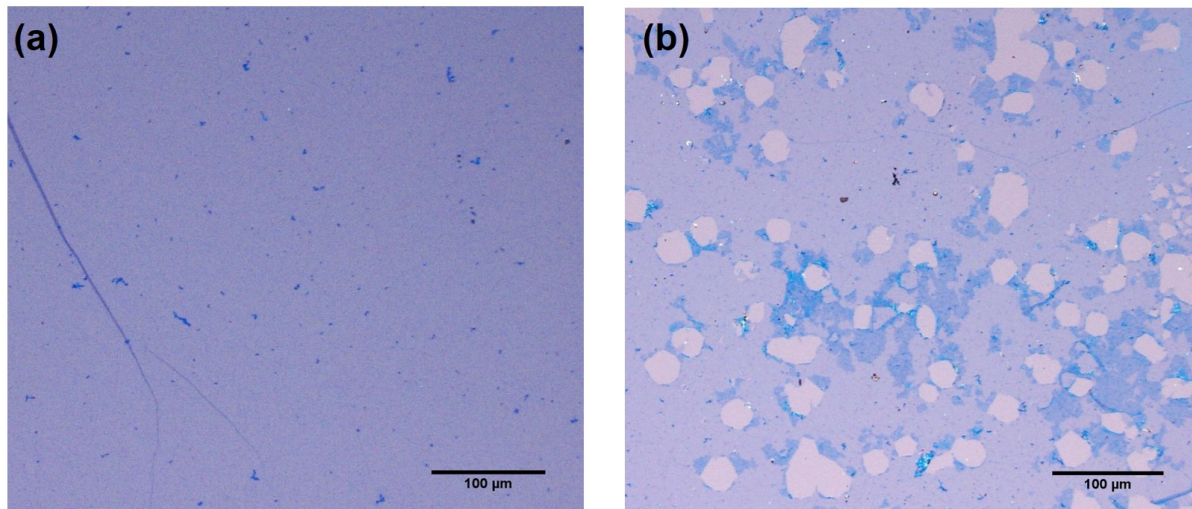


Figure 3.8: An optical image of (a) as transferred CVD graphene on SiO_2 (b) transferred graphene on SiO_2 after heating in H_2O_2 at 60°C for 30 minutes, circular shape damage to graphene can be seen after heating in H_2O_2 .

3.2.2 UV Assisted Photo-chemical Method

For UV assisted hydroxylation of graphene, (a) CVD graphene transferred onto the SiO_2/Si and (b) exfoliated graphene on SiO_2/Si were treated with 30% hydrogen peroxide for various time periods in the presence of UV light with a wavelength of 256 nm and 365 nm at room temperature. A schematic representation for UV assisted hydroxylation of CVD and exfoliated graphene is shown in figure 3.9.

3.2. FUNCTIONALIZATION OF GRAPHENE WITH HYDROXYL GROUPS AND CHARACTERIZATION

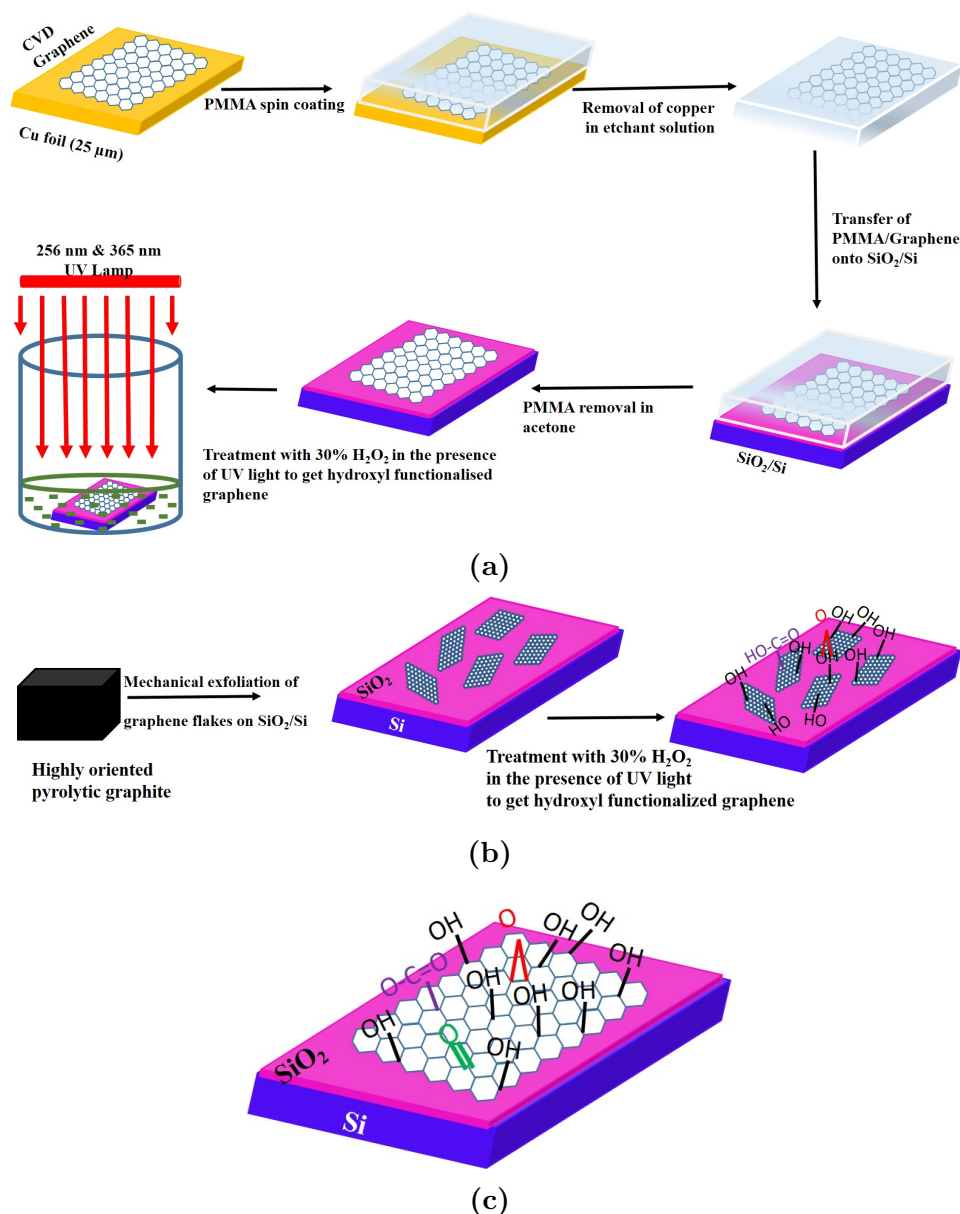


Figure 3.9: Schematic representation of (a) hydroxylation of CVD graphene via treatment with H₂O₂ in the presence of UV light, (b) hydroxylation of exfoliated graphene via treatment with H₂O₂ in the presence of UV light, (c) graphene after hydroxylation.

Characterization of CVD and Exfoliated Graphene on SiO₂/Si

Figure 3.10 shows C 1s XPS spectra of pristine CVD graphene after different types of H₂O₂ treatments. The XPS spectra were deconvoluted into five peaks. Graphene exhibits presence of sp² carbon bonds at 284.6 eV [123, 124]. Deconvolution of C 1s spectra reveal additional peaks at 285.5 eV (C-OH), 286.4 eV (C-O-C), 287.6 eV (C=O)

3.2. FUNCTIONALIZATION OF GRAPHENE WITH HYDROXYL GROUPS AND CHARACTERIZATION

and 288.8 eV (-O-C=O) [123]. C 1s XPS spectra was shifted to 284.6 eV binding energy before deconvolution to compensate for the positive charge buildup on the surface by emission of electrons during spectroscopy [125].

Figure 3.10 (a) shows C 1s XPS spectra of pristine CVD graphene and CVD graphene after treatment only with H₂O₂ for 30 minutes. Both spectra overlap each other implying no change in the carbon bonding after H₂O₂ treatment. However when the H₂O₂ treatment was carried out in the presence of UV light, the XPS peak corresponding to C-OH is seen to be enhanced, see figures 3.10 (c) and 3.10 (d). Table 3.2 shows the different peaks' positions for deconvoluted XPS spectra of carbon and relative area of each peak for pristine CVD graphene, CVD graphene after 30 minutes of treatment in H₂O₂, and after 15 and 30 minutes of H₂O₂ treatment in the presence of UV light. For pristine graphene, various types of carbon to oxygen bonds constituted 30.65 % of the C 1s spectrum. This is quite comparable to other reports in the literature for transferred CVD graphene [124]. It is seen that H₂O₂ treatment alone without UV light for 30 minutes do not change the total carbon to oxygen bond concentration. More detailed analysis, result of which is given in table 3.2, also indicate that the concentration of various types of carbon to oxygen bonds in the pristine CVD graphene do not change with only H₂O₂ treatment. This implies that the treatment of CVD graphene only with H₂O₂ at room temperature is not sufficient to functionalized the graphene. On the other hand, H₂O₂ treatment in the presence of UV light enhances the C-OH concentration from 10.37 % to 17.15 % and from 10.37% to 20.87 % for 15 minutes and 30 minutes of treatment respectively. This is also accompanied by a small decrease in the C-O-C bonds and a small increase in the C=O bonds.

Table 3.2: Relative peak area for each denconvoluted peak of C 1s spectra of CVD graphene before and after different H₂O₂ treatments at room temperature.

Bond position(eV)	Bond Name	Pristine CVD graphene	after 30 min of only H ₂ O ₂	after 15 min of H ₂ O ₂ + UV	after 30 min of H ₂ O ₂ + UV
284.6	sp ² C	69.35	69.13	67.33	62.3
285.5 ± 0.1	C-OH	10.70	11.98	17.15	20.87
286.4 ± 0.1	C-O-C	13.34	13.50	8.25	9.07
287.6 ± 0.1	C=O	0	0	2.2	2.81
288.8 ± 0.1	-O-C=O	6.61	5.39	5.06	4.93

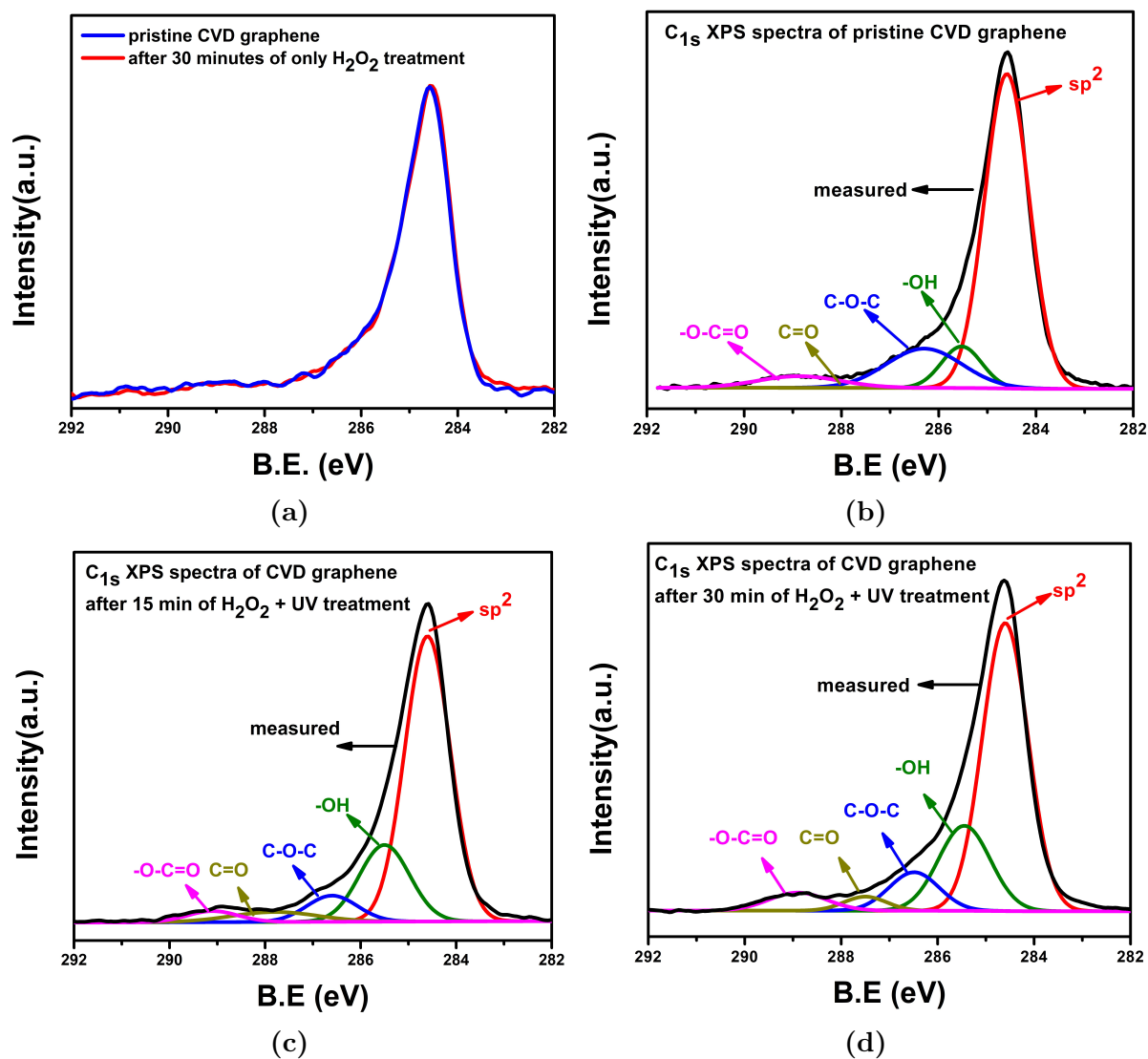


Figure 3.10: (a) C 1s XPS spectra of pristine CVD graphene and CVD graphene after treatment with only H₂O₂ for 30 minutes at RT shows no affect of H₂O₂ (b) deconvoluted C 1s XPS spectra of pristine CVD graphene, and (c,d) CVD graphene after 15 minutes and 30 minutes of H₂O₂ treatment in the presence of UV light shows increase in oxygen containing functional groups.

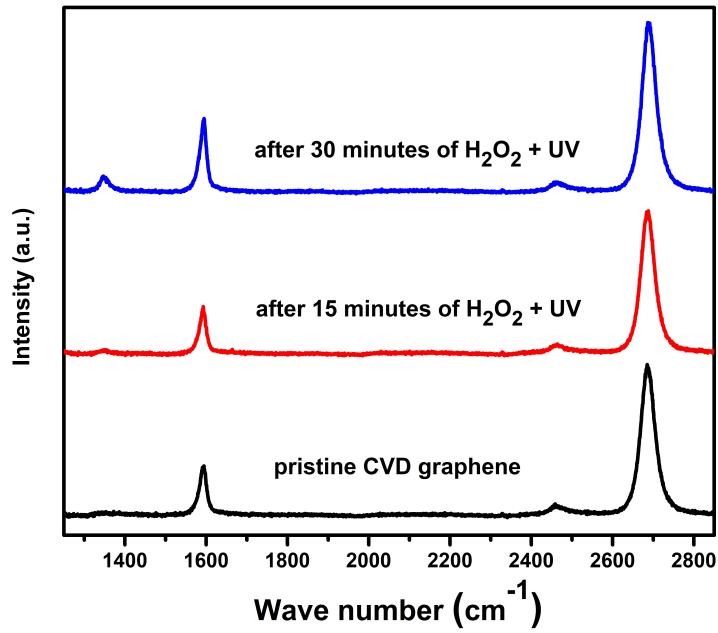


Figure 3.11: Raman spectra of CVD graphene before hydroxylation and after hydroxylation for different time periods.

Raman spectra for CVD graphene and exfoliated graphene before and after treatment with H₂O₂ in the presence of UV light for different time periods is shown in figures 3.11 and 3.12. A small defect peak (D peak) appears after hydroxylation. I_D/I_G ratio increases from 0 for pristine CVD graphene to 0.1 and 0.3 for 15 minutes and 30 minutes of treatment respectively. For exfoliated graphene I_D/I_G ratio is seen to be 0.06 for pristine which increases to 0.23, 0.46 and 0.56 for one, two and three hours of treatment respectively. D peak is due to intervalley resonant Raman scattering and needs defects in graphene lattice for activation [126]. Defects can be vacancies, grain boundaries or a break in the graphene lattice sp^2 symmetry. The intensity of D peak (I_D) represents the amount of non- sp^2 bonding [126]. The ratio of area of D and G peaks (I_D/I_G) can be considered as a measure of the ratio of non- sp^2 to sp^2 bonding carbon atoms [127]. Raman results are consistent with XPS results, as $-OH$ functional groups make one extra sigma bond with carbon atom of graphene lattice by sp^3 hybridization. Thus the increase in I_D/I_G ratio indicates the adsorption of a significant amount of functional groups ($-OH$) on the CVD graphene lattice which lead to a change in hybridization from sp^2 to sp^3 by covalent bonding of hydroxyl groups with the carbon atoms of graphene lattice.

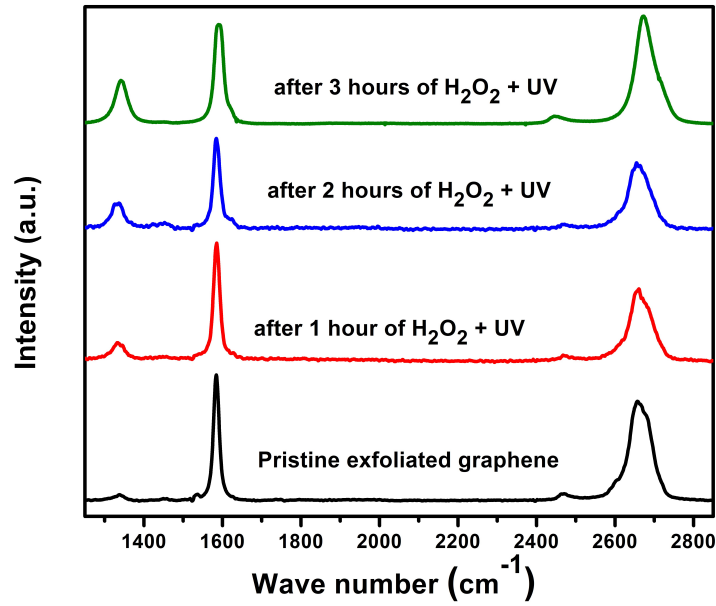


Figure 3.12: Raman spectra of exfoliated graphene before and after hydroxylation for different time periods.

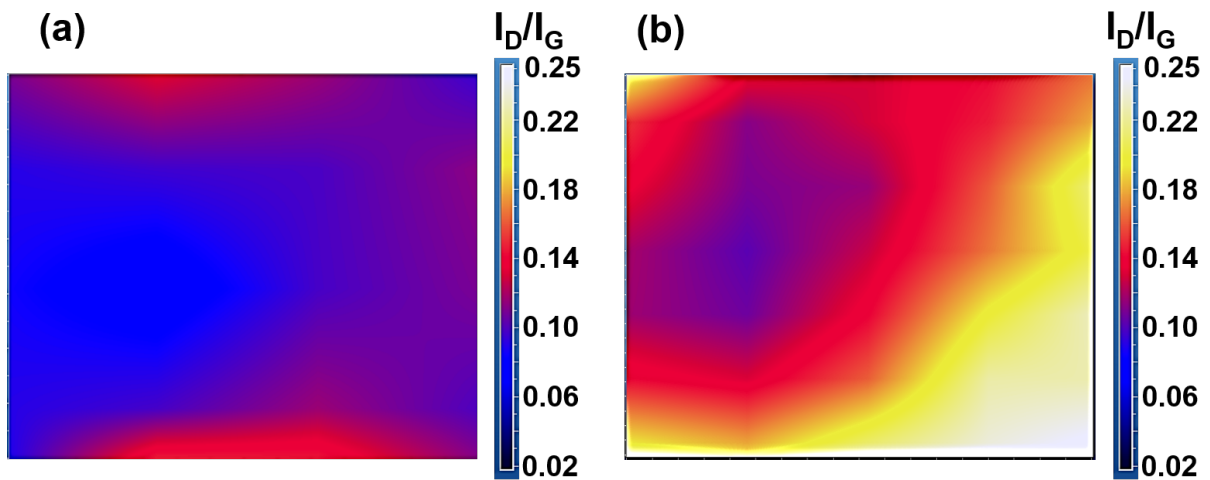


Figure 3.13: Raman map of I_D/I_G ratio for $4 \mu\text{m} \times 4 \mu\text{m}$ scan area of CVD graphene (a) before hydroxylation, and (b) after hydroxylation.

Figure 3.13 shows the Raman map of I_D/I_G ratio for $4 \mu\text{m} \times 4 \mu\text{m}$ area of CVD graphene before and after 15 minutes of hydroxylation in the presence of UV light. Scale of both images has been kept same for fair comparison. For pristine graphene, most of the area have I_D/I_G in the range of 0.04 to 0.10 which increase to a range of 0.10 to 0.25 after hydroxylation. This strongly indicates the formation of sp^3 hybridized carbon bonds by a change in hybridization from sp^2 .

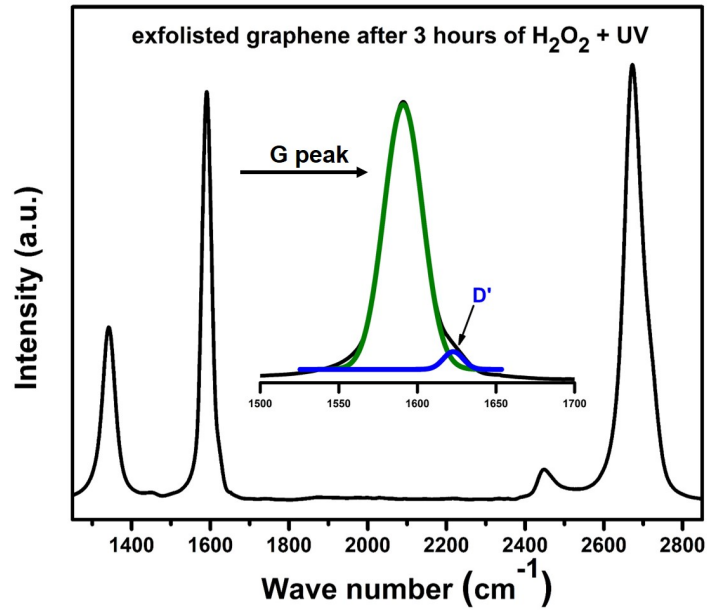


Figure 3.14: Raman spectra of exfoliated graphene after three hours of H₂O₂ treatment in the presence of UV light. Inset shows the deconvoluted G peak. The black line is measured spectrum, the green and blue lines are the deconvoluted peaks.

In case of CVD graphene, the G peak position shifts from 1592.7 cm⁻¹ for pristine to 1594.3 cm⁻¹ for CVD graphene treated with H₂O₂ in the presence of UV light for 30 minutes and for exfoliated graphene from 1582.9 cm⁻¹ to 1591 cm⁻¹ after three hours of treatment. This blueshift in G peak position indicates p-type doping of graphene.

Figure 3.15 shows Raman map for G peak position of pristine CVD graphene and CVD graphene after hydroxylation. For pristine CVD graphene the G peak position is at the same value except at the edges and after hydroxylation there is a blueshift in the G peak position throughout the graphene. Shift in G peak position is uniform which indicates uniform p-type doping of graphene [51]. Figure 3.14 shows a more detailed analysis of exfoliated graphene after 3 hours of treatment. A disorder peak, D', appears after deconvolution of G peak as shown in the inset of figure 3.14. D' peak is due to intravalley resonant Raman scattering and get activated only if defects are present in graphene [127]. Exfoliated graphene after one hour and two hours of treatment also shows similar appearance of D' peak. A new peak, D + D', also appears at 2900 cm⁻¹ only in case of three hours of treatment, figure 3.14.

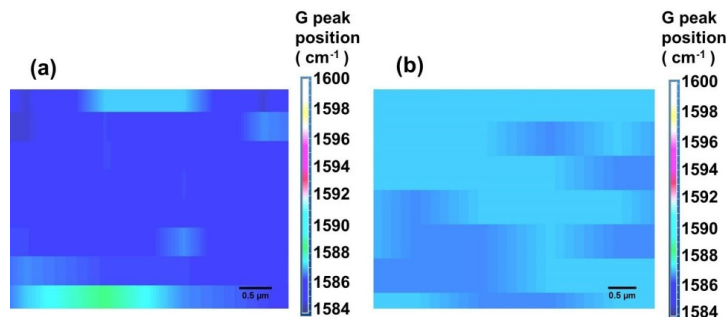
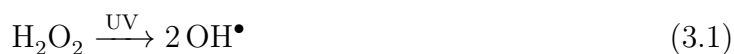


Figure 3.15: Raman map of G peak position of (a) pristine CVD graphene (b) hydroxyl functionalized CVD graphene. Shows shift in G peak position after hydroxylation.

Discussion

The photolysis of H_2O_2 is reported to result in the generation of -OH radicals and the reaction is represented as follows [89].



Final products of H_2O_2 decomposition are water and oxygen. Bond dissociation enthalpy (BDE) for HO-OH bond in H_2O_2 is 47 kcal/mol [128]. However the BDE of H-O bond in H_2O_2 is similar to BDE of H-OH bond in water [129], which is 470 kcal/mol [130]. When H_2O_2 decomposition occurs in the presence of UV light, the HO-OH bonds break first and produces -OH radicals.

Graphene lattice has sp^2 hybridized carbon where each carbon atom makes three covalent sigma bonds with neighboring carbon atoms and have one free electron present in 2p_z orbital which make π bond with one of the neighboring carbon atoms. Hydroxyl radicals can make covalent bonds with carbon atoms by sharing an electron with 2p_z orbital which results in fourth sigma bond by sp^3 hybridization. Also they make bonds with carbon atoms at defect sites and edges of graphene very easily. Mechanism for addition of hydroxyl radical to a sp^2 hybridized aromatic ring of graphene is shown in figure 3.16.

3.2. FUNCTIONALIZATION OF GRAPHENE WITH HYDROXYL GROUPS AND CHARACTERIZATION

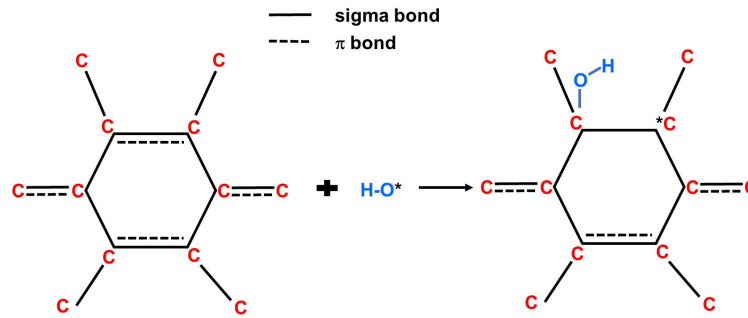
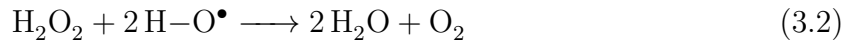


Figure 3.16: Mechanism of -OH radical addition to one ring of graphene. -OH radical generated via decomposition of H_2O_2 .



-OH radicals also reacts with the H_2O_2 and produce H_2O and O_2 , as shown in chemical equation (3.2). Oxygen can react with electrons and undergoes reduction to form species such as peroxide ions (O_2^{2-}) and superoxide ions (O_2^-). Oxygen ions result in functionalization of graphene by carbonyl groups.

Decomposition of H_2O_2 also occurs naturally at room temperature but at a very slow rate. Hence a longer time may be required for functionalization of graphene by treating with only H_2O_2 at room temperature whereas heating increase the decomposition rate of H_2O_2 . However heating in H_2O_2 results in delamination of CVD graphene and complete removal of exfoliated graphene from SiO_2 surface, as shown in figure 3.8. No sign of physical damage to graphene is seen after treatment of transferred graphene with H_2O_2 in the presence of UV light, figure 3.17 (a) and with only H_2O_2 at room temperature for 30 minutes, figure 3.17 (b).

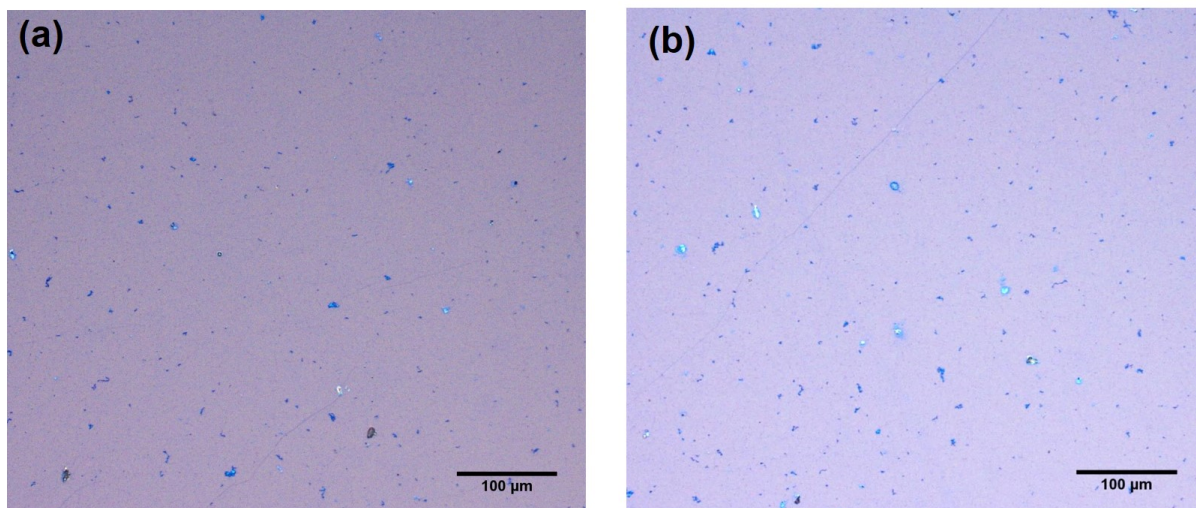


Figure 3.17: Optical image of CVD graphene on SiO₂ (a) after treatment of transferred graphene with H₂O₂ in the presence of UV light and (b) with only H₂O₂ at room temperature for 30 minutes, no damages to graphene in both the cases.

3.3 Summary and Conclusions

In this chapter we have reported development of two simple process for the functionalization of CVD and exfoliated graphene with hydroxyl groups. CVD graphene on copper foil and transferred onto SiO₂/Si were used for functionalization. Functionalization was done via heating graphene in H₂O₂ and treatment of graphene with H₂O₂ at room temperature in the presence of UV light. Heating of graphene in H₂O₂ results in physical damages to graphene whereas in case of treatment in UV light no damages to graphene was observed. XPS and Raman spectroscopy was used for the confirmation of functionalization. C 1s XPS spectra shows a increase of C-OH bonds form 10.70 % to 20.87 %. Raman spectroscopy shows increase in I_D/I_G ratio form 0 to 0.3 for CVD graphene and form 0.23 to 0.56 for exfoliated graphene. Decomposition of H₂O₂ gives -OH radicals which make covalent bonds with carbon atoms of graphene and result in hydroxylation of graphene.

Chapter 4

Electrical Applications of Functionalized Graphene

4.1 Workfunction Engineering

Workfunction of graphene varies with the variation in the oxygen content in GO. Misra et al. showed variation in workfunction of GO by reducing it at different temperatures and showed that the workfunction of GO correlates with the oxygen content [18]. In our case we start from pristine graphene and then functionalized it with hydroxyl groups by treating with H_2O_2 at 60°C for 60 min. Workfunction measurement was done by Kelvin Probe Force Microscopy (KPFM) and observed a difference of 0.45 eV in workfunction of pristine and functionalized graphene.

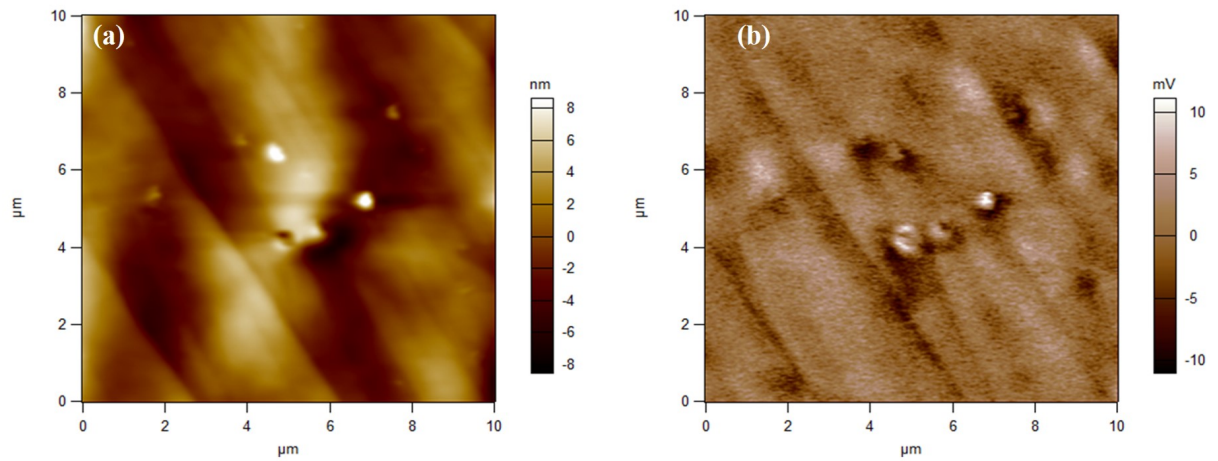


Figure 4.1: (a) Height image, obtained from AFM scan and (b) CPD image of HOPG to calculate workfunction of KPFM tip, obtained from KPFM scan.

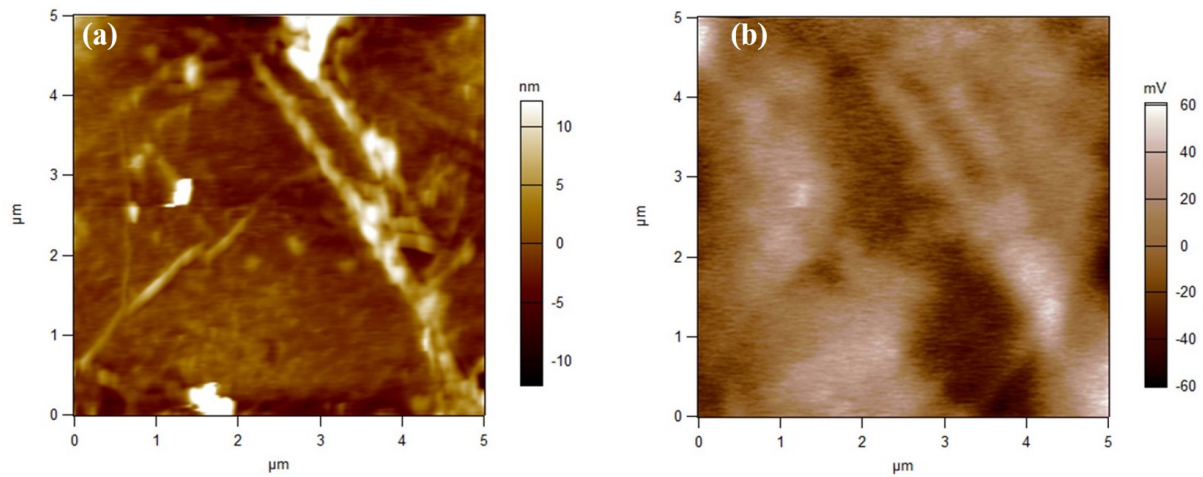


Figure 4.2: (a) Height image, obtained from AFM scan and (b) CPD image of pristine graphene, obtained from KPFM scan.

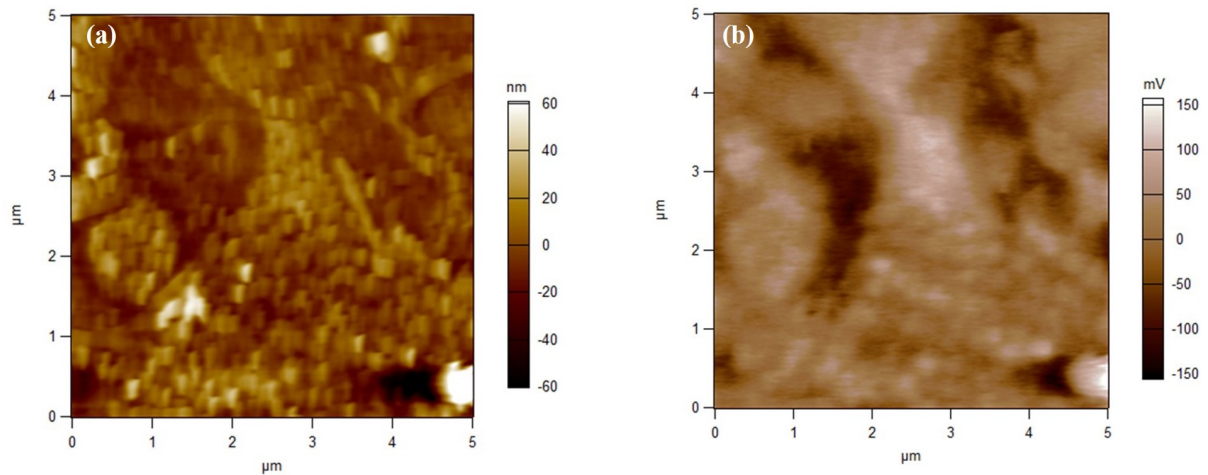


Figure 4.3: (a) Height image, obtained from AFM scan and (b) CPD image of functionalized graphene, obtained from KPFM scan.

Reference scan of HOPG (whose workfunction is already known to us) was done to calculate the workfunction of KPFM tip, figure 4.1, and we calculated the workfunction of tip as 5.1 eV. Topography and Contact Potential Difference (CPD) scan for pristine graphene and functionalized graphene is shown in figure 4.2 and 4.3 respectively. For pristine graphene RMS value of CPD were 0.318 V and 0.373 V for 1 μm and 5 μm scan area respectively. This gives workfunction of approximately 4.78 eV ($= 5.1 - 0.32$) and 4.73 eV for 1 μm and 5 μm scan area respectively. And in case of functionalized graphene the RMS value of CPD was 0.801 V and 0.722 V for 1 μm and 5 μm scan area respectively which gave a workfunction of approximately 4.3 eV and 4.38 eV. Figure 4.4 shows the analysis of CPD scan for functionalized graphene and pristine graphene. Thus there is a difference of 0.45 eV between the workfunction of pristine graphene and functionalized graphene. Workfunction of graphene reduces after functionalization. Which means there is a reduction in workfunction of graphene with a increase of oxygen concentration, whereas Misra et al. [18] and Priyank et al. [131] have shown increase in workfunction with a increase of oxygen concentration in graphene oxide. They have used thick GO and RGO for workfunction engineering with different oxygen concentration, whereas we have used monolayer CVD graphene, this might be the reason for reduction of workfunction in our case and increase of workfunction in their case with oxygen concentration. Transfer

of charge after functionalization result in change of workfunction of graphene.

Graphene treated in H_2O_2 at 60 °C for 60 min		Pristine Graphene	
Scan size = 5 μm	Scan size = 1 μm	Scan size = 5 μm	Scan size = 1 μm
Avg. Potential = 0.718 V	Avg. Potential = 0.801 V	Avg. Potential = 0.372 V	Avg. Potential = 0.313 V
RMS Potential = 0.722 V	RMS Potential = 0.801 V	RMS Potential = 0.373 V	RMS Potential = 0.318 V
WF = 5.1 – 0.72 = 4.38 eV	WF = 5.1 – 0.8 = 4.3 eV	WF = 5.1 – 0.37 = 4.73 eV	WF = 5.1 – 0.32 = 4.78 eV

Figure 4.4: Analysis of KPFM scan for pristine graphene and functionalized graphene.

4.2 Atomic Layer Deposition of Al_2O_3

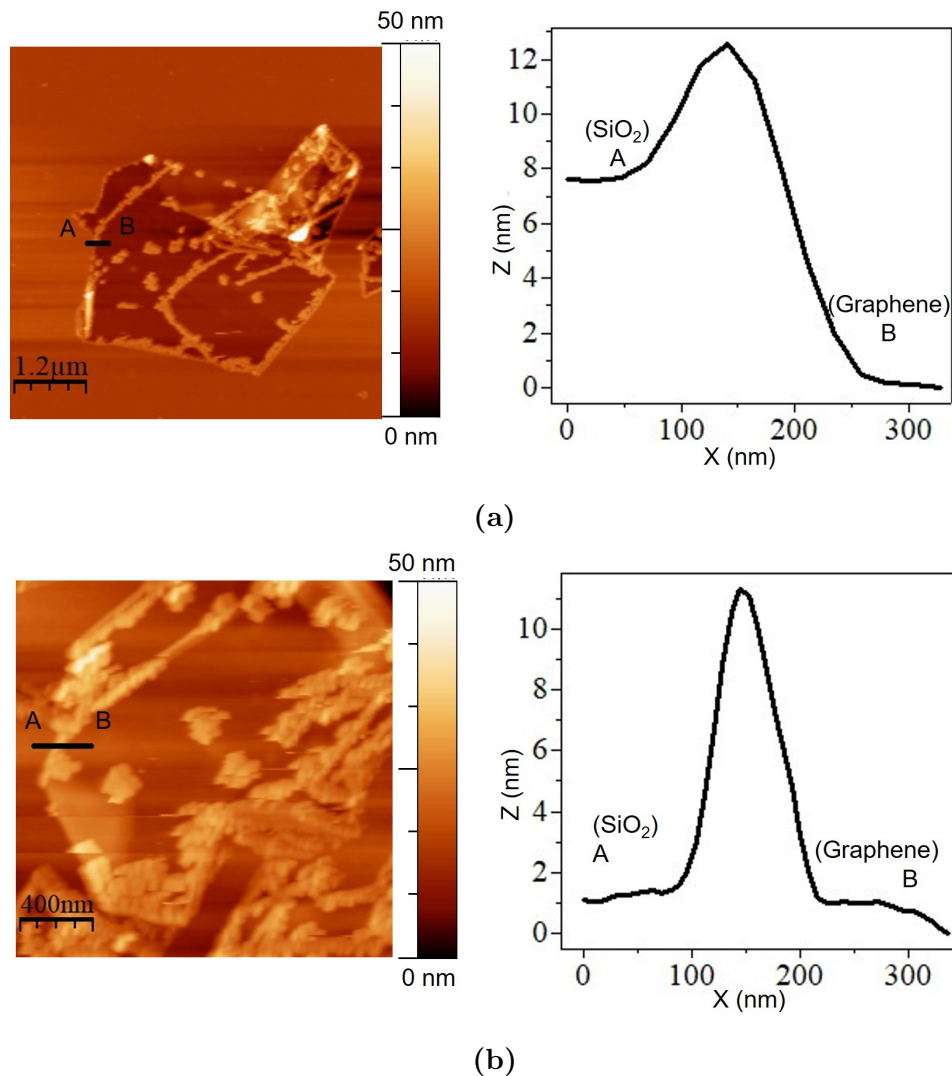


Figure 4.5: AFM line profile of the samples with Al_2O_3 deposition on the surface (a) before hydroxylation (b) after hydroxylation.

The peaks in the AFM line scans in both figures 4.5 (a) and 4.5 (b) are due to deposition at the defects at the edges of graphene. This also explain the deposition of isolated islands of Al_2O_3 on pristine graphene, figure 4.5.

Al_2O_3 was deposited on pristine exfoliated graphene and exfoliated graphene was strongly hydroxylated for one hour. Deposition was done via 100 cycles of ALD at 200°C using the Tri Methyl Aluminum (TMA) as precursor. The thickness of Al_2O_3 deposited on SiO_2 on the samples was determined as 8 nm using ellipsometry. AFM images of the two samples are shown in figure 4.5. In case of pristine graphene, the line profile shows a height difference of 8 nm between SiO_2 surface (point A) and graphene (point B), figure 4.5 (a), which matches with the value measured by ellipsometer on SiO_2 . This implies that Al_2O_3 is not deposited on pristine graphene. In the case of hydroxylated graphene, figure 4.5 (b), no height difference between graphene and SiO_2 is seen, indicating that the Al_2O_3 was deposited on the hydroxylated graphene. It is well known that the ALD deposition of Al_2O_3 using TMA require an -OH terminated surface [132].

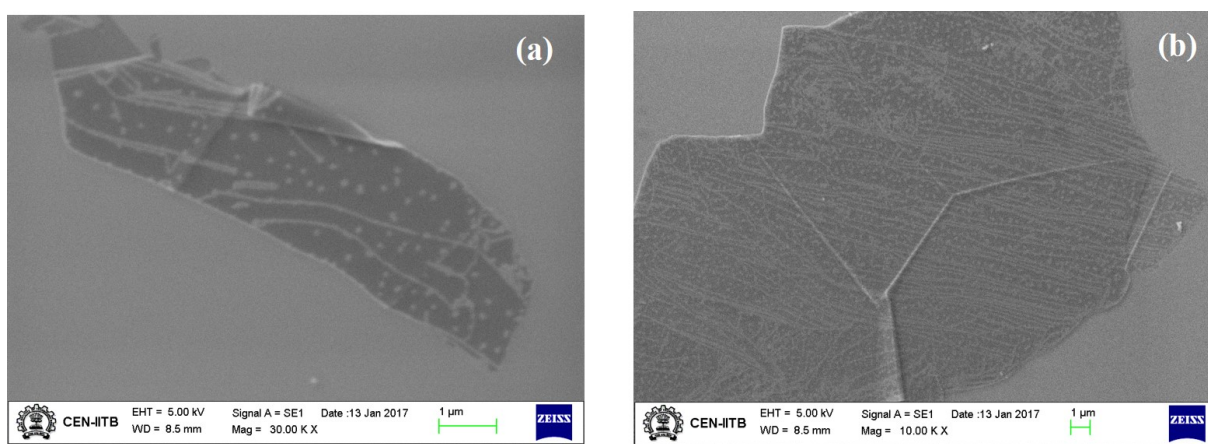


Figure 4.6: SEM images of pristine exfoliated graphene after Al_2O_3 deposition on (a) pristine graphene and (b) functionalized graphene

Figure 4.6 shows the SEM images after Al_2O_3 deposition on pristine and functionalized exfoliated graphene. In both cases there is no uniform deposition. However Al_2O_3 coverage on graphene surface increases after H_2O_2 treatment. ALD deposition is more uniform on functionalized graphene than on pristine graphene.

4.3 Graphene Field Effect Transistors (GFETs)

4.3.1 GFET Fabrication Process Flow

Silicon wafer was used as substrate for fabrication of back gated GFETs. A 90 nm thick layer of SiO₂ was grown in dry thermal O₂ ambient at 1100 °C on p-type (100) Silicon substrate of 0.001–0.005 Ω-cm resistivity. Forming gas annealing (FGA) was done after oxidation at 300 °C for 1 hour in H₂/N₂ (5% H₂) ambient. A schematic of GFET structure, is shown in figure 4.7 (a), and the fabrication steps are shown in figure 4.7 (b).

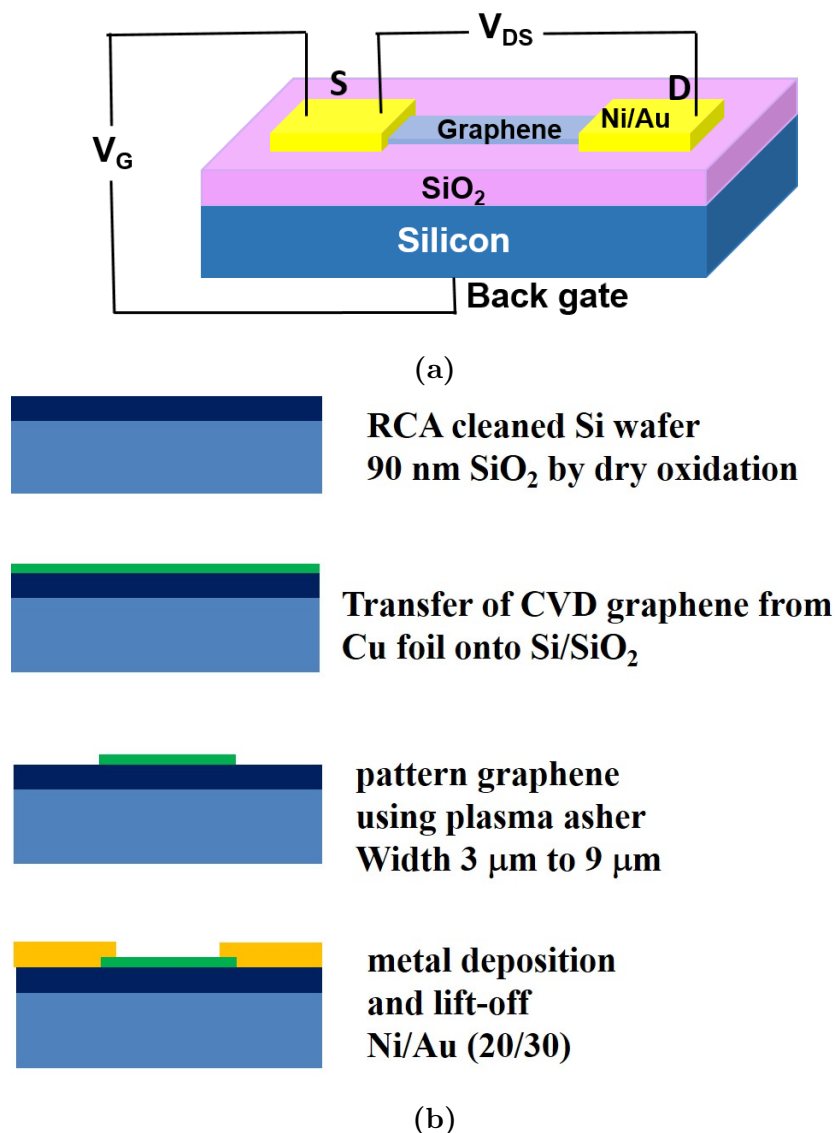


Figure 4.7: (a) Schematic of GFET device structure and (b) schematic representation of fabrication steps.

Fabrication Steps

1. Alignment Marks

First, alignment marks were fabricated on the SiO₂ surface to align subsequent lithography steps.

- (a) Cleaning of wafer with acetone, IPA and DI water respectively.
- (b) Dehydration bake at 150°C for 5 minutes.
- (c) Spin coating of AZ5214E positive photoresist at a speed of 4500 rpm for 45 sec.
- (d) Prebake at 110°C for 50 sec.
- (e) UV lithography exposure with a dose of 65 mJ/cm².
- (f) Development of resist in MF319 developer by keeping sample in vertical position. Developing time vary depending upon lab conditions, temperature and humidity. Typically when temperature was under 25°C and relative humidity less than 50 %, the development time required was 20 sec.
- (g) Etching of SiO₂ by dipping in 5% BHF. The sample was kept in vertical position because in vertical position etching rate was constant with time whereas in horizontal position it was varying with time.
- (h) Removal of photoresist in AZ100 remover.

After this step we have substrate with alignment marks etched into the SiO₂. Step-(g) also removes oxide from the backside of silicon wafer during etching oxide from the top for alignment marks.

2. Graphene Transfer

CVD graphene was used for GFET fabrication. Graphene of size 1 cm X 1 cm was transferred onto the wafer with alignment marks fabricated in step-1. Process

for CVD graphene transfer onto Si/SiO₂ substrate was already explained in section 3.1.1. SiO₂ was treated with plasma before graphene transfer to remove any contamination present on surface and to make SiO₂ surface little rough so that adhesion of CVD graphene get improved with the SiO₂ surface. But plasma treatment process affect the GFET performance, so we discontinued use of plasma treatment for fabrication of GFETs, as explained in Appendix B.

3. Graphene Patterning

- (a) Cleaning of wafer with acetone, IPA and DI water respectively.
- (b) Dehydration bake at 150°C for 5 minutes.
- (c) Spin coating of AZ5214E positive photoresist at a speed of 4500 rpm for 45 sec. AZ5214E photoresist was used because other available photoresist make graphene p-type doped, whereas after using AZ5214E we were able to obtain the Dirac point near to zero gate voltage.
- (d) Prebake at 110°C for 50 sec.
- (e) UV lithography exposure with a dose of 65 mJ/cm².
- (f) Development of resist in MF319 developer by keeping sample in vertical position. Developing time vary depending upon lab conditions, temperature and humidity. Typically when temperature was under 25°C and relative humidity less than 50 %, the development time required was 20 sec.
- (g) Etching of graphene by oxygen plasma in plasma asher for 3 minutes.
- (h) Removal of resist in AZ100 remover.

After this step we have sample with alignment marks and patterned graphene in rectangle shape. Size of graphene strips were in the range of width 3 μm to 9 μm and length from 15 μm to 40 μm . 10 μm was the overlap length of graphene for two

metal contact pads, which effectively gave channel length of 5 μm to 30 μm .

4. Metal Deposition

- (a) Cleaning of wafer with acetone, IPA and DI water respectively.
- (b) Dehydration bake at 150°C for 5 minutes.
- (c) Spin coating of AZ5214E photoresist at a speed of 5000 rpm for 45 sec. AZ5214E photoresist was used in image reversal mode i.e. as negative photoresist because AZ5214E was not leading to successful lift-off when used as positive photoresist. An under-cut or retrograde sidewall type profile is desirable for metal lift-off. When AZ5214E was used in image reversal mode, lift-off could be carried out successfully in all experiments [133]. SEM images of patterned A5214E is shown in figure 4.8. A retrograde sidewall slope is clearly visible in the case of AZ5214E image reversal mode, shown in figure 4.8 (b).
- (d) Prebake at 110°C for 50 sec.
- (e) UV lithography exposure with a dose of 65 mJ/cm².
- (f) Postbake at 110°C for 2 minutes.
- (g) Flood exposure with a dose of 170 mJ/cm².
- (h) Development of resist in MF319 developer by keeping sample in vertical position. Developing time vary depending upon lab conditions, temperature and humidity. Typically when temperature was under 25°C and relative humidity less than 50 %, the development time required was 20 sec.
- (i) Metal deposited using six target e-beam evaporator. A stack of 20 nm nickle and 30 nm gold was deposited.
- (j) For lift-off, samples were kept in AZ100 for 12 hours. No heating and sonication was done for fast lift-off because it results in delamination of graphene strips

from the substrate.

After this step we got GFETs ready for electrical characterization. Channel width of the fabricated transistors were 3, 5 and 9 μm and lengths were 5, 10, 15, 20 and 30 μm for each width. An optical image of the fabricated graphene FET is shown in figure 4.9.

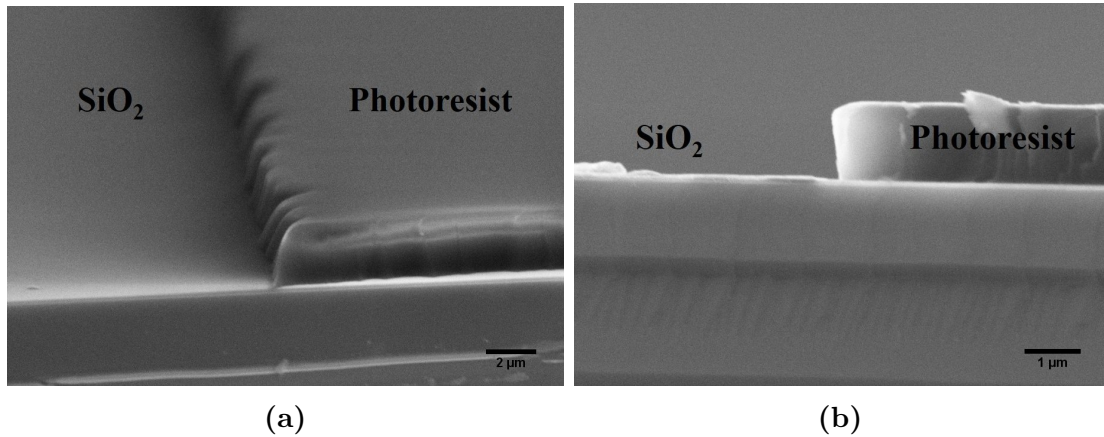


Figure 4.8: (a) SEM image of patterned AZ5214E resist when used as positive photoresist. (b) SEM image of patterned AZ5214E resist when used in image reversal mode, a retrograde sidewall slope can be seen.

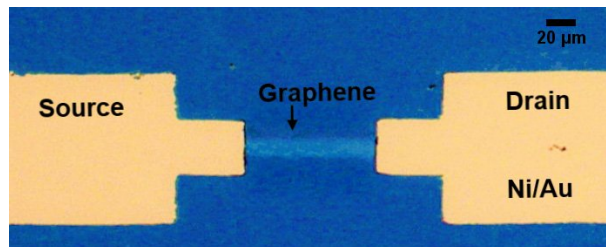


Figure 4.9: An optical image of the fabricated graphene FET.

4.3.2 Electrical Characterization of Functionalized Graphene FETs

We have shown functionalization of exfoliated graphene and CVD graphene in chapter 3. In this section the electrical characterization of functionalized graphene FETs are presented.

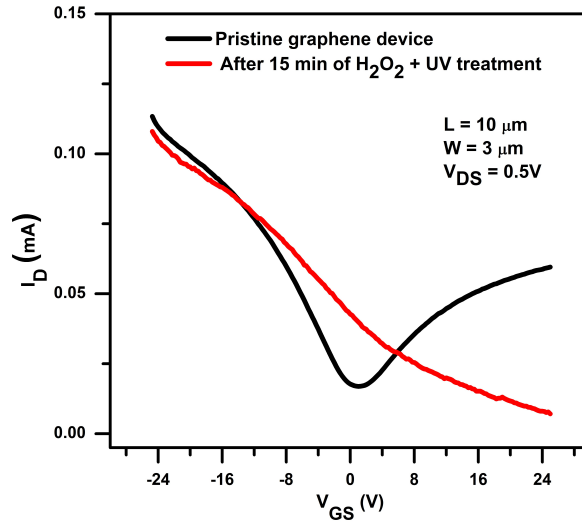


Figure 4.10: Transfer characteristics of CVD GFETs before and after hydroxylation when measured in air.

Figure 4.10 shows the transfer characteristics of back-gated CVD graphene FETs before and after hydroxylation. Current - Voltage characteristics of pristine graphene FETs were measured in air at room temperature. Subsequently these devices were treated with H_2O_2 for 15 minutes in the presence of UV light and I-V was measured again in air at room temperature. Minimum conductivity (σ_{min}) decreases after hydroxylation and this decrease in σ_{min} can be understood by carrier density dependent expression of conductivity $\sigma(n)$, equation (4.1), which is theoretically predicted by many authors [134, 135].

$$\sigma(n) = Ce \left| \frac{n}{n_{imp}} \right| + \sigma_{res} \quad (4.1)$$

Where C is a constant, e is the electronic charge, n is carrier density, n_{imp} is the charged impurity density and σ_{res} is the residual conductivity at $n = 0$. The decrease in σ_{min} can be attributed to the increase in n_{imp} after hydroxylation. Dirac point voltage or gate voltage of minimum conductivity, V_{Dirac} , shifts towards more positive gate voltage, from -2 V for pristine graphene to beyond 25 V for hydroxylated graphene, which indicates p-type doping.

Width of I-V characteristics around Dirac point (ΔV_{Dirac}) broadens after treatment

due to increase in n_{imp} after hydroxylation. Equation (4.2) shows the ΔV_{Dirac} dependency on n_{imp} [134].

$$\Delta V_{Dirac} \propto n_{imp} \quad (4.2)$$

Hole mobility values reduces from $3830 \text{ cm}^2 \text{ V}^{-1} \text{ s}^{-1}$ to $1100 \text{ cm}^2 \text{ V}^{-1} \text{ s}^{-1}$ after hydroxylation. This loss in the carrier mobility values is mainly due to the increase in the scattering of carriers with the charged impurities, equation (4.3) [134].

$$\frac{1}{\mu} \propto n_{imp} \quad (4.3)$$

The mobility values for -OH functionalized graphene FETs we have obtained are 100 times higher compared to the best reported mobilities for RGO [30]. We calculated mobility by Fitting Method (FTM) method [136] by fitting the R vs V_G curve, as obtained in appendix C.

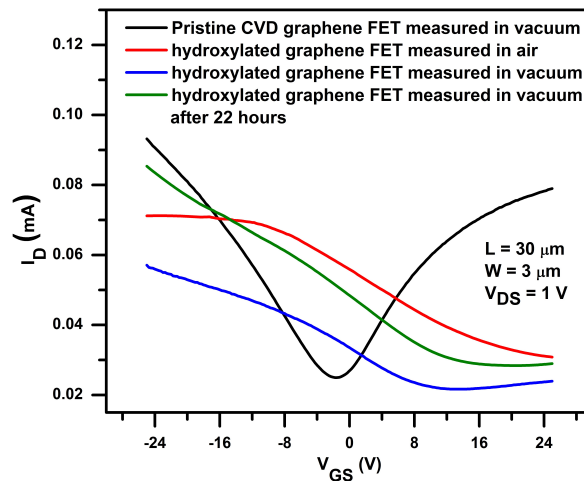


Figure 4.11: Transfer characteristics of CVD GFETs before and after hydroxylation when measured in vacuum.

To check the vacuum stability of -OH functional groups, a different set of devices were measured in vacuum. First, GFETs were fabricated using pristine CVD graphene

and I-V characteristics measured in vacuum of 5×10^{-3} mbar. Then the devices were functionalized with H_2O_2 in the presence of UV light and measured in air. The devices were then loaded into the vacuum chamber and I-V characteristics were measured immediately after reaching the vacuum level of 5×10^{-3} mbar. Then these devices were kept in vacuum chamber for 22 hours and measured again to check the stability of hydroxyl groups attached to graphene. The results are shown in figure 4.11 for one of the GFETs. Hole mobility (μ_p) values for pristine GFET is $1823 \text{ cm}^2 \text{ V}^{-1} \text{ s}^{-1}$, and for hydroxylated graphene GFET it is 700, 800 and $690 \text{ cm}^2 \text{ V}^{-1} \text{ s}^{-1}$ when measured in air, 5×10^{-3} mbar vacuum and after keeping in vacuum for 22 hours respectively. Even after keeping in vacuum for 22 hours no further shift in Dirac point towards pristine graphene is seen for hydroxylated graphene FET. By comparing the I - V characteristics measured in vacuum, the functionalization is seen to be vacuum stable. It may be noted that the XPS measurements were also carried out at high vacuum and hence the data presented in figure 3.10 is representative of the hydroxylated graphene for which I-V curves are measured in vacuum, figure 4.11.

After hydroxylation, the Dirac point voltage measured in vacuum is much smaller than that measured in air. It can be concluded that some adsorbed species on the hydroxylated graphene are desorbed in vacuum. These desorbed species could be either oxygen and water molecules which sits on graphene surface from air or -OH groups which were adsorbed on graphene surface after hydroxylation. But vacuum measurement after 22 hours shows that hydroxyl groups are stable and are not desorbed from graphene surface in vacuum. This shows that shift in Dirac point for hydroxylated graphene towards negative voltage when measured from air to vacuum is likely due to desorption of environmental oxygen and water molecules from graphene surface [137, 138] and not due to desorption of hydroxyl groups.

Hydroxyl adsorbates are affecting the conductivity in vacuum also, as shown in figure 4.11. Stability of hydroxyl functional groups in vacuum is tested by vacuum measurements. To check the thermal stability of hydroxyl groups at higher temperature, the XPS spectra of hydroxyl functionalized graphene was taken after annealing in vacuum

of 4×10^{-2} mbar at 150°C for 30 minutes and it was compared with XPS spectra of hydroxyl functionalized graphene before annealing. No change in the XPS spectra after annealing is observed which implies that hydroxyl groups are stable at high temperature as well. C 1s XPS spectra of hydroxyl functionalized graphene, before and after annealing is shown in figure 4.12.

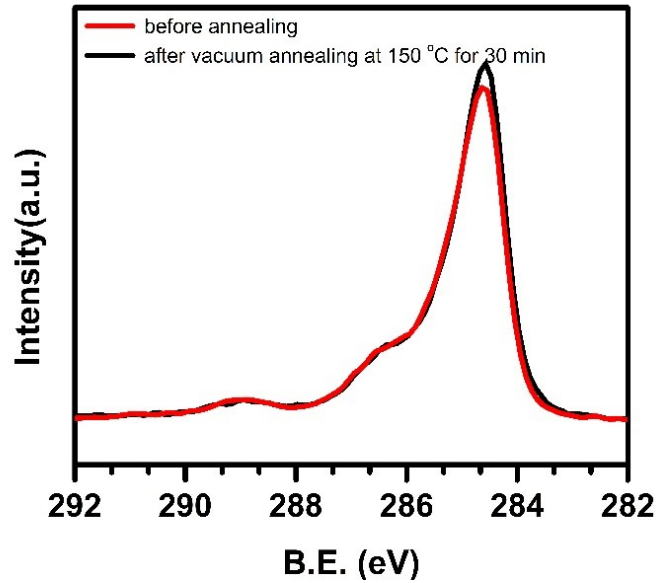


Figure 4.12: C 1s XPS spectra of hydroxyl functionalized CVD graphene before and after vacuum annealing at 150°C for 30 minutes.

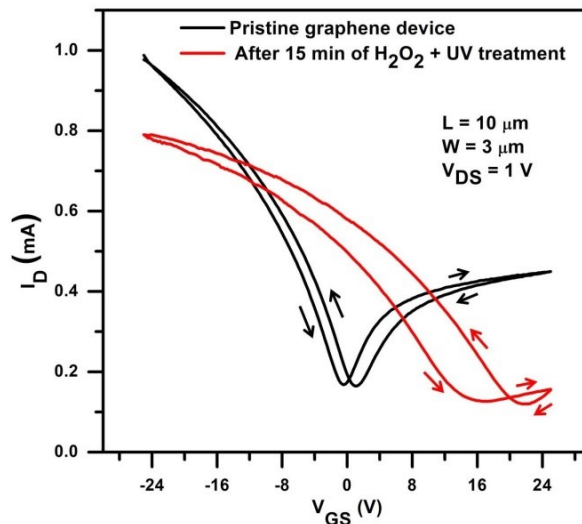


Figure 4.13: Hysteresis of gate response for pristine and hydroxyl functionalized graphene FETs.

Hysteresis of gate response for pristine graphene and hydroxyl functionalized graphene is shown in figure 4.13. Sweeping voltage rate, voltage range and surrounding environment during measurement were kept same for both measurements. The shift in V_{Dirac} for cyclic sweeping of gate voltage has been considered as the hysteresis for graphene FET. Hysteresis increases from 1.5 V for pristine graphene FET to 5 V for hydroxyl functionalized graphene FET. Hydroxyl functionalization increases hole density in the graphene. Consequently, V_{Dirac} shifts more towards right during sweeping gate voltage backward.

Figure 4.14 shows I-V measurement of a functionalized graphene device measured in different conditions. First the device was measured in air at room temperature, at low temperature of 6 K, then at room temperature in vacuum, and subsequently in air at room temperature after unloading from vacuum. The device performance improved in vacuum both at low and room temperature. For device shown in figure 4.14, the hole mobility (μ_p) value increased to $1407 \text{ cm}^2 \text{ V}^{-1} \text{ s}^{-1}$ at low temperature and $1013 \text{ cm}^2 \text{ V}^{-1} \text{ s}^{-1}$ at room temperature whereas it was $755 \text{ cm}^2 \text{ V}^{-1} \text{ s}^{-1}$ when measured in air before loading into the low temperature measurement system. We were able to calculate electron mobility (μ_n) also only in case of low temperature and vacuum room temperature measurement because Dirac point was not visible in the applied voltage range for measurements done in air.

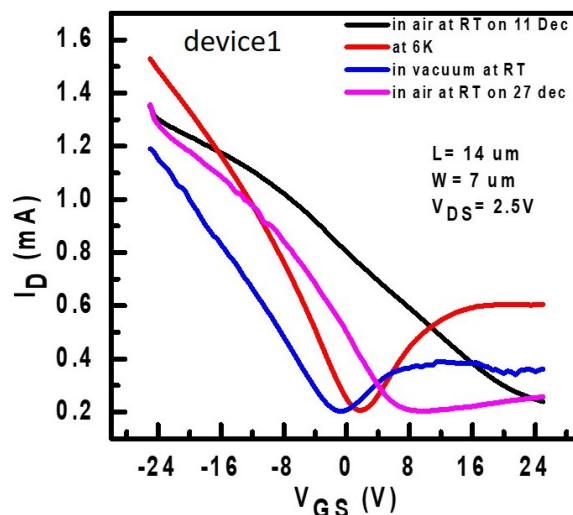


Figure 4.14: Transfer characteristics of functionalized graphene FETs in different conditions

The Dirac point position for measurement done in air and vacuum is expected [137] to be at different positions. But shift in Dirac point with change in temperature is not expected for pristine graphene [139]. This shift in Dirac point position at low temperature and room temperature and improvement in mobility for low temperature needs to be examined further.

4.4 Improvement of Contact Resistance

4.4.1 Transfer Length Measurement (TLM)

It is reported in literature that if defects are created in the graphene at the metal-graphene overlap region, the contact resistance of graphene devices decreased [140, 141]. Bharadwaj et al. reported that by creating defects in graphene during graphene growth results in a factor of two reduction in contact resistivity for graphene devices when platinum, palladium or gold were used as contact metal [140]. Meersha et al. reported that by exposing graphene to (i) controlled O₂ or Ar plasma, (ii) O₂ or Ar ion bombardment, and (iii) electron beam just before the metal deposition creates sp²-hybridized/defected graphene which shows significant improvement in metal-graphene contact properties [141].

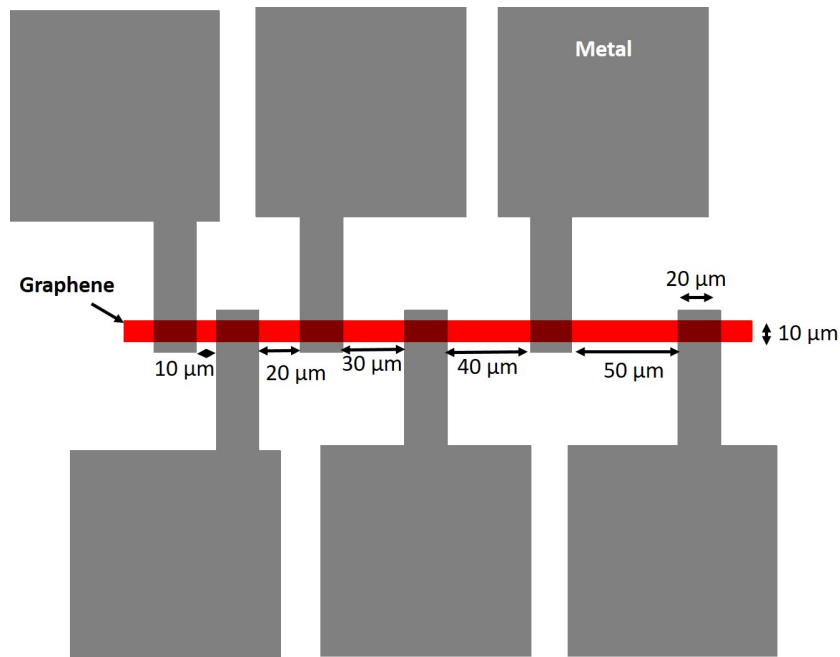


Figure 4.15: Schematic of TLM devices used for contact resistance measurements.

Our functionalization process also creates defects in graphene. We had designed a transfer length measurement structure shown in figure 4.15 and created defects in graphene via treatment of graphene with H_2O_2 in presence of UV light just before the metal deposition. During this process only graphene where metal will get deposit was exposed to H_2O_2 and defects were created only in that region of graphene and not in the channel region of graphene. Resistance for H_2O_2 treated (with defects) devices and pristine graphene (without defects) devices are compared.

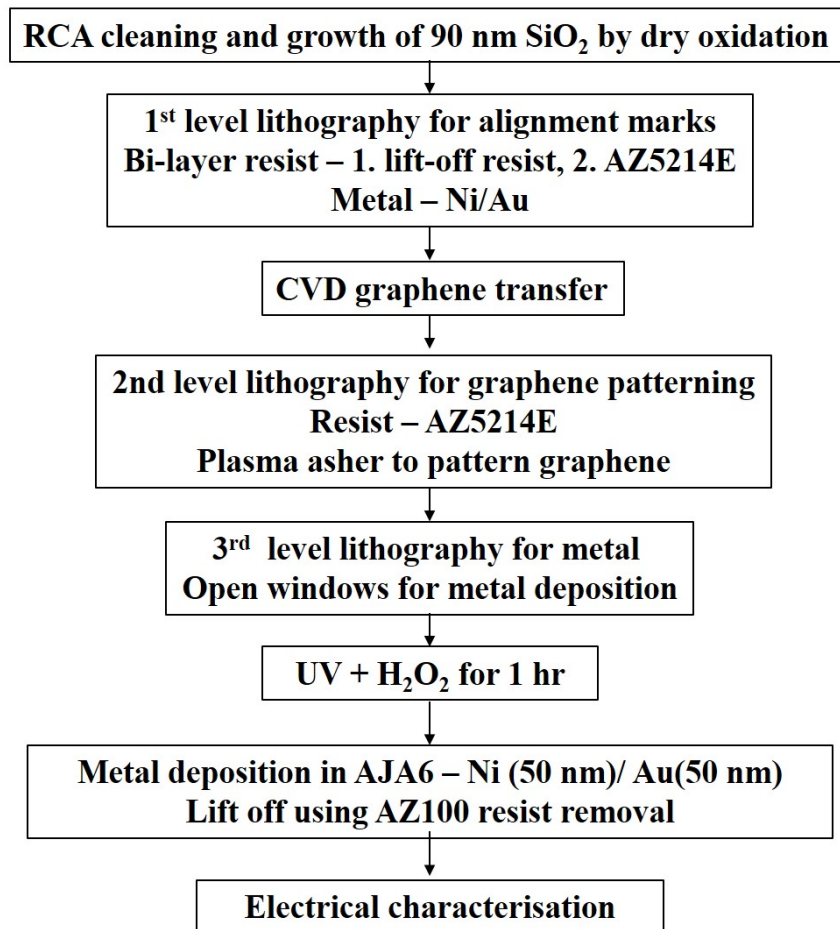


Figure 4.16: Process flow for TLM device fabrication.

Process flow for device fabrication is shown in figure 4.16 and an optical image of the fabricated TLM devices is shown in figure 4.17. After opening the windows in photoresist for metal deposition on graphene, we treated the samples with H_2O_2 in the presence of UV light for one hour. In this process, graphene on which metal is going to be deposited got exposed to H_2O_2 whereas channel area of graphene was not exposed as it

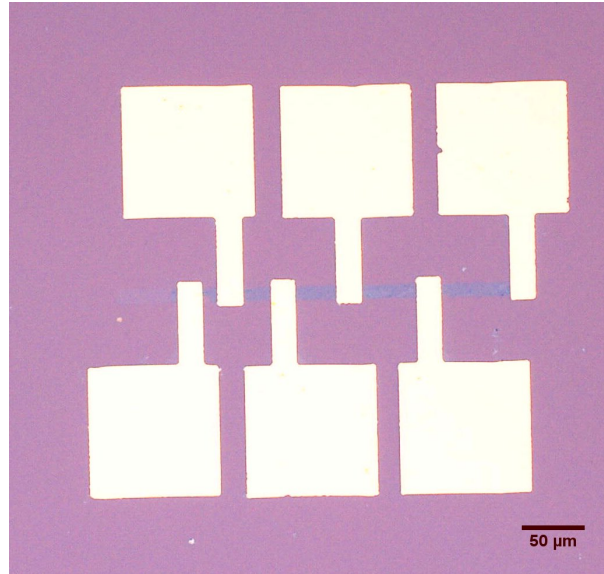


Figure 4.17: An optical image of as fabricated TLM devices.

was covered with photoresist. This process creates defects only in the exposed graphene after functionalization with $-OH$. Total resistance values for graphene devices of different channel length are shown in figure 4.18, values presented are the average values after measurement of three devices for each channel length. As per literature, a reduction in resistance was expected. However we observed a small increase in resistance after treatment. It is because defects created by our process are of sp^3 -hybridized type carbon atoms after converting from sp^2 -hybridized carbon atoms whereas literature reports talk about creating defects of sp -hybridized type carbon atoms.

	Channel length →	10 (μm)	20 (μm)	30 (μm)	40 (μm)	50 (μm)
Total Resistance (k Ω)	Without H_2O_2	2.27	5.5	4.87	5.67	6.82
	After 2 nd level UV + H_2O_2	2.56	5.42	5.2	6.03	15.9

Figure 4.18: Total resistance values for different channel length devices before and after H_2O_2 treatment.

Bharadwaj et al. introduced defects in CVD graphene synthesis and they measured a two fold decrease in the contact resistivity for defective graphene devices compared to

the non-defective graphene devices [140]. Meersha et al. used (i) O₂ and Ar plasma, (ii) O₂ and Ar ion bombardment, and (iii) electron beam to create the defects in the metal-graphene contact area of graphene. These techniques removed the carbon atoms from the graphene and result in sp-hybridized defects in graphene [141]. sp-hybridized defects in graphene increase the free electrons present on the graphene surface and increase the edge-type contact area of graphene with metal, whereas our work creates sp³-hybridized graphene which decrease the free electron density present on the graphene surface resulting in an increase in the total resistance.

4.4.2 Dependence on Metal-Graphene Overlap Length

In graphene devices with graphene as a channel and metal as source-drain, the edge region of metal-graphene overlap contribute 60% of total contact resistance whereas overlap region contribute 40% [141]. To check whether graphene-metal overlap region effect the contact resistance, special devices were designed with equal channel length but with different graphene-metal overlap lengths. Schematic of devices is shown in figure 4.19.

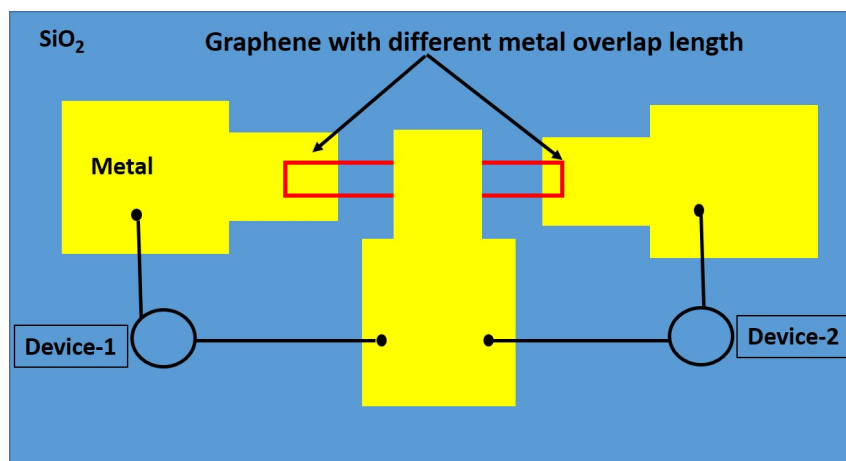


Figure 4.19: Schematic of device with different metal-graphene overlap length.

Total length of graphene-metal overlap was calculated by adding the graphene-metal overlap regions for both metal contacts. Plot of total resistance vs graphene-metal overlap length is shown in figure 4.21. No clear trend in resistance value with change in

overlap length can be observed. We found total resistance values scatter in a range of 1.5 to 3 k Ω for all devices with a graphene-metal overlap length in a range of 10 to 70 μm . It seems higher graphene-metal overlap doesn't effect the device resistance and it is limited by the graphene channel width and further increase in the graphene dimension has no effect on the resistance.

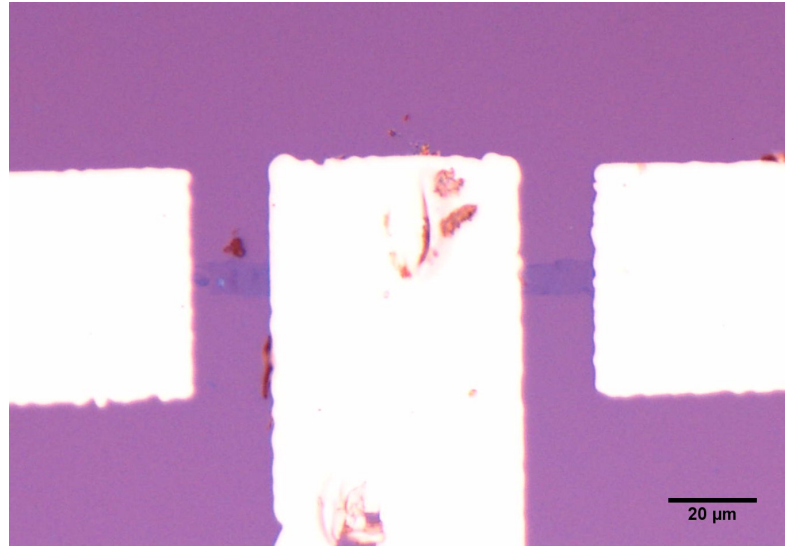


Figure 4.20: An optical photograph of device with different metal-graphene overlap lengths.

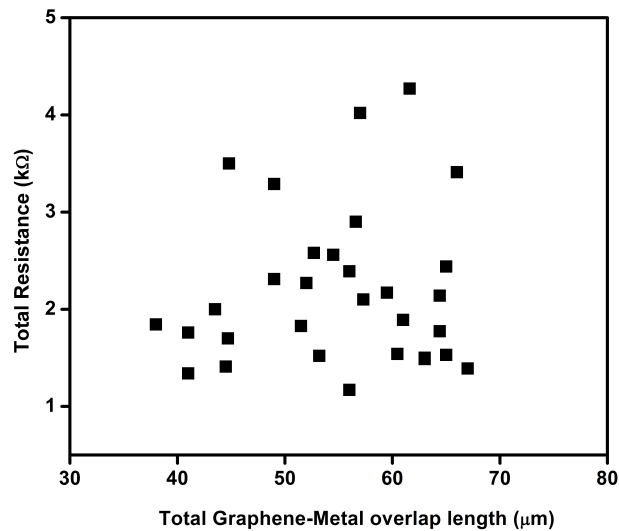


Figure 4.21: Total resistance vs metal-graphene overlap length.

4.5 Summary and Conclusions

In this chapter we have shown various electrical applications of functionalized graphene. Workfunction of pristine and functionalized graphene was calculated using KPFM and a decrease of 0.45 eV in workfunction after functionalization is observed. Deposition of Al₂O₃ on functionalized exfoliated graphene via ALD has been shown. More uniform deposition was observed on functionalized graphene compared to pristine graphene. High-K dielectric deposition via ALD can be used for fabrication of top-gated graphene transistors.

Fabrication and characterization of back-gated graphene field effect transistor has been explained in detail. Transfer characteristics of functionalized graphene FETs shows a shift in Dirac point voltage to higher value because of p-type doping after functionalization. Hole mobility values reduce from 3830 cm² V⁻¹ s⁻¹ to 1100 cm² V⁻¹ s⁻¹ after hydroxylation and these values are still much higher than the mobility values reported for GO and RGO. Hydroxyl functionalization is stable in vacuum and to show this graphene FETs were kept in vacuum for 22 hours. After 22 hours graphene FETs didn't show any sign of desorption of -OH groups in transfer characteristics. To check the thermal stability XPS spectra was recorded before and after annealing of functionalized graphene, which shows no change in C 1s XPS spectra after annealing.

Chapter 5

Ferromagnetism in Functionalized Graphene

To introduce magnetization in monolayer CVD graphene, it was doped with nitrogen. Nitrogen doping of CVD graphene was carried out via a two step process. Graphene was first functionalized with hydroxyl groups using a process already explained in section 3.2.2, and we obtained a high mobility -OH functionalized monolayer CVD graphene after this process. Hydroxyl functionalized graphene was subsequently annealed in ammonia gas for 1 hour for nitrogen doping. Ferromagnetism and AMR are demonstrated in monolayer CVD graphene doped with nitrogen. Hydroxyl functionalized graphene is bio-compatible [40, 41]. We purposed that, after making it magnetic, it may be used in nano-medicines for magnetic field guided drug delivery (not explored in this thesis). Magnetic CVD graphene has advantages over magnetic GO and RGO in terms of purity and thin film device fabrication as it is difficult to obtain single layer and large area continuous films of GO and RGO [3].

5.1 Nitrogen Doping of Graphene

Monolayer CVD graphene was transferred onto SiO₂/Si from Cu foil, by using the process described in section 3.1.1. CVD graphene on SiO₂/Si was subsequently functionalized with -OH groups by treating with H₂O₂ in the presence of UV light for 30 minutes. We had demonstrated the process for functionalization of graphene with -OH in section

3.2.2. The hydroxyl functionalized graphene was subsequently annealed in ammonia gas at 500°C for one hour at atmospheric pressure to synthesize nitrogen doped graphene (NGr). XPS and Raman spectroscopy were carried out to characterize the nitrogen doping after ammonia annealing.

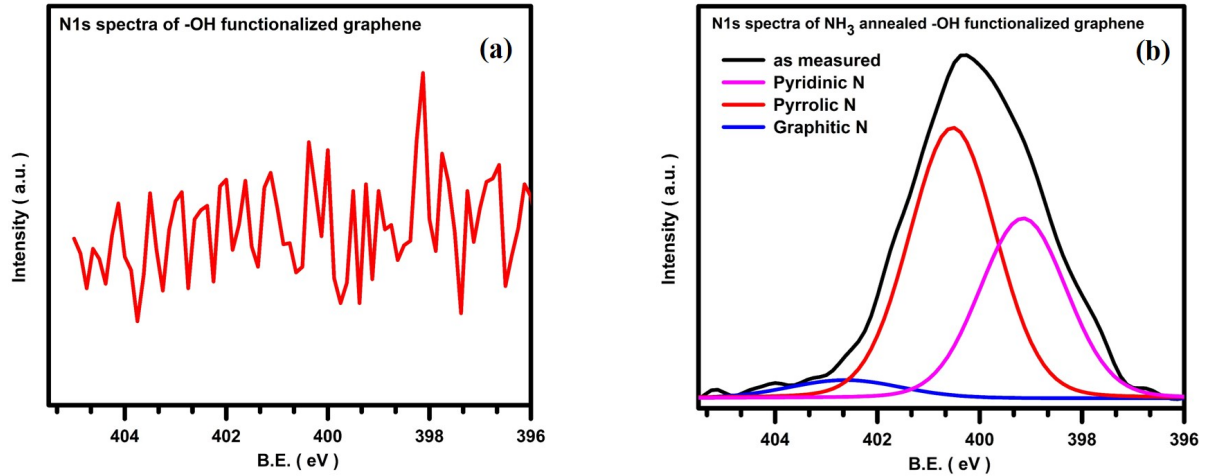


Figure 5.1: N 1s XPS spectra of (a) Only -OH functionalized graphene, no signature of nitrogen, and (b) Graphene after two step process of hydroxylation and ammonia annealing, confirm presence of nitrogen, the measured spectrum was deconvoluted into three peaks.

The N 1s XPS spectra of CVD graphene after only hydroxylation and after hydroxylation followed by ammonia annealing are shown in figure 5.1 (a) and (b) respectively. N 1s XPS spectra for only -OH functionalized graphene doesn't show any signature of nitrogen. Whereas for NGr, the N 1s spectra clearly shows presence of nitrogen peak. N 1s spectra for NGr is deconvoluted into three peaks related to pyridinic N, pyrrolic N and graphitic N at 399.1 eV, 400.5 eV and 402.6 eV respectively [142], and have relative band areas of 37.97 %, 57.07 % and 4.95 % respectively. The presence of nitrogen in CVD graphene after -OH functionalization and NH_3 annealing, indicated by the XPS analysis, shows that the CVD graphene become N doped after two step process of H_2O_2 treatment and ammonia annealing. Raman spectra for pristine, only -OH functionalized and nitrogen doped graphene is shown in figure 5.2. Raman spectra shows increase in I_D/I_G ratio from 0.04 to 0.3 for -OH functionalized graphene and to 0.6 after annealing in NH_3 , shown in table 5.1. This increase in defect peak intensity clearly indicate doping of

graphene. The possibility that hydroxyl groups leave the graphene after annealing at high temperature, leading to higher density of defects, is ruled out by XPS analysis presented in figure 5.1.

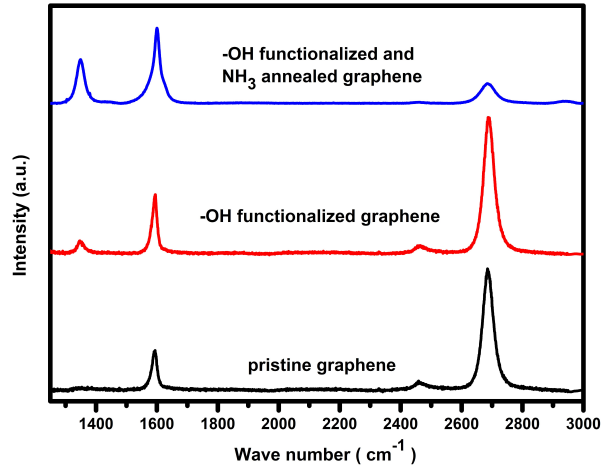


Figure 5.2: Raman spectra of pristine CVD graphene (black), and after hydroxylation (red) and after nitrogen doping via ammonia annealing after -OH functionalization (blue).

Table 5.1: I_D/I_G values for pristine, only -OH functionalized, and nitrogen doped graphene.

	Pristine graphene	-OH graphene	Nitrogen doped graphene
I_D/I_G	0.04	0.3	0.6

5.2 Magnetization Measurement

5.2.1 Superconducting Quantum Interference Device (SQUID) Magnetometer

M-H Curves

SQUID was used to measure the magnetization in pristine graphene, -OH functionalized graphene and nitrogen doped graphene. Single layer pristine CVD graphene on SiO₂ shows diamagnetic M-H curve, see figure 5.3. This is similar to the results published by Sepioni et al. for mechanically exfoliated pristine graphene [4]. M-H curves measured

at different temperatures for only hydroxyl functionalized graphene is shown in figure 5.4. Only -OH functionalized graphene shows very weak ferromagnetism only at 2 K.

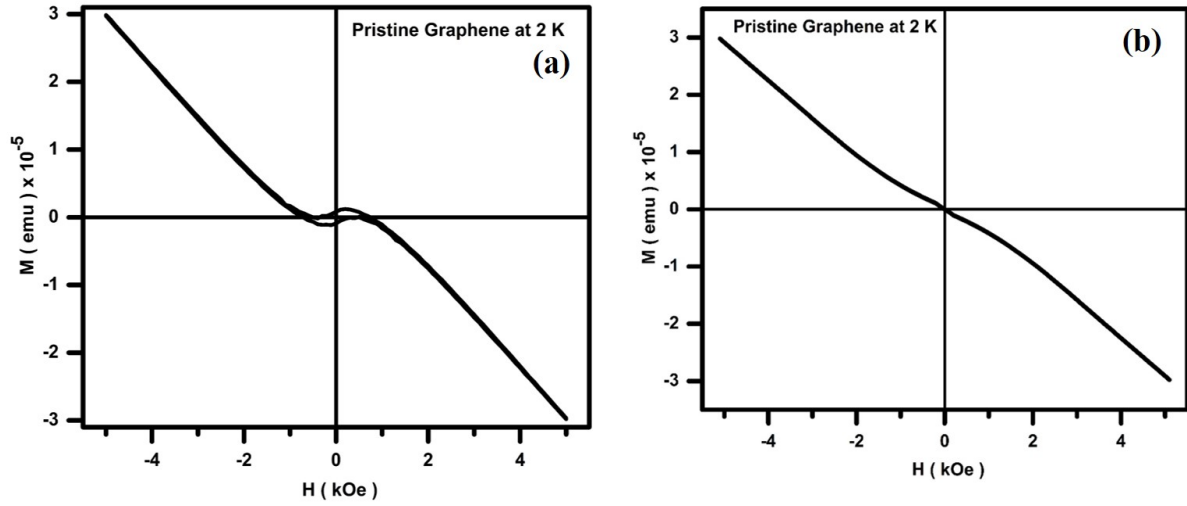


Figure 5.3: Magnetization as a function of magnetic field at 2 K for pristine graphene shows diamagnetic behavior, (a) as measured (b) after background subtraction.

Ferromagnetism is lost beyond 2 K, and a paramagnetic behavior can be noticed and the magnetization is lost beyond 10 K. In contrast, the ferromagnetism and magnetism in nitrogen doped graphene are active to higher temperatures.

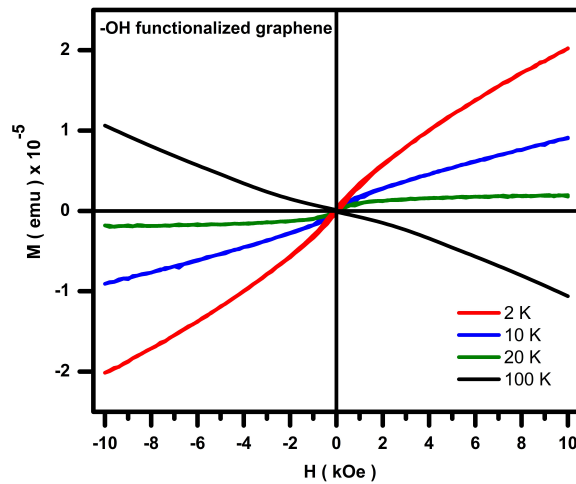


Figure 5.4: M-H curve for hydroxyl functionalized graphene.

Figure 5.5 (a) shows M-H curve for NGr measured at different temperatures from 2 K to 300 K in the magnetic field range of -10 kOe to +10 kOe. Results shown in figure 5.4

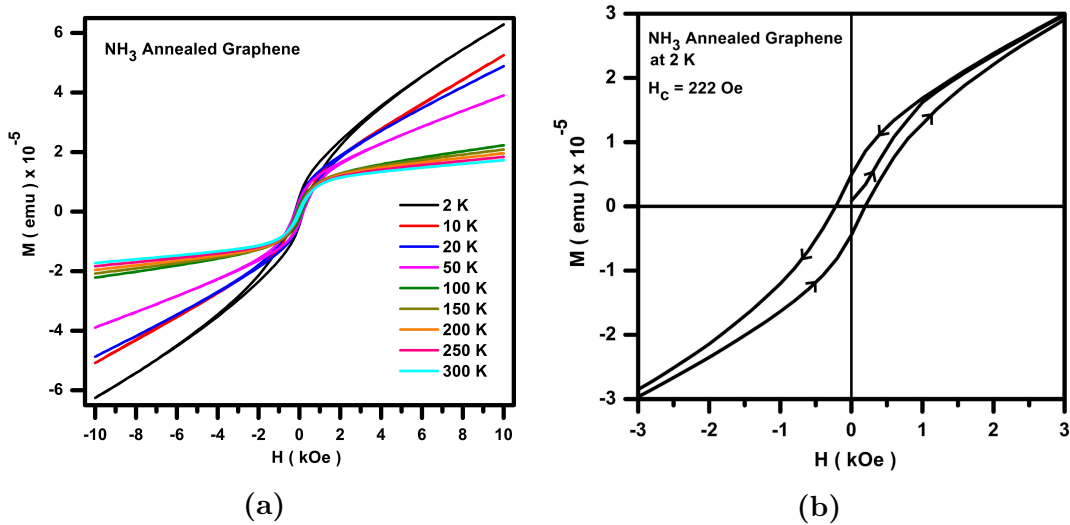


Figure 5.5: (a) Magnetic moment as a function of magnetic field for different temperatures from 2 K to 300 K for N doped graphene. (b) Magnified image for lower magnetic field values at 2 K.

and 5.5 are after subtracting the background of Si/SiO₂ substrate and substrate holder made of quartz. Ferromagnetism in NGr can be clearly noticed from the hysteresis loop in M-H curves.

Figure 5.5 (b) shows a zoomed-in version of the M-H curve at 2 K, and clearly shows a strong ferromagnetism hysteresis loop. For temperatures of 2 K, 10 K, 20 K and 50 K the magnetic moment was not saturated till 10 kOe of magnetic field and for temperature range from 100 K to 300 K the magnetic moment almost saturate at 2 kOe. As shown in figure 5.5 (b) the intrinsic coercivity (H_c) is 222 Oe at 2 K. Magnetization values reported in figure 5.5 are comparable with the magnetization values of hydrogenated epitaxial graphene reported by Lanfei et al. [9].

SQUID measurement shows very high values of magnetic moment for the graphene samples. Conversion of measured magnetization values from emu to emu/g is shown below. Magnetization values in emu/g is even 20 times higher than a pure ferromagnetic iron. Such high values cannot be observed from only graphene. We assume that high values were observed because some background got added to the data during measurement and we were not able to remove the background. For pristine graphene also the values are in the same range but showing non-magnetic behavior, which means ferromagnetism

showed by NGr is not because of some background noise as we used graphene from same batch, same SiO₂/Si wafer, and quartz sample holder for measurements of all types of samples.

Conversion of measured magnetization values from emu to emu/g

Area of SQUID graphene sample = 3 mm × 3 mm = 9 × 10⁻⁶ m²

Mass density of graphene = 7.57 × 10⁻⁷ kg m⁻²

Mass of SQUID graphene sample = 6.8 ng

Measured value of magnetization for SQUID graphene sample = 3 × 10⁻⁵ emu

Convert magnetization into emu/g = 3 × 10⁻⁵ emu / 6.8 ng = 4400 emu/g

M-T curves

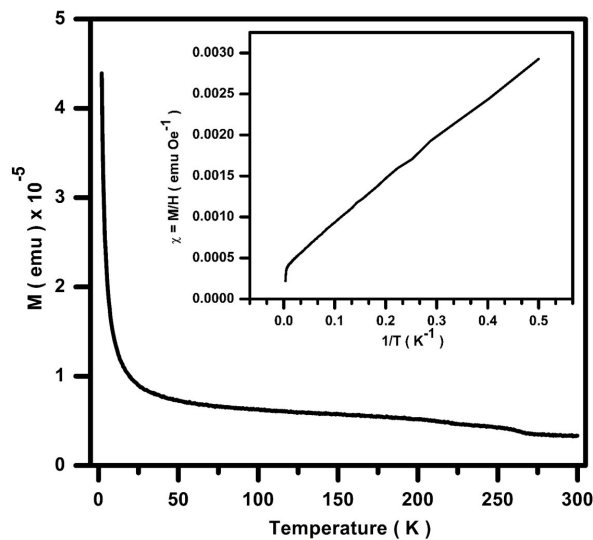


Figure 5.6: Magnetization as a function of temperature at a magnetic field of 1.5 kOe for nitrogen doped graphene.

Figure 5.6 shows M-T curves for NGr, which were measured in the presence of magnetic field of 1.5 kOe. With decrease in temperature, the magnetic moment increases and there is a drastic increase in magnetic moment for temperature below 25 K. Inset of figure 5.6 shows $\chi = M/H$ vs $1/T$ curve and it shows a paramagnetic behavior. This M-T curve is similar to those Qin et al. reported for RGO and N doped RGO [90]. It can be concluded from M-H and M-T curves that paramagnetism (due to -OH, figure 5.4) and

ferromagnetism (due to N atoms and defects, figure 5.5 and 5.6) coexist in NGr.

5.2.2 Magnetic Force Microscopy (MFM)

Magnetic force microscopy scan plots for pristine graphene, -OH functionalized graphene and nitrogen doped graphene are shown in figure 5.7, 5.8 and 5.9 respectively. In MFM, a magnetic tip was used to scan the samples and the frequency of tip vibration changed whenever it experiences a magnetic force due to interaction between the magnetic field of the tip and sample. Tip height from the sample was kept constant at 30 nm so that the tip don't experience any force due to the topography of the sample surface. By using MFM one can investigate the change in frequency and phase of magnetic tip vibration due to the magnetic samples. To prepare the samples for MFM the CVD graphene was first transferred onto the SiO₂/Si substrate followed by patterning into strips with a width of 5 and 7 μm using photolithography and subsequently -OH functionalization and nitrogen doping was carried out as describe in section 5.1. Graphene was patterned into strips so that the difference between non-magnetic SiO₂ and magnetic graphene layer can be identify easily using MFM scans.

In case of pristine graphene the change in MFM image of graphene with respect to SiO₂ can be noticed only at the boundaries of the graphene strips, a clear dip can be seen only at the boundaries in figure 5.7 (c) and (d). Only -OH functionalized graphene also shows similar results to pristine graphene, shown in figure 5.8. Whereas in case of nitrogen doped graphene, a clear change in MFM for whole graphene strip with respect to the SiO₂ is visible, as shown in figure 5.9 (b), (c) and (d). Thus, MFM also confirm presence of magnetism in NGr.

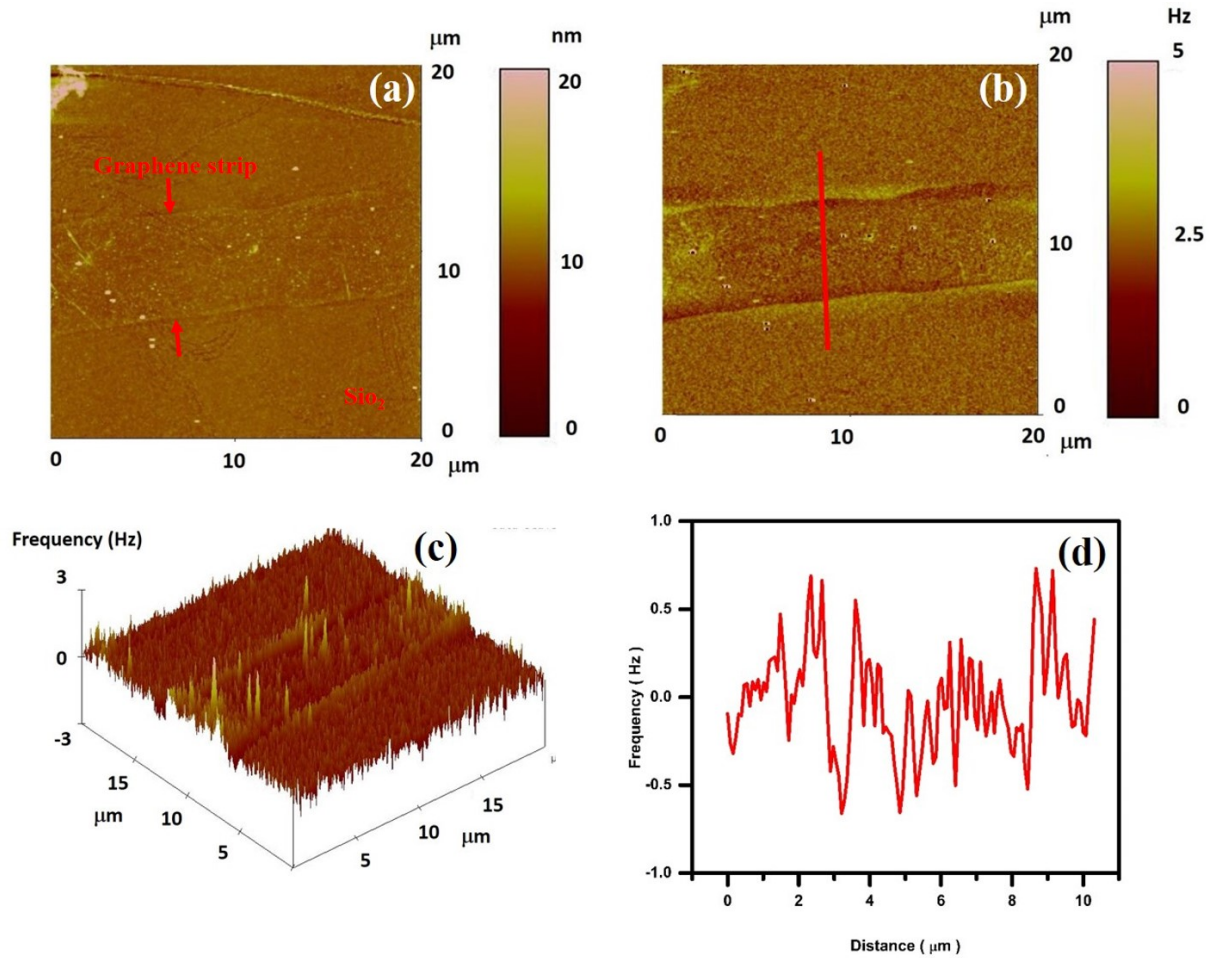
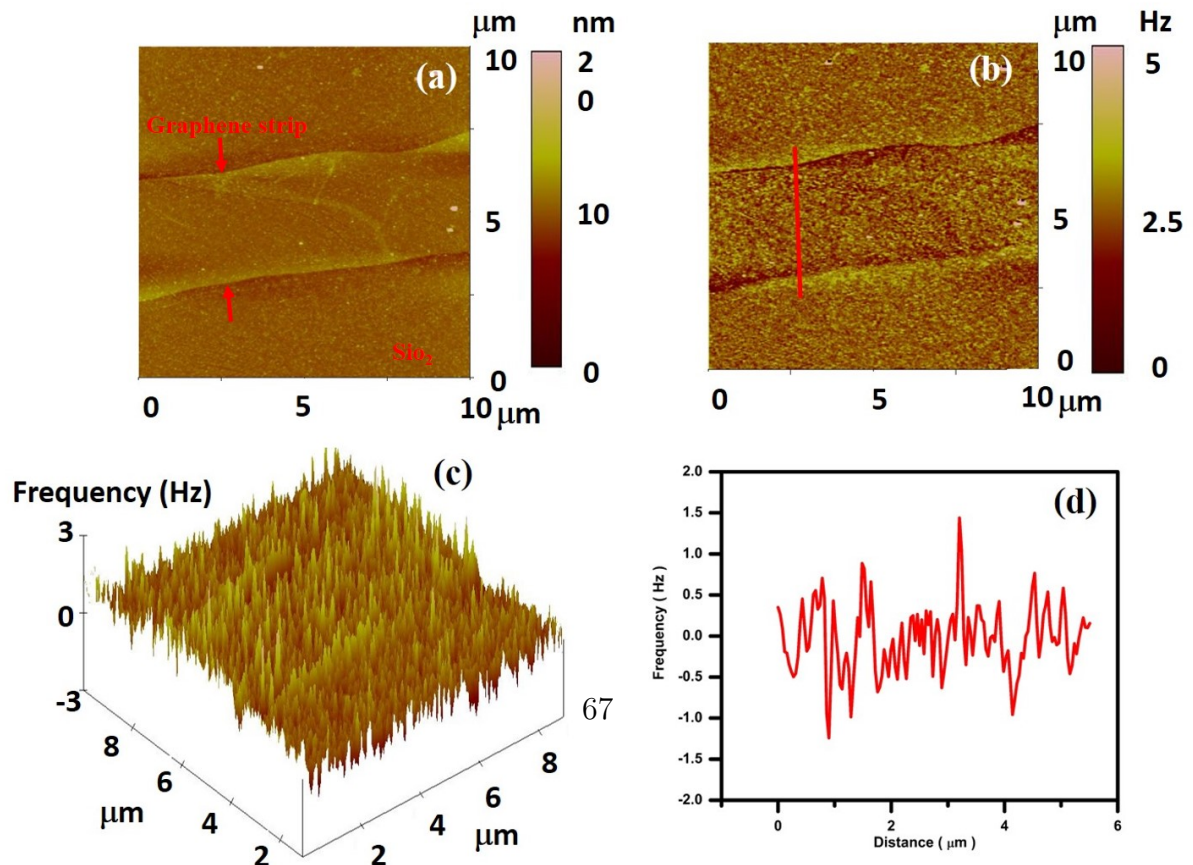


Figure 5.7: (a) Topography AFM image (b) 2D MFM image (c) 3D MFM image (d) line section of 2D MFM scan for pristine graphene.



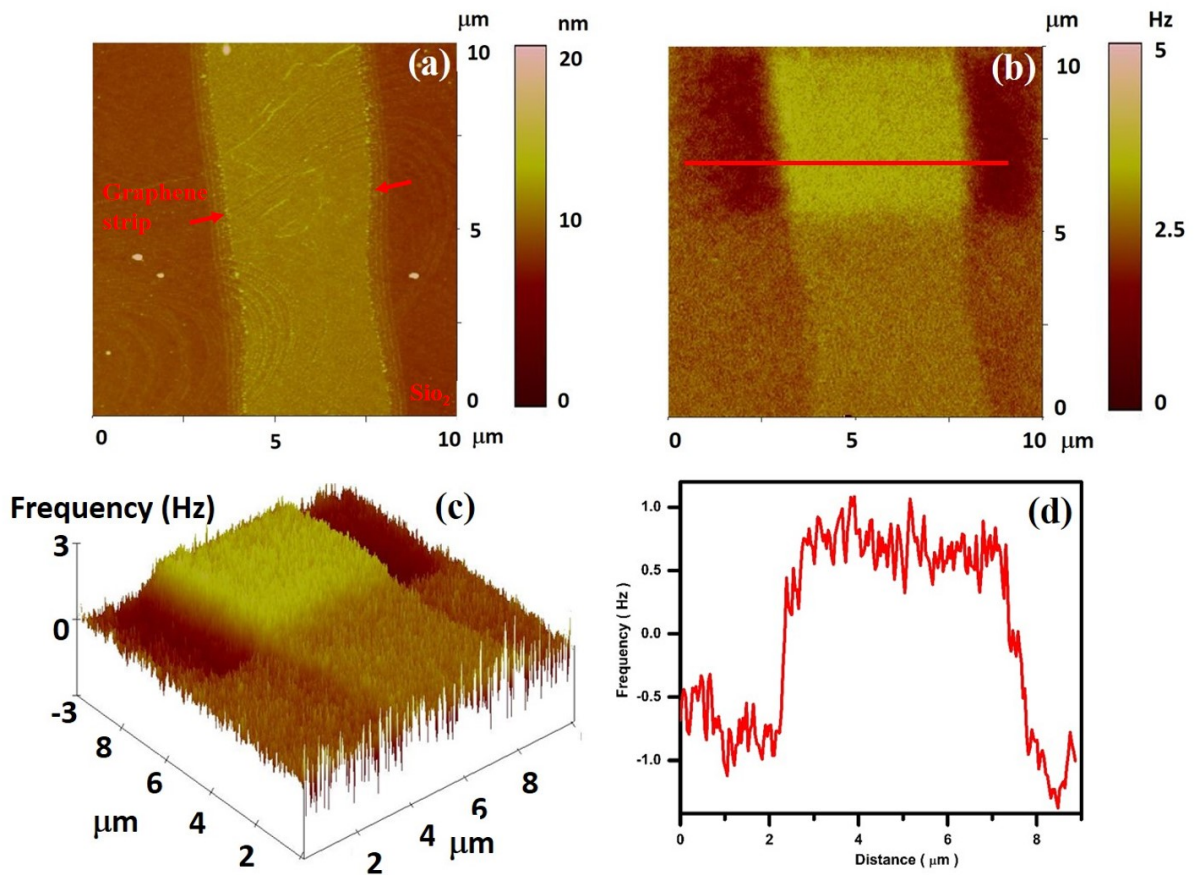


Figure 5.9: (a) Topography AFM image (b) 2D MFM image (c) 3D MFM image (d) line section of 2D MFM scan for nitrogen doped graphene.

5.2.3 Electron Spin Resonance (ESR)

Electron spin resonance spectra for nitrogen doped and pristine graphene is shown in figure 5.10. ESR will show resonance in a material only if free electrons are available in that material. ESR shows a clear resonance in nitrogen doped graphene, figure 5.10 (a). No resonance was observed in only -OH functionalized graphene and pristine graphene, shown in figure 5.10 (b) and (c) respectively. This ESR study confirmed availability of free electrons after nitrogen doping of graphene.

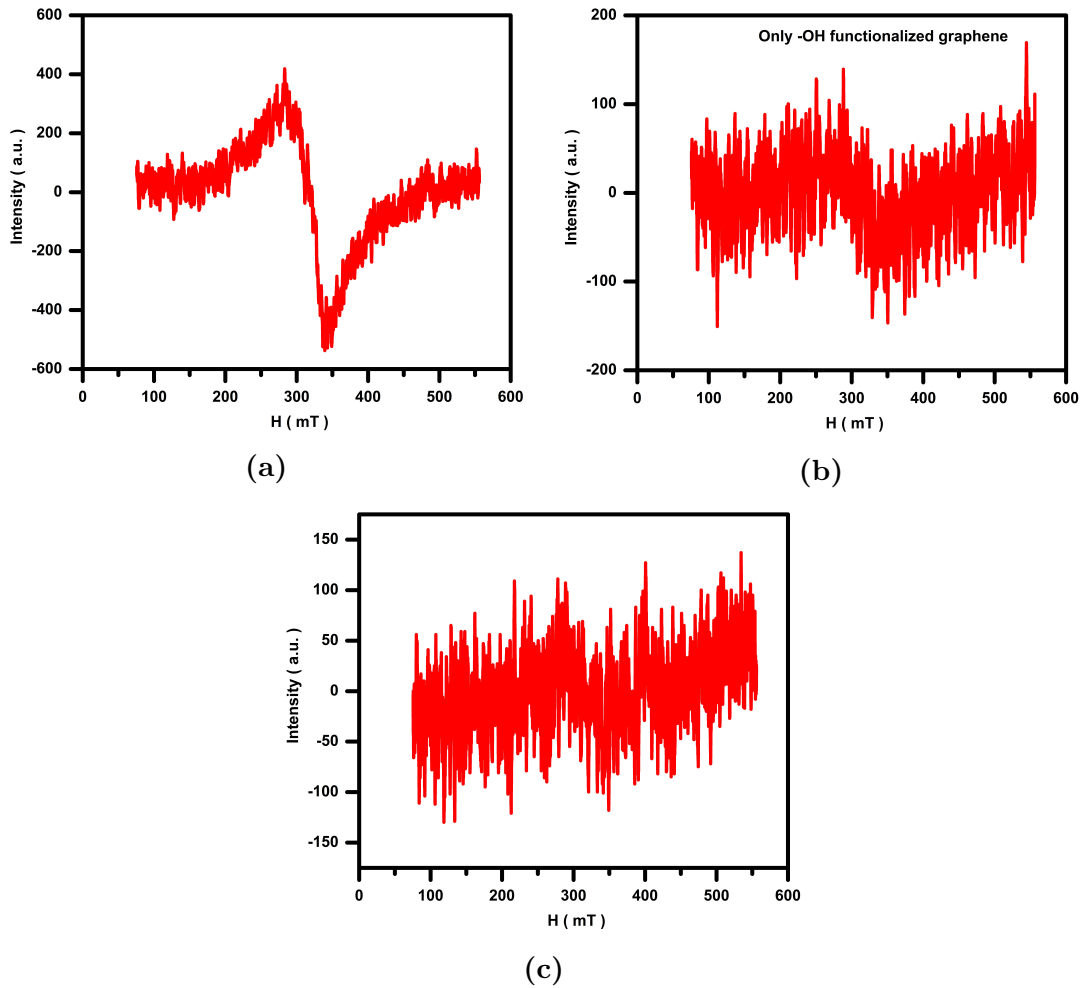


Figure 5.10: ESR spectra for (a) nitrogen doped graphene, shows good resonance curve, (b) for only -OH functionalized graphene (c) for pristine graphene, no resonance can be seen in (b) and (c).

5.3 Anisotropic Magnetoresistance (AMR)

Intrinsic ferromagnetism in NGr was further tested by measuring angular dependency of AMR effect in NGr. Graphene devices for AMR measurement were fabricated by photo-lithography. Transferred CVD graphene on SiO_2 was first patterned into strips of length $50 \mu\text{m}$ and width $20 \mu\text{m}$. Devices were treated with H_2O_2 for -OH functionalization followed by annealing in NH_3 at 500°C for 1 hour to dope it with nitrogen. Subsequently metal contacts of Ti/Au ($20 \text{ nm}/30 \text{ nm}$) were fabricated using e-beam evaporation and lift-off processes. A schematic of the fabricated AMR device is shown in figure 5.11.

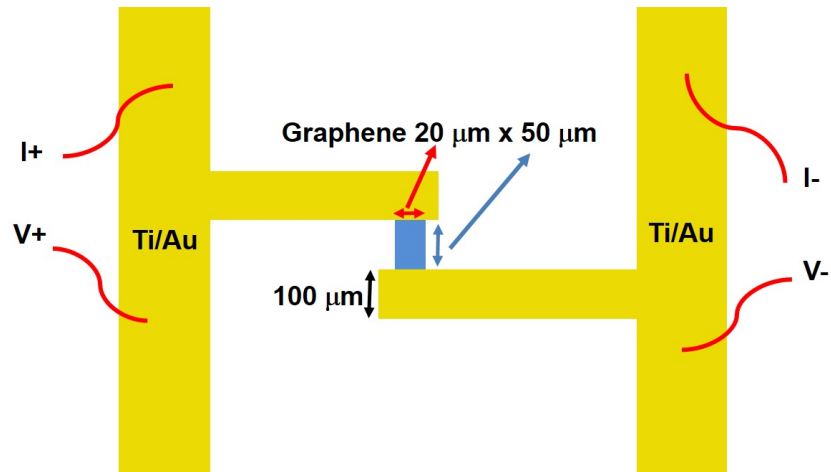


Figure 5.11: Schematic of devices fabricated for angular AMR measurements (dimensions are not upto the scale).

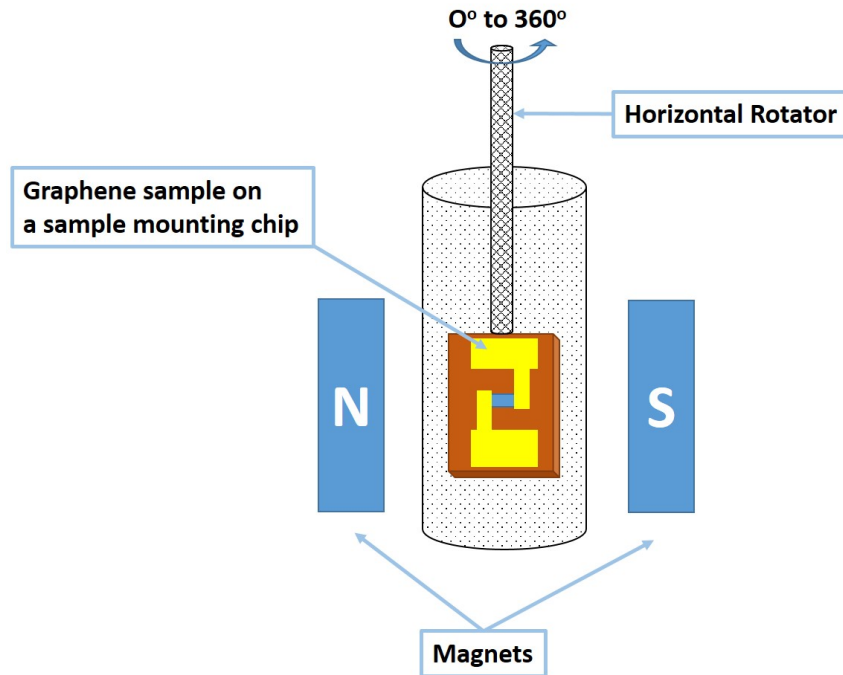


Figure 5.12: Schematic of devices inside the PPMS tool shows in-plane magnetic field at an angle of 0° with respect to the graphene.

In AMR phenomena, the resistivity of a device depends upon the angle between current flow and the magnetization of the device. Using PPMS tool, four terminal I-V measurements were carried out and the resistivity was measured when angle of in-plane magnetic field was varied with respect to current direction in the graphene. Here, when

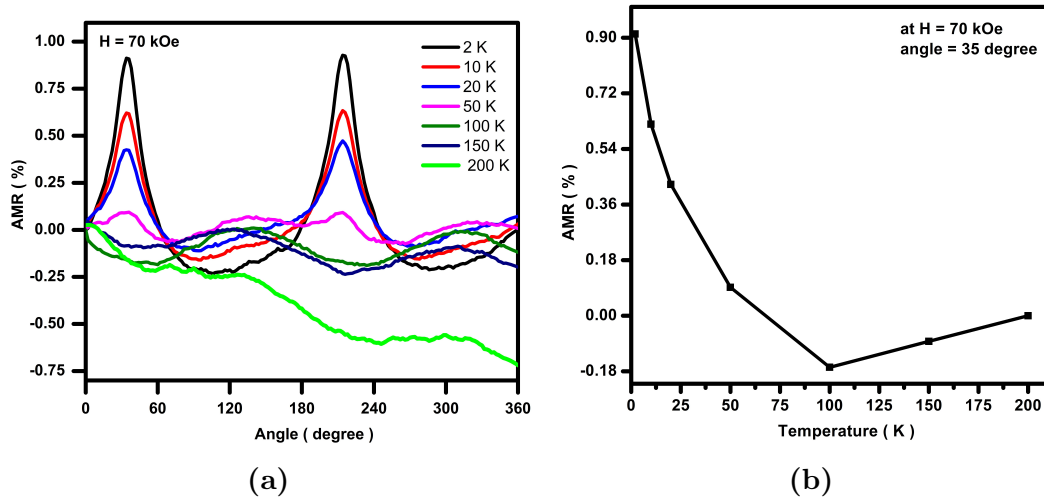


Figure 5.13: (a) AMR as a function of angle of applied magnetic field (70 kOe) at different temperatures from 2 K to 200 K, beyond 150K devices didn't show any AMR. (b) Maximum AMR value as a function of temperature at constant magnetic field of 70 kOe and angle of 35°.

we change the angle of applied magnetic field, the magnetization of graphene align itself accordingly and the angle between current and magnetization changes with a change of orientation of applied magnetic field, which results in the change of resistivity. Figure 5.12 shows a schematic of graphene device mounted on a chip and horizontal rotator. This whole assembly was then placed between the magnets inside the PPMS tool. In figure 5.12 magnetic field is in-plane with respect to the current in graphene and at an angle of zero degree. Horizontal rotator shown in figure can be rotated with the help of the motor to change the angle between graphene and magnetic field from 0° to 360°. Chamber was cooled down to 2 K and an in-plane magnetic field of 70 kOe was applied. Now resistance of device was measured by varying the angle of magnetic field from 0° to 360° with the help of horizontal rotator while keeping the field and temperature constant. The same was repeated for temperatures 10 K, 20 K, 50 K, 100 K, 150 K, 200 K, 250 K and 300 K. Angular dependency of AMR at constant in-plane field of 70 kOe at different temperatures is shown in figure 5.13 (a). Data till 200 K is shown because devices didn't show AMR beyond 150 K. Figure 5.13 (b) shows maximum AMR measured for different temperatures at in-plane field of 70 kOe. NGr shows maximum AMR of 0.92 % at a temperature of 2 K. AMR decreases with an increase in temperature and reverses its direction from positive

AMR to negative AMR after 50 K, and stop responding to angular change in field at 200 K and higher temperatures. Maxima of AMR occurred at an angle of 35° and minima at 125° .

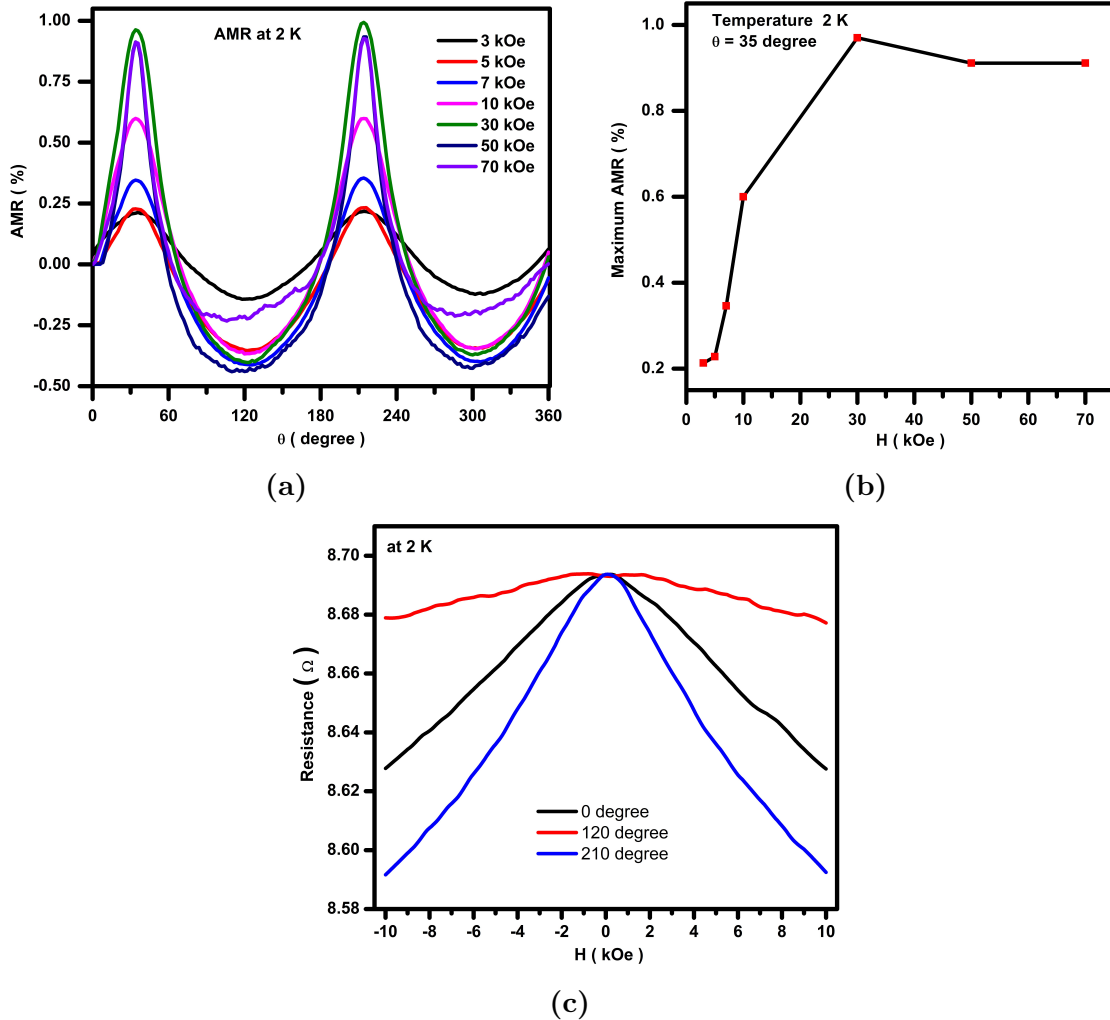


Figure 5.14: (a) AMR measured at 2 K for in-plane magnetic field in the range from 3 kOe to 70 kOe. (b) Maxima AMR value at 35° as function of in-plane magnetic field at 2 K. (c) Resistance as a function of magnetic field at 2 K for 0° , 120° and 210° .

Angular dependency of AMR for different in-plane magnetic field strength at 2K is shown in figure 5.14 (a), and figure 5.14 (b) shows maximum AMR measured vs magnetic field strength when magnetic field was applied in-plane at a fix angle of 35° . Initially the AMR increases with increase in magnetic field strength from 3 kOe to 30 kOe, and after 30 kOe it starts decreasing with increase of field strength, as shown in figure 5.14 (a) and 5.14 (b). NGr shows the maximum AMR at 30 kOe, and plateaus out at 50 kOe

and beyond. Figure 5.14 (c) shows resistance vs magnetic field at 2 K for different angles of applied in-plane magnetic field. At 0° , resistance decreases with increase in field and similar pattern is observed for 120° and 210° . However at 120° , the rate of decrease in resistance is lower, and at 210° , the rate of decrease in resistance is more as compared to 0° . This is because devices show a minima of AMR at 120° and a maxima at 210° .

5.4 Discussions

The experimental data presented so far strongly suggest that nitrogen doping and defects in NGr are the key reasons behind ferromagnetism seen in figure 5.5. Liu et al. have shown improvement in magnetization of RGO after nitrogen doping [7, 86]. Creation of defects or functionalization of graphene introduce free electrons due to break of delocalized π - π symmetry. Each free electron carry spin and overall contribution from each electron results in net magnetization in graphene. N doping increase the density of free electrons in the graphene and lifts-up the Fermi level [143]. Hydroxyl functionalization of graphene also break π - π bonds in the graphene lattice which create an imbalance in sublattice and results in un-bonded free electrons. Theoretical studies carried out by Ghaderi et al. predicted a magnetic moment of $0.75 \mu_B$ for each unpaired electron after -OH functionalization in graphene [45].

N 1s XPS spectra, figure 5.1 (b), shows the presence of more pyrrolic N than pyridinic N and graphitic N. Yafei et al. have shown theoretically that Pyrrolic N can induce a net magnetization of $0.95 \mu_B/N$ whereas graphitic N and pyridinic N has less influence on spin polarization [144]. Also nitrogen doping in the form of pyrrolic N, which is a 5 atoms ring structure, comes with defects like vacancy [89] and these defects can induce a magnetization of 1 to $1.7 \mu_B$, as shown experimentally by J. Zhu et al. [8] and theoretically by O. V. Yazyev et al. [81] and J. J. Chen et al. [145]. Interaction in between defects can increase the magnetization up to $2.9 \mu_B$ [8] and magnetic coupling between defects and pyrrolic N can cause the ferromagnetism in nitrogen doped CVD graphene as shown experimentally by Q. Miao et al. [88].

MFM characterization also confirms that nitrogen doped graphene is magnetic in nature. ESR study shows presence of free electrons in nitrogen doped graphene which confirms our hypothesis of availability of free electrons after doping as a reason for magnetization in graphene.

AMR in ferromagnetic metal arise due to scattering of d-orbital electrons in the direction of magnetization, where the orientation of magnetization is controlled by direction of applied magnetic field. AMR in ferromagnetic graphene may arise from the scattering of magnetic unpaired electrons but the reason behind such AMR response is still unclear.

5.5 Summary and Conclusions

In this chapter we have shown a method for nitrogen doping of monolayer CVD graphene via hydroxyl functionalization followed by ammonia annealing. Nitrogen doping introduced magnetization in graphene and the same was confirmed by SQUID, MFM, ESR and AMR measurements. N 1s XPS spectra shows presence of nitrogen in ammonia annealed -OH functionalized graphene. SQUID characterization shows ferromagnetic loop in nitrogen doping graphene and pristine graphene shows diamagnetic behavior. The intrinsic coercivity (H_c) of 222 Oe was observed for nitrogen doped graphene at 2K temperature.

MFM scan image shows a difference between nitrogen doped graphene and non-magnetic SiO_2 surface, whereas no difference was observed in MFM scan of pristine and -OH functionalized graphene. Which also confirmed presence of magnetization in nitrogen doped graphene. ESR spectroscopy shows a resonance in the case of nitrogen doped graphene and hence it confirms presence of free electrons in nitrogen doped graphene, which are reason for ferromagnetism in graphene.

AMR of nitrogen doped graphene was measured. AMR device fabrication and characterization using PPMS tool has been explained. Nitrogen doped graphene shows a good AMR response where resistivity of device changes with the variation of angle between the electrical current in device and magnetization of device. Orientation of magnetization

of device was varied from 0° to 360° and the change on resistivity was observed. Device shows a maximum AMR of 0.92% at 2K temperature.

Chapter 6

Sensors Based on Functionalized Graphene

Figure 6.1 shows the UV-Vis spectra of pristine CVD graphene and CVD graphene after treatment with H_2O_2 in the presence of UV light for 15 and 30 minutes. CVD graphene was transferred onto quartz to get absorbance UV-Vis spectra. Blank quartz, without graphene, was taken as the reference. UV-Vis spectra of hydroxyl functionalized graphene seems to shift towards UV-Vis spectra of RGO.

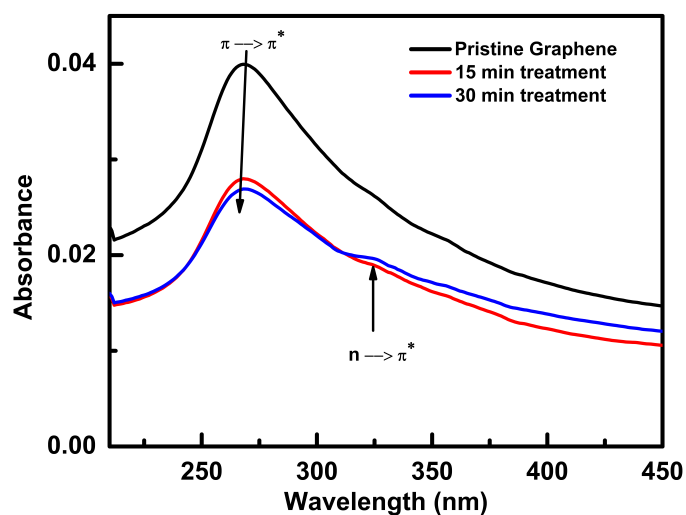


Figure 6.1: UV-Vis spectra of pristine CVD graphene and -OH functionalized CVD graphene on quartz.

UV-Vis spectroscopy gave an idea about change in optical properties of graphene after functionalization, so we tried to sense UV light using hydroxyl functionalized graphene because there is a shift in peak position in the UV range. Also graphene should become chemically reactive after functionalization and we explored some gas sensing applications of hydroxyl functionalized graphene.

An interdigitated electrodes circuit was designed for both sensing applications of hydroxyl functionalized graphene. Figure 6.2 (a) shows device fabrication process flow and figure 6.2 (b) is a schematic of the sensing device. Graphene strips shown in blue color are $20\ \mu\text{m}$ wide and $50\ \mu\text{m}$ long in size. Ni/Au ($20\ \text{nm}/30\ \text{nm}$) was deposited using e-beam evaporator as interdigitated electrode and for electrical connection. Keithley 2450 source meter unit was used for resistance measurement of the devices.

Graphene has very high electron mobility so it should provide a very fast response. It is a 2-D material with a high surface to volume ratio, so half of total area can be easily exposed for sensing. These factors can result in high sensitivity in graphene based sensors. Gas sensing based on graphene is due to adsorption and desorption of gas molecules on graphene surface. Depending upon the nature of gas, it will either donate an electron or a hole [102] to the graphene, which results in change of conductivity of graphene. By measuring resistance of graphene devices in absence and presence of gases/UV light the sensing properties of graphene can be extracted.

6.1 UV Sensor

Sensing devices were first tested in a in-house solar simulator. The lamp of solar simulator covered a long range of wavelength from $300\ \text{nm}$ to $1800\ \text{nm}$. A decrease in current of sensing device was noticed after exposure to light in solar simulator. Figure 6.4 (a) shows the current measured in dark condition after exposure to light for 15 seconds. When the current was measured immediately after light exposure a decrease of 24.8% was observed in current which got recovered with time as shown in figure 6.4 (b). Figure 6.4 (c) shows the current measured in the presence of light when light was on continuously

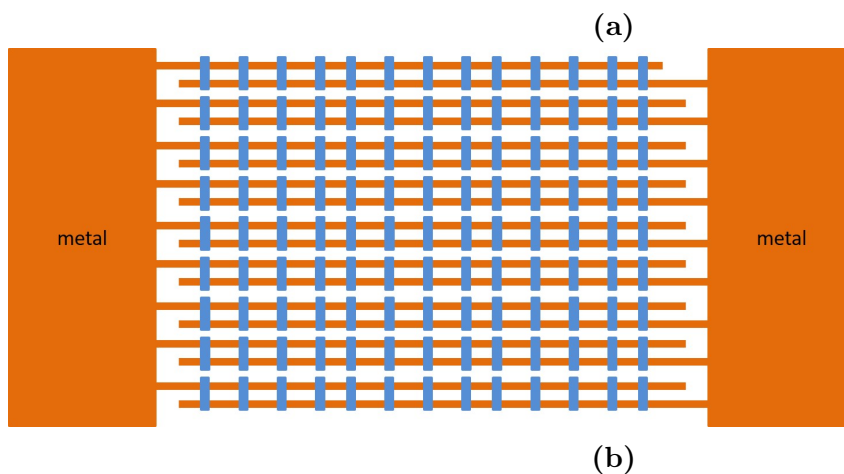
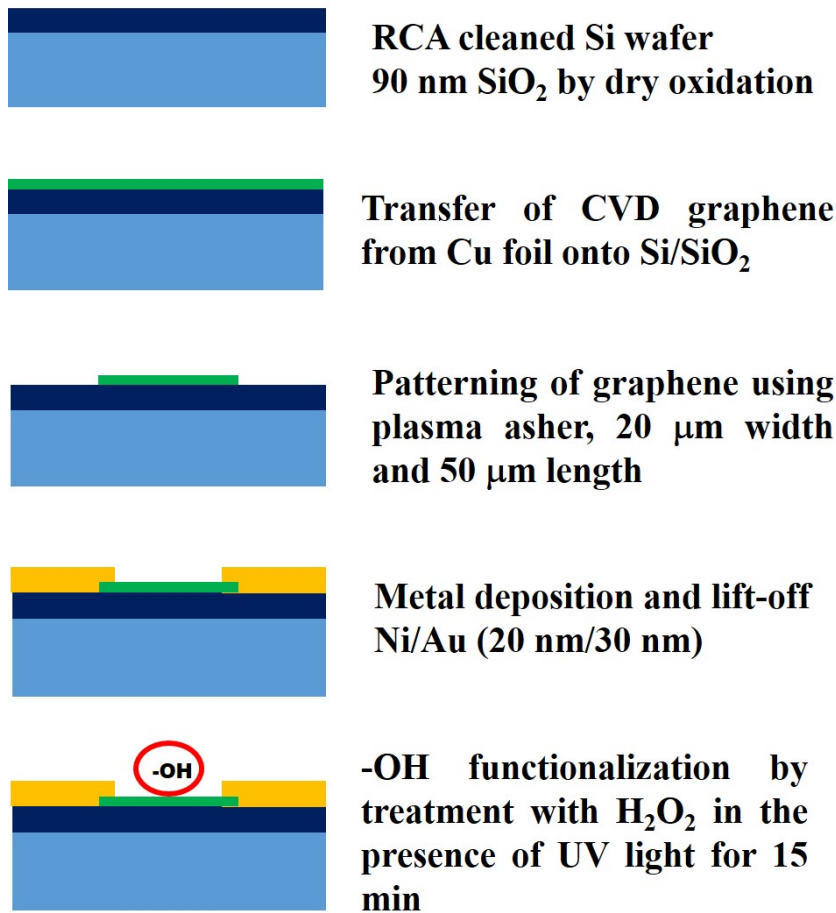


Figure 6.2: (a) Flow chart of sensor device fabrication (b) A schematic of the sensor device (top view).

and the current was recorded after every 30 seconds. A decrease of 56.4% was observed in current after 5 minutes of continues light exposure. Initially current decreases at a very fast rate when exposed to light and later rate of decrease of current reduces, as shown in

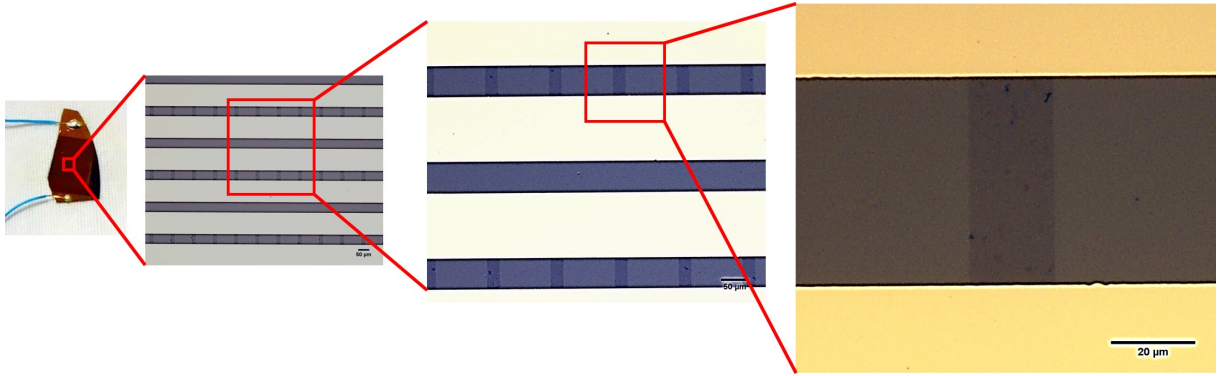


Figure 6.3: Photograph of a sensor device at different zoom levels.

figure 6.4 (d).

Solar simulator experiment shows that hydroxyl functionalized graphene is sensitive to light and shows a decrease in current after exposure. However it was not clear that which wavelength or wavelengths of light it is sensing. To check the wavelength, current was measured in solar cell quantum efficiency tool which measured current of devices at discrete wavelengths whereas lamp of in-house simulator was emitting all wavelengths together. We observed that device is responding to wavelengths only below 380 nm, as shown in figure 6.5.

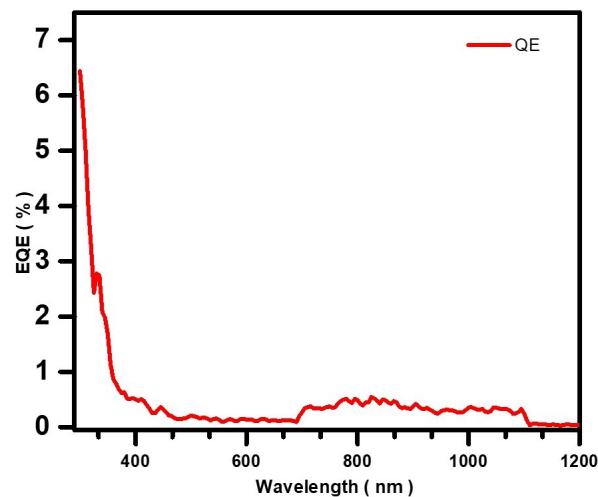


Figure 6.5: Response measured in quantum efficiency tool.

After confirmation that functionalized graphene is sensitive to wavelengths of UV range, functionalized graphene devices were tested for UV light using UV lamp of wave-

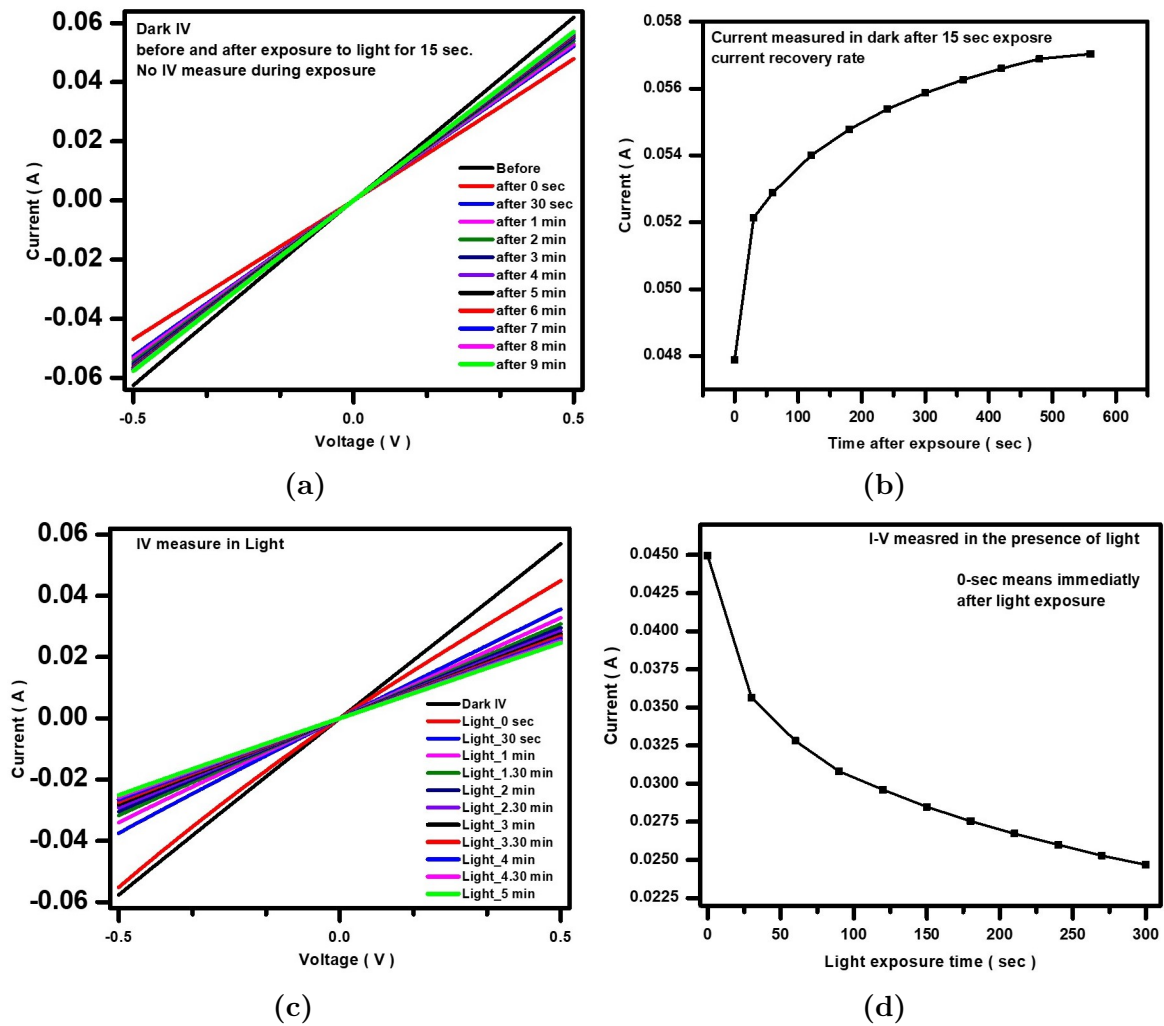


Figure 6.4: (a) Current measured in dark after 15 sec exposure of light. (b) rate of recovery of current in dark with time after 15 sec exposure of light. (c) current measured in presence of light until 5 minute of exposure. (d) rate of decrease in current in continuous exposure of light.

length 256 nm and intensity of 11 mW/cm^2 . Figure 6.6 shows response to UV light of 256 nm. Sensing device shows a response (R%) upto 19% for UV light pulses of 5 seconds. Recovery was also very fast, within few seconds the devices recovered to original value. Where R% is calculated using equation 6.1, where R_i is the initial resistance and R_o is the resistance after exposure. Multiple pulses of UV light was tested just to check repeatability of sensor and the device shows a very good repeatability. UV response of pristine graphene sensor were also tested and no response was noticed by pristine graphene, figure 6.7.

$$R\% = \frac{|R_i - R_o|}{R_i} \times 100 \quad (6.1)$$

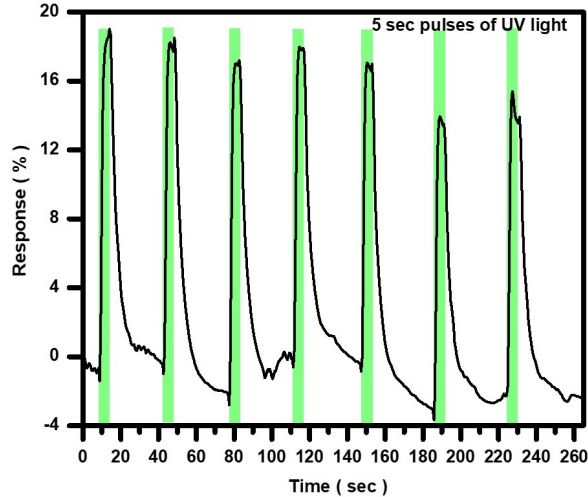


Figure 6.6: Response to UV light of hydroxyl functionalized graphene device.

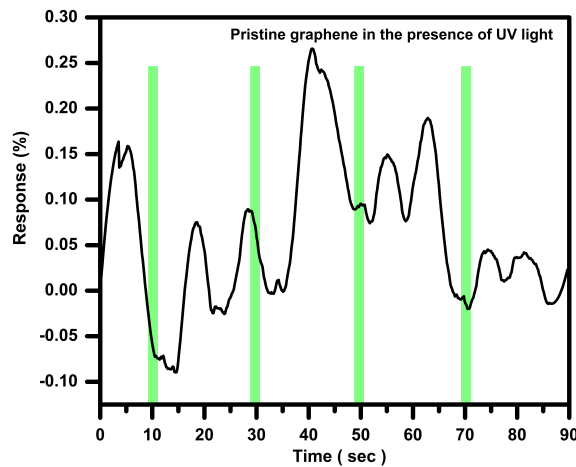


Figure 6.7: Pristine graphene device is behaving randomly and shows no response to UV light.

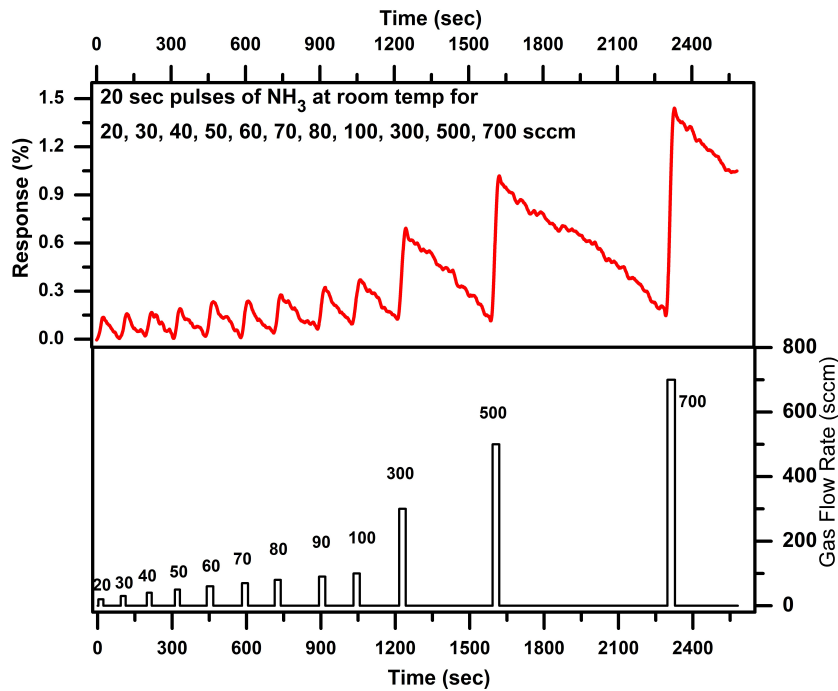
6.2 Gas Sensor

An in-house equipment was developed for gas sensing applications, details of which were described in section A.11. This sensing equipment is connected to a vacuum pump, having a substrate holder whose temperature can be raised up to 850 °C, and to four

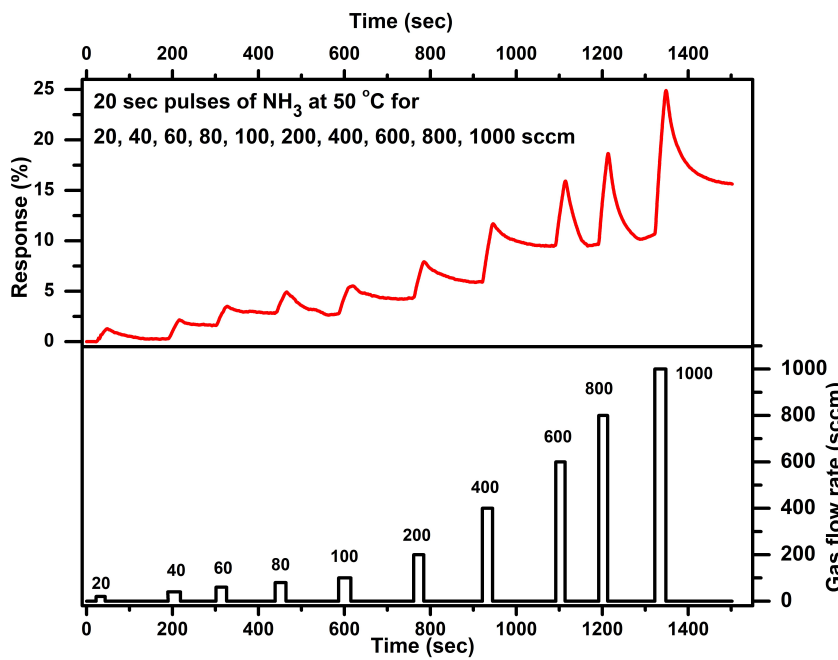
gas lines via four MFCs along with a digital MFC controller to control the gas flow rate precisely. External measurements were carried out through BNC female to female adapters attached to the chamber ports through which the sensing device kept inside the vacuum chamber can be connected to a source-meter.

6.2.1 Ammonia Sensor

Figure 6.8 shows the results for ammonia gas sensing by hydroxyl functionalized graphene sensing device. Gas was introduced at flow rates ranging from 20 sccm to 1000 sccm and the response was recorded as a change in the resistance of the graphene device. Hydroxyl functionalized graphene shows response to NH_3 gas immediately after gas was introduced into the chamber. Response was recorded at room temperature (RT) and after raising the device temperature to 50 °C. Figure 6.8 (a) and (b) shows the responses for different flow rates of gas vs time at RT and 50 °C respectively. Recovery after sensing can be noticed.



(a)



(b)

Figure 6.8: (a) Response vs time for NH₃ at room temperature for 20 sec pulses of NH₃ gas. (b) Response vs time for NH₃ at 50°C for 20 sec pulses of NH₃ gas.

In case of RT, the gas pulses of 20 seconds was flowed for 20, 30, 40, 50, 60, 70, 80, 100, 300, 500 and 700 sccm of gas. And in case of 50 °C the gas pulses of 20 seconds

was flowed for 20, 40, 60, 80, 100, 200, 400, 600, 800 and 1000 sccm of gas. Figure 6.9 (a) compares response measured at RT vs response at 50 °C for different gas flow rates. Response to ammonia gas increased many folds when temperature was raised to 50 °C from RT. To check the saturation of sensor, 1000 sccm of gas was flowed for longer time. In case of 50 °C, the response got saturated after 5 minutes and in case of RT, saturation didn't achieve even after 25 minutes, as shown in figure 6.9 (b). However rate of increase in response reduced after 7-8 minutes.

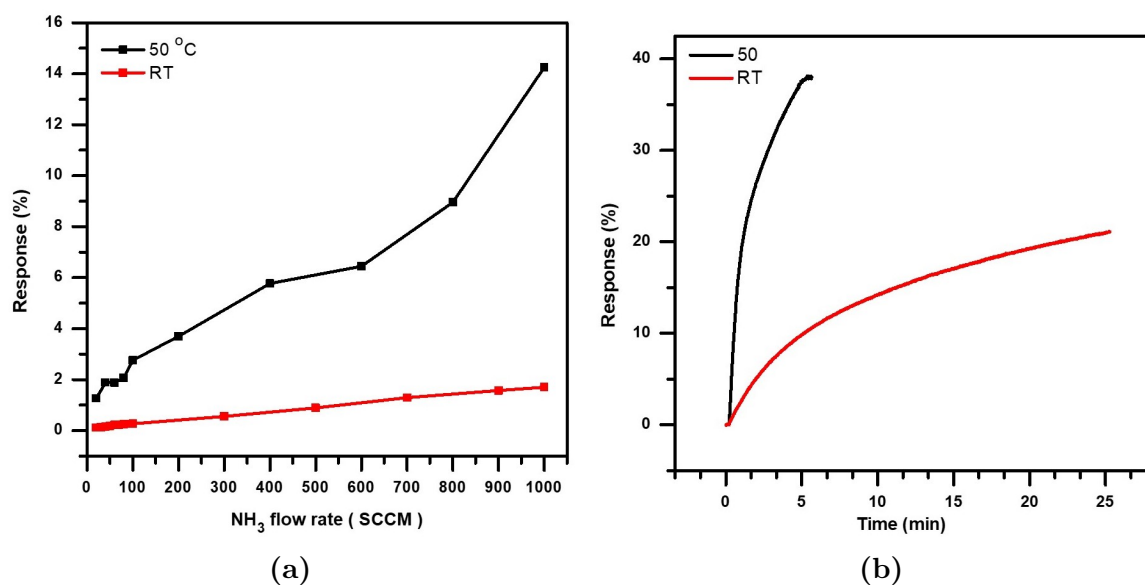


Figure 6.9: (a) Comparison of response at room temperature and 50°C. (b) Saturation for NH₃ gas at room temperature and 50°C.

To test repeatability, back-to-back multiple pulses of gas was flowed. The sensor response was recorded to detect whether it stop responding or any reduction in the maximum response after few pulses. As shown in figure 6.10 there is no degradation in response even after flowing 10 pulses of 100 sccm gas for 10 sec each back to back. These results show that one sensing device can be used multiple times.

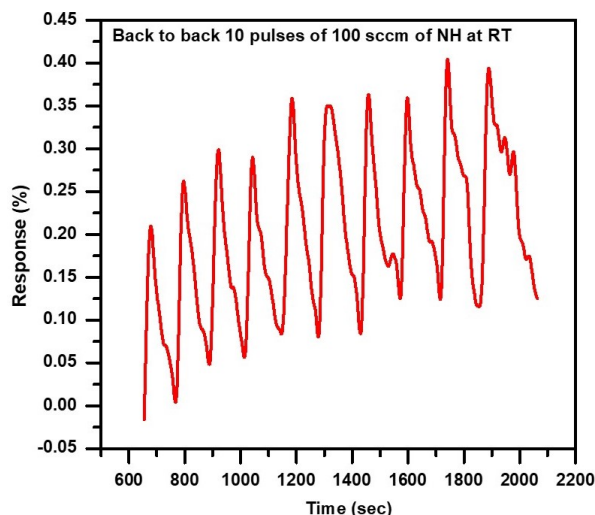


Figure 6.10: Response vs time for NH_3 at room temperature for back-to-back gas pulses of 10 sec, to check the repeatability of sensor.

After comparing these results with already reported sensors based on graphene, GO and RGO [?, 103, 104], we found that the sensor should be able to detect gas in the range of parts per million (ppm) or parts per billion (ppb). We used 100% NH_3 gas, so it is not possible to convert these results of sccm to ppm because there was only NH_3 gas present inside the chamber. Our hydroxyl functionalized graphene having very good mobility so it is showing very fast response to gas but due to problem with minimum gas amount which it can detect a good sensor can not be built using this graphene.

6.2.2 Hydrogen Sulfide Sensor

Figure 6.11 shows the response of hydroxyl functionalized graphene sensor device for 500 sccm of hydrogen sulfide (5% H_2S + 95% N_2) gas at room temperature. Device shows a good response of around 0.25% for 5% H_2S gas but again problem is that it is not in the range of ppm or ppb. Resistance of sensor devices increased in case of H_2S also, so sensing mechanism is same as sensing mechanism explained for NH_3 gas in next section.

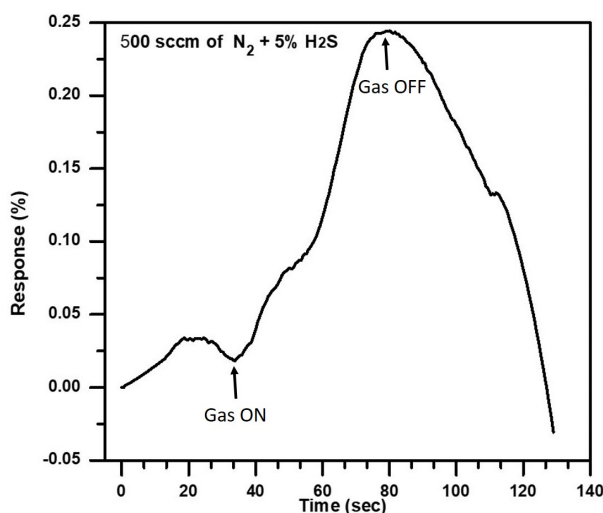


Figure 6.11: Response vs time for H_2S gas at room temperature for a 40 sec pulse.

Both gases show good preliminary results which need to be improved further by changing the device structure or degree of functionalization so that devices can sense gases in the range of ppm and ppb.

6.3 Discussions

UV sensing ability of -OH functionalized graphene was tested it is found that these devices show a reduction in current when exposed to UV light. This reduction in current after UV light exposure is not because of removal of hydroxyl groups from the graphene as the sensor device recovered fully and repeat the same response for multiple UV pulses. If there was a desorption of -OH groups after UV exposure, then the sensitivity should get reduced after each exposure because -OH groups are the key reason behind sensing and sensitivity is proportional to the -OH groups present for sensing. The phenomena behind sensing is not clear and 100% recovery eliminate the possibility of hydroxyl group removal. So we believe that hydroxyl groups are donating electrons to p-type graphene upon exposure to UV light which results in increase of resistance of graphene.

NH_3 and H_2S are electron donor gases [146, 147], and when a molecule of NH_3 get adsorbed on graphene surface, it gives electron to p-type doped graphene which results

in increase of resistance of graphene, as shown in the schematic in figure 6.12.

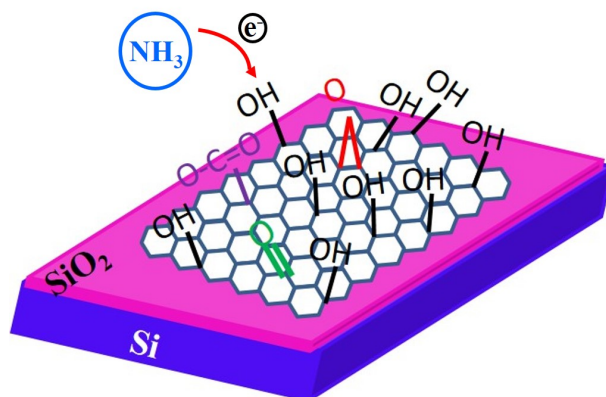


Figure 6.12: Schematic of electron donation from NH_3 to graphene.

6.4 Summary and Conclusions

Hydroxyl functionalized graphene device with interdigitated electrodes was used for sensing UV light, NH_3 and H_2S gases. Fabrication of sensing device has been explained. Sensing device shows a response of 19% to 256 nm UV light. Sensing devices show an immediate response to UV light and recovers fully after light was switched off. UV light didn't results in desorption of -OH functional groups after exposure.

Similar devices were also tested for gas sensing using a in-house built sensing setup. sensor shows a good response to both NH_3 and H_2S . In both cases sensor shows a response immediately when gas was introduced in the chamber and recovered after gas was shut down. For both the gases resistance of device increases after gas was flowed in the chamber. NH_3 and H_2S donate electron to -OH group which result in increase of a p-doped graphene after accepting electrons.

All the experiments related to sensing applications were conducted for preliminary assessment. More detailed interrogations including process optimizations are required for fully assess the potential for applications of hydroxyl functionalized graphene in sensors.

Chapter 7

Conclusions and Future Work

7.1 Conclusions

Exfoliated graphene and monolayer CVD graphene were functionalized by chemical treatment of graphene with H_2O_2 in the presence of UV light. Photo-chemically generated hydroxyl radicals and oxygen ions functionalized the graphene with hydroxyl and carbonyl groups and the same has been confirmed by Raman spectroscopy and XPS. This easy and low cost chemical method to hydroxyl graphene does not damage the graphene and similar process for graphene functionalization has not been reported in literature yet. Raman spectroscopy shows increase in I_D/I_G ratio after functionalization from 0 to 0.3 and deconvoluted C 1s XPS spectra shows increase of -OH group peak area from 10.70 % to 20.87 % after treatment. Hydroxylation of graphene was also tried by heating graphene in H_2O_2 , but that result in damaging the graphene as well.

Workfunction of functionalized graphene was tested using KPFM and a decrease in workfunction was observed after functionalization. Functionalized graphene has -OH termination on its surface which can be used for ALD of dielectric on graphene and we have shown deposition of thin Al_2O_3 layer via ALD on hydroxyl functionalized exfoliated graphene. Atomic layer deposition of Al_2O_3 on functionalized graphene open up the possibility to use graphene as channel in top gate devices. ALD of Al_2O_3 shows change in the surface properties of graphene after functionalization.

To test the electrical properties, the back-gated graphene FTEs were fabricated and IV characteristics shows a shift in Dirac point to higher voltage pointing to the p-type doping of the graphene. A reduction in hole mobility from $3830 \text{ cm}^2 \text{ V}^{-1} \text{ s}^{-1}$ to $1100 \text{ cm}^2 \text{ V}^{-1} \text{ s}^{-1}$ was observed. This mobility values are 100 times higher than reported mobility of GO and RGO. Vacuum stability of hydroxyl groups were tested by keeping samples in vacuum for 22 hours and hydroxyl groups shows very good stability. Vacuum stability was confirmed by XPS as well. XPS measurements were done under UHV condition and XPS spectra shows presence of -OH groups on graphene. Without vacuum stability they would not be able to sustain at such a ultra high vacuum and no -OH should be observed in XPS spectra.

Monolayer CVD graphene is doped with nitrogen after two step process of H_2O_2 treatment and ammonia annealing. H_2O_2 treatment in the presence of UV light results in -OH functionalization of graphene and NH_3 annealing of -OH functionalized graphene results in N doping of graphene. XPS and Raman spectroscopy confirms N doping of graphene. N doping of graphene introduce ferromagnetism in graphene which was confirmed by SQUID. M-H curve measured by SQUID magnetometer shows ferromagnetism in N doped graphene with a coercivity of 222 Oe at 2 K. Graphene devices shows AMR effect, where resistivity of graphene devices is monitored with respect to angle of current flow and angle of intrinsic magnetization by changing angle of applied magnetic field. ESR and MFM also confirmed presence of magnetization in nitrogen doped graphene. This process of nitrogen doping of graphene which introduce attendant magnetism in graphene could open the way for the applications of graphene in spintronics and other devices.

To check the change in optical properties, UV-Vis spectroscopy was done, and UV-Vis spectroscopy showed that the peak wavelength is shifting towards GO peak wavelength value after hydroxylation. UV sensing property of hydroxyl functionalized graphene was exposed and a high response of 19% to the UV light of wavelength 256 nm was observed.

Gases sensors based on functionalized graphene were also fabricated and it shows good sensitivity to ammonia and hydrogen sulfide. However the detection limit was very less compared tp those reported in literature.

Figure 7.1 summaries the work done in a flow chart format.

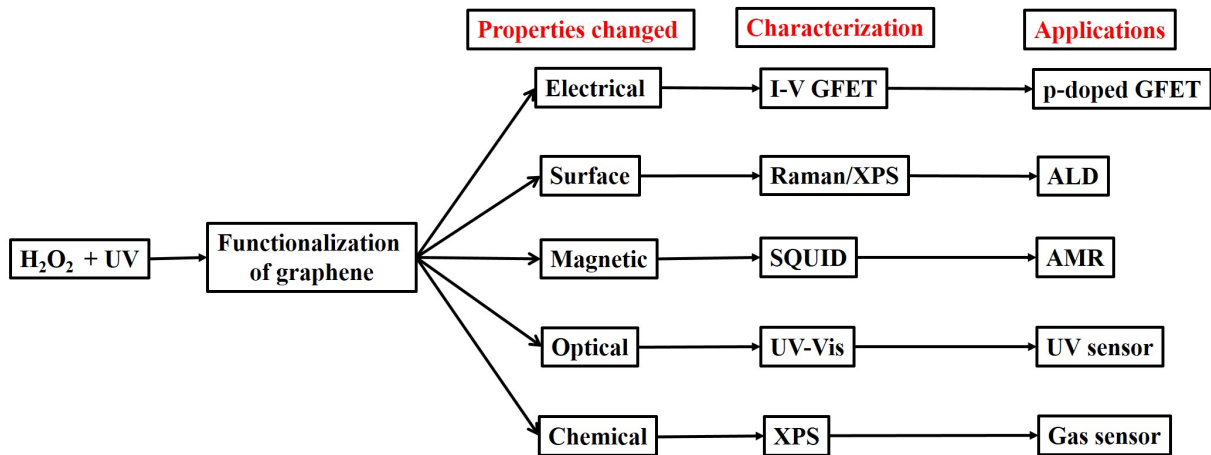


Figure 7.1: Summary of work.

7.2 Future Work

We believe following can be explored in future based on the results presented in this thesis:

1. Fabrication of top gate GFET and check if there any degradation in mobility after top dielectric deposition through ALD. Also spin coating or spray coating of Al_2O_3 by sol-gel method on functionalized graphene can be tried.
2. Improve sensitivity towards gases like NH_3 and H_2S and develop a low cost, fast response, flexible sensor based on functionalized graphene.
3. Apart from gases, functionalized graphene can be use for sensing of chemicals like acetone, toluene etc.
4. Functionalized graphene is bio-compatible and after making it magnetic, it can be used in bio medicines for magnetic field guided nanodrug delivery.
5. After introducing ferromagnetism in graphene, it can be used in spintronics for
 - spin FET

- spin hall effect
 - spin logic devices
 - spin memory device
 - magnetic field sensor
 - magnetic sensor to read magnetic encoders
6. Functionalized graphene shows response to UV light but mechanism is not clear and mechanism behind UV sensing can be explored and it can be use in optoelectronics devices.

Appendix A

Experimental Techniques

A.1 Laminar Flow Chemical Wet Bench

All chemical processes were done under laminar flow chemical wet bench. It is enclosed from five sides and draw air from one opening and filter the air and provide clean air to the working surface. Laminar flow wet bench was equipped with a 24-hour DI water line, electrical connections for connecting equipment likes hotplate and ultrasonicator, and a nitrogen gas line to dry the samples. Following processes were done under laminar flow wet bench: (1) RCA cleaning of silicon wafers, (2) CVD graphene transfer onto SiO₂/Si, (3) sample cleaning in acetone/IPA/DI water, (4) development during photolithography, (5) lift-off after metal deposition, (6) etching of SiO₂ in BHF and (7) H₂O₂ treatment of graphene.

A.2 Ellipsometer

SE 800 ellipsometer by SENTECH Instruments GmbH Germany was used to measure the thickness of thermally grown SiO₂ and Al₂O₃ deposited by ALD, figure A.1. The specifications of equipment are as follows:

- **Sample size:** minimum 1 cm X 1 cm and maximum 6 in X 6 in.
- **Spectral wavelength range:** 240 nm to 930 nm.

- **Angles for Measurement:** 40° - 90° , with 5° steps.
- **Parameters can be extracted:** Thin film thickness, refractive index, uniformity of films and layer stacks.
- **Software used:** Spectra Ray.



Figure A.1: Photograph of ellipsometer [148].

A.3 UV Exposure Unit

KUVC-2 model UV exposure unit manufactured by Kadavil Electro Mechanical Industries India was used for UV exposure of graphene samples, figure A.2. It is a closed chamber with UV lamps mounted inside. To expose samples they are left inside the chamber and lamps were switched on. The specifications of equipment are as follows:

- **Lamps available:**
 1. Short UV lamp: 256 nm.
 2. Long UV lamp: 365 nm.
 3. Fluorescent lamp: white light.

- **Sample size:** 156 mm x 156 mm.
- **View port:** one.



Figure A.2: Photograph of UV exposure unit.

A.4 Raman Spectroscopy

HR800-UV confocal micro-Raman spectrometer by Horiba Jobin Yvon Ltd. Japan was used for Raman spectroscopy, figure A.3. Specifications are as follows:

- **Excitation sources:** 532 nm 50 mW, and 633 nm 20 mW.
- **Microscope objectives:** 10x, 20x, 50x and 100x.
- **Scan type:** point scan and area mapping.
- **Resolution:** 10 fA and 10 nV.
- **Software used:** LabSpeck-5 and LabSpeck-6.
- **Temperature:** room temperature.



Figure A.3: Photograph of Raman spectroscopy instrument [149].

A.5 X-ray Photoelectron Spectroscopy (XPS)

Scanning XPS spectrometer PHI5000 VersaProbe II by ULVAC-PHI Inc., equipped with monochromatic Al $K\alpha$ radiation source at a pressure of 10^{-9} mbar was used for XPS analysis. Specifications are as follows:

- **X-ray beam diameter:** 10 μm to 200 μm .
- **Ion beam energies:** 5 eV to 5 keV.
- **Capabilities:**
 1. Scanning X-ray Imaging (SXI).
 2. Micro area spectroscopy.
 3. Macro area spectroscopy.
 4. Sputter depth profiling.
 5. Angle dependent depth profiling.

6. Line scan and mapping.

7. Ultraviolet Photoelectron Spectroscopy (UPS).

- **Sample type:** thin film and powder.
- **Load lock:** available.
- **Substrate size:** upto 12 inch.
- **Temperature:** room temperature.
- **Base vacuum:** 10^{-9} mbar.
- **Software used:** MultiPak.
- **Gases used:** Compressed Dry Air (CDA), He, N₂, Ar.



Figure A.4: Photograph of X-ray Photoelectron Spectroscopy instrument.

A.6 Atomic Force Microscope (AFM)

MFP3D Origin AFM of Oxford Instruments Asylum Research Inc. California was used for topographic scans, Kelvin Probe Force Microscopy (KPFM) scans for workfunction determination, and Magnetic Force Microscopy (MFM) scans to check magnetization

in nitrogen doped graphene, figure A.5. Specifications are as follows:

- **Capabilities -**

1. AFM (contact and tapping modes)
2. Conducting AFM
3. Electrostatic force microscopy
4. Magnetic force microscopy
5. Piezoelectric force microscopy
6. Kelvin probe force microscopy

- **Scan area:** maximum of $90 \mu\text{m}^2$ X $90 \mu\text{m}^2$ and minimum of around 10 nm to 30 nm.

- **Noise isolation:** yes.

- **Software used:** Igor Pro.



Figure A.5: Photograph of AFM measurement instrument.

A.7 Scanning Electron Microscope (SEM)

SEM imaging was done using Raith150^{two} SEM instrument of Raith GmbH, figure A.6. The specifications of Raith150^{two} are as follows:



Figure A.6: Photograph of Raith150^{two} SEM equipment [148].

- **TFE Filament with Beam size:** ≤ 2 nm at 20 kV.
- **Beam energy:** 100 eV to 30 keV.
- **Stage travel range:** 150 mm x 150 mm x 20 mm.
- **Current density:** $\geq 20,000$ A/cm².
- **Current stability:** ≤ 0.5 % / 8 hours.
- **Minimum line width:** < 20 nm.
- **Stitching accuracy:** ≤ 40 nm (mean +3 sigma).
- **Overlay accuracy:** ≤ 40 nm (mean +3 sigma).
- **Process capabilities:** imaging, lithography, Electron beam-induced deposition (EBID).
- **Substrate size:** for surface imaging- small pieces up to 100 mm or 4" wafer, for

cross sectional imaging at 45°: 20 mm W x 10 mm H and at 90°: 20 mm W x 7 mm H.

A.8 Photolithography Tool

EVG 620 Double Sided mask Aligner (DSA) manufactured by EV Group (EVG) Austria was used for photolithography to fabricate graphene devices, figure A.7. Specifications of the tool are as follows:

- **Exposure mode:** soft, hard, vacuum contact.
- **separation distance:** 0-300 μm .
- **Wafer thickness:** 0.1 - 10 mm.
- **Lamp:** 500 W Hg lamp.
- **Wavelength range:** 650 - 450 nm.
- **Alignment accuracy:** 0.5 μm for top side and 1 μm for bottom side.
- **Minimum feature size achievable:** 2 μm .
- **Substrate size:** 2 and 4 inch.
- **Mask plate size:** 3 and 5 inch.
- **Gas used:** nitrogen (5N purity).



Figure A.7: A photograph of EVG 620 photolithography tool [148].

A.9 E-beam Metal Evaporator

6 target e-beam metal evaporator ATC-ORION-8E by AJA International Inc. USA was used for metal deposition. Specifications are as follows:

- **Main power supply:** 5 kW.
- **Total metal targets:** six numbers.
- **Metals used in thesis work:** Nickle, Gold, Platinum.
- **Deposition rate control:** Å/sec.
- **Load lock:** available.
- **Substrate size:** upto 4 inch.

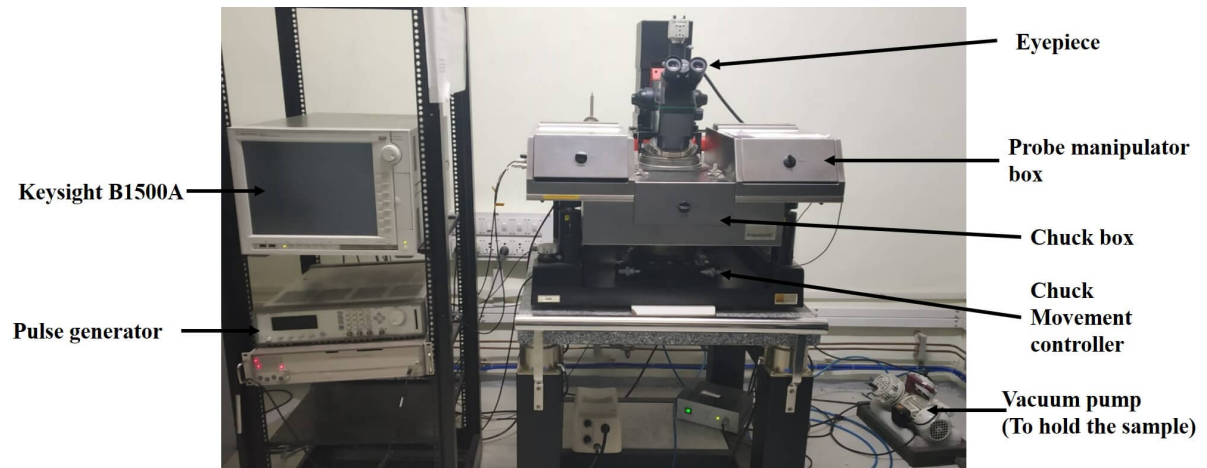
- **Temperature:** room temperature.
- **Base vacuum:** 4×10^{-8} Torr.

A.10 Electrical Characterization

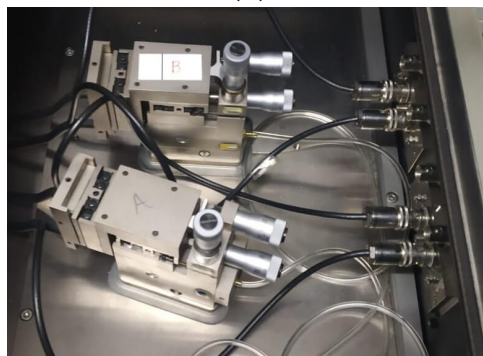
Keysight Technology B1500A semiconductor device analyser was used for current - voltage (I-V) characterization of GFETs, figure A.8.

Specifications of the system are as follows:

- **Measurement modes:** I-V/ capacitance - voltage (C-V) measurement/ pulsed I-V/fast I-V/transient I-V measurement and pulse generation.
- **Operating temperature:** room temperature.
- **Number of probes:** four probes with manipulator and one chuck.
- **Voltage range:** upto ± 100 V.
- **Voltage resolution:** $0.5 \mu\text{V}$.
- **Current resolution:** 1 fA.
- **Frequency range:** 1 kHz to 5 MHz.
- **Software used:** Keysight EasyEXPERT application.
- **Substrate size:** upto 8 inch.



(a)



(b)



(c)

Figure A.8: Photograph of (a) I-V measurement setup (b) probe manipulators (c) chuck.

Keithley 2450 source-meter of Tektronix Inc. USA was used for current measurement of sensor devices, figure A.9. Specifications are as follows:

- **Current range:** 10 nA to 1 A.
- **Voltage range:** 20 mV to 200 V.
- **Software used:** KickStart.



Figure A.9: Photograph of Keithley 2450 connected with a laptop for current measurement.

A.11 Graphene Annealing and Sensing Setup

An in-house built equipment was used for graphene annealing and gas sensing experiments, schematic of the equipment is shown in figure A.10 and photographs in figure A.11. It has a 4" substrate holder with a heater for raising temperature upto 850°C. It is connected to a dry roughing pump, Pirani gauge to measure vacuum, a throttle valve between vacuum and chamber to control the pressure inside the chamber, four gas lines, four Mass Flow Controllers (MFC), MFC digital controller, and four BNC female connectors for connecting samples kept inside the chamber with a source-meter kept outside. The specifications of the equipment are as follows:

- **Vacuum level:** upto 3×10^{-2} mbar with a control of 0.1×10^{-2} mbar with the help of throttle valve.
- **Temperature:** room temperature to 850°C.
- **Gases used:** N₂, NH₃, CH₄, H₂S, Ar, N₂ + H₂ (5% H₂).
- **Gas flow rate:** from 10 sccm to 1000 sccm.
- **Electrical connections:** can be connected to two source meters with BNC male

cables.

- **Substrate size:** upto 4".

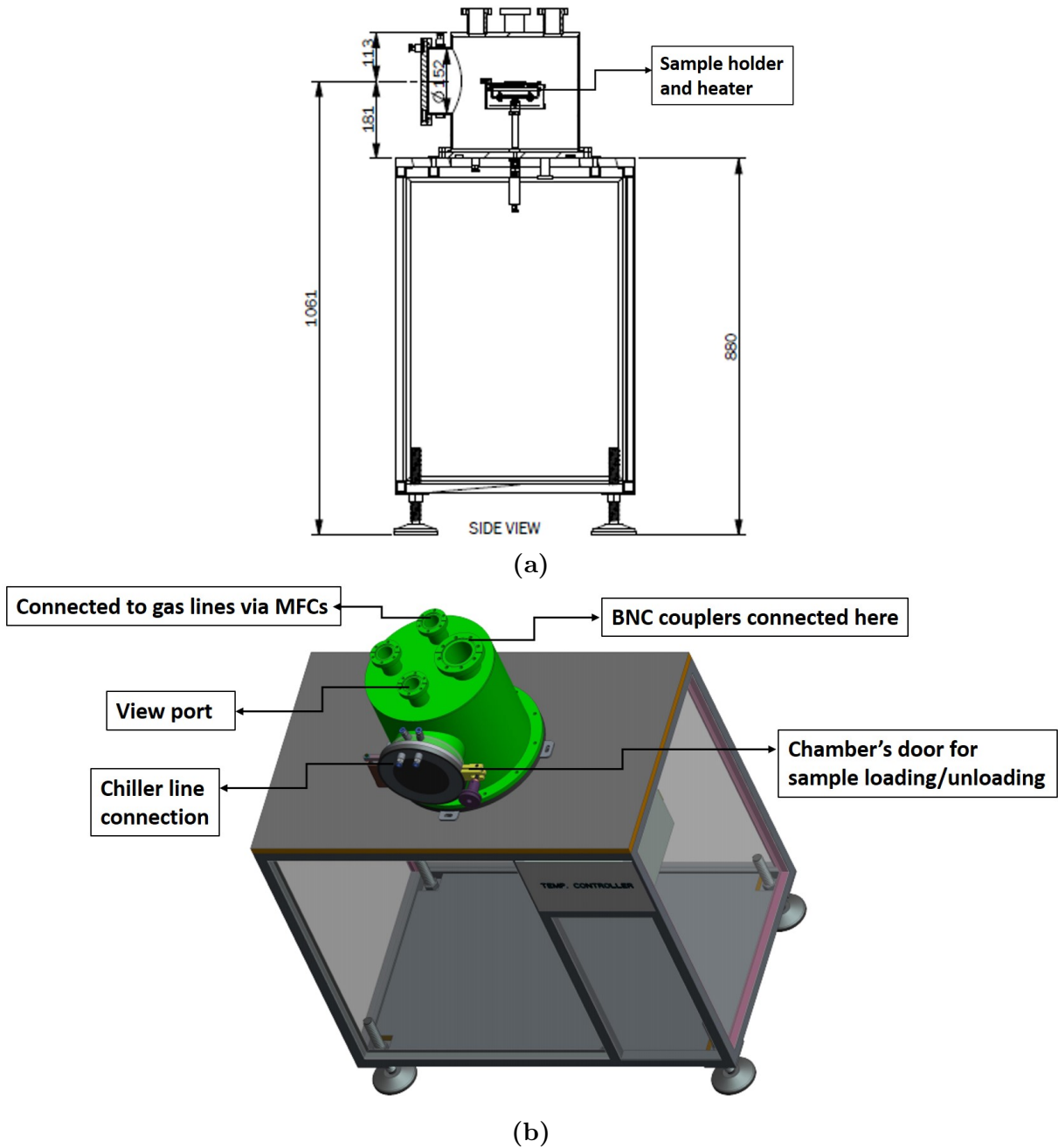
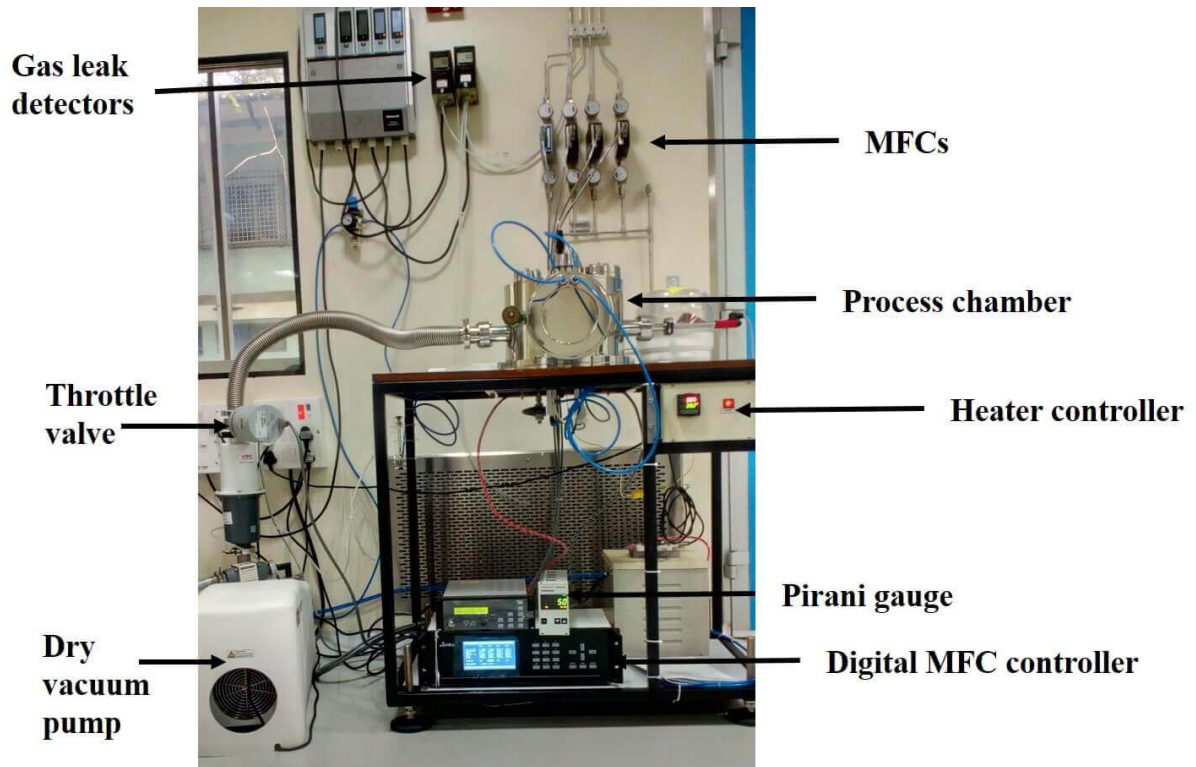
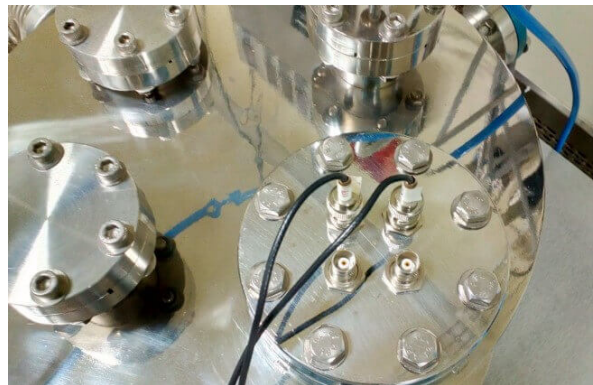


Figure A.10: Drawing of in-house built graphene annealing and sensing setup (a) side view. (b) top view.



(a)



(b)

Figure A.11: Photograph of (a) Graphene annealing and sensing setup (b) BNC connectors for electrical measurements.

A.12 Superconducting Quantum Interference Device (SQUID)

MPMS 3 SQUID magnetometer by Quantum Design Inc. USA was used for magnetisation measurements. The specifications of the equipment are as follows:

- **Operating temperature range:** 1.8 K to 400 K.
- **Magnetic field range:** -70 kOe to +70 kOe.
- **Cooling/heating rate:** upto 30 K/min.
- **Resolution:** $\leq 8 \times 10^{-8}$ emu.
- **Variable drive amplitude:** 0.1 to 8 mm (peak).
- **Sample chamber internal diameter:** 9 mm.
- **Sample size (maximum):** length ~ 10 mm, breadth ~ 0.5 mm, thickness ~ 0.5 mm.
- **Sample:** bulk/thin film/powder.

A.13 Physical Property Measurement System (PPMS)

DynaCool Physical Property Measurement System by Quantum Design Inc. USA was used for AMR measurements, figure A.12. A horizontal rotator was used to rotate the sample from -10° to 360° and sample was mounted on the rotator with the help of a chip, and loaded inside the PPMS. Horizontal rotator and chips for mounting samples in different orientation are shown in figure A.13. The specifications of the equipment are as follows:

- **Operating temperature range:** 2 K to 400 K.
- **Magnetic field range:** -90 kOe to +90 kOe.
- **Cooling/heating rate:** upto 30 K/min.
- **DC resistance measure range:** $10 \mu\Omega - 10 M\Omega$ in a standard 4-probe configuration.



Figure A.12: Photograph of PPMS instrument.

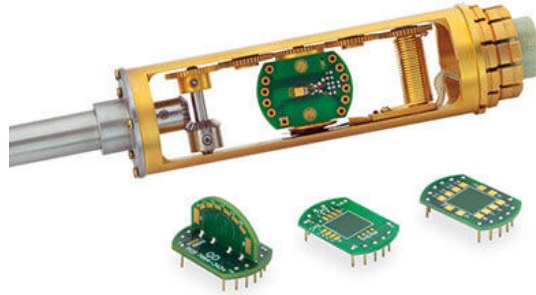


Figure A.13: Photograph of horizontal rotator and sample mounting chips [150].

A.14 Electron Spin Resonance (ESR)

JES - FA200 Electron Spin Resonance spectrometer by JEOL Ltd. Japan was used for ESR characterization of graphene samples, figure A.14. The specifications of equipment are as follows:

- **Frequency Band:** X-band, 8.75 GHz - 9.65 GHz.
- **Sensitivity:** 7×10^9 spins per 0.1 mT.
- **Resolution:** $2.35 \mu\text{T}$.
- **Temperature:** Any temperature from liquid nitrogen temperature (77 K) to

200°C.

- **Sample size:** 5 mm X 3 mm X 2 mm.



Figure A.14: Photograph of electron spin resonance spectrometer [149].

Appendix B

Surface Treatment of SiO₂ Before Graphene Transfer

For applications of graphene in semiconductor devices it is necessary to transfer CVD graphene from metal substrate to a required substrate. Transfer of one atomic thin layer of graphene is the most critical process and affect the GFETs performance [151]. The most common used transfer process is to deposit polymethyl-methacrylate (PMMA) as supporting layer on graphene and then etch out the metal substrate and transfer PMMA/graphene stack onto required substrate and remove PMMA with acetone [152], as explained in section 3.1.1. In the process of graphene transfer onto SiO₂/Si substrate, different techniques for surface treatment of SiO₂ before graphene transfer to increase the hydrophilicity and roughness of SiO₂ surface, to improve the adhesion of graphene with SiO₂ surface and to remove organic residues have been reported [153]. The reports so far have demonstrate the following treatments before transfer: (i) HF dip [154], (ii) O₂ plasma treatment [153], (iii) UV-ozone treatment [155], and (iv) deposition of hexamethyldisilazane (HMDS) layer between graphene and SiO₂ [156]. The effect of these treatments on GFET performance were reported. However reason behind the degradation or improvement in GFETs performance because of surface treatment techniques is not explained well.

We have tried different surface treatments and studied their effect on GFET performance, which is explained in further sections.

B.1 SiO₂ Surface Treatment

We have studied the reasons behind the improvement in GFETs performance after forming gas annealing of SiO₂, and degradation in performance after O₂ and Ar plasma treatments of SiO₂ just before the CVD graphene transfer. We used contact angle measurement, AFM, and XPS to characterize the SiO₂/Si substrate after different treatments. Change in the values of siloxane group (Si-O-Si), silanol groups (Si-OH) and SiO₄ groups present in SiO₂ gives an idea about the mobility degradation and instability in the I-V characteristics in case of plasma treated samples.

Four different types of samples were prepared based on SiO₂ surface treatment before graphene transfer. Process flow for device fabrication is shown in figure B.1.

1. **No treatment** - as grown SiO₂ was used without any surface treatment
2. **FGA** - forming gas (5% H₂ + 95% N₂) annealing after oxidation
3. **O₂ plasma** - post FGA treatment with oxygen plasma for 5 min at 50 W
4. **Ar plasma** - post FGA treatment with Ar plasma for 5 min at 50 W

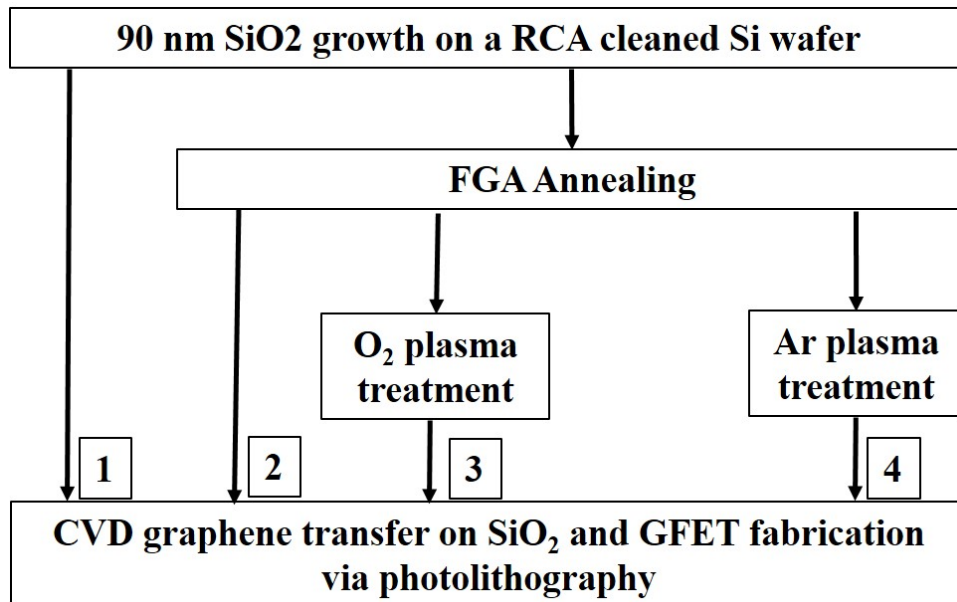


Figure B.1: Process flow showing different types of surface treatments.

FGA samples were cleaned with acetone, IPA and DI water before proceeding for plasma treatment. Graphene was transferred immediately onto SiO₂/Si after surface treatment of SiO₂ with O₂ and Ar plasma.

GFETs were fabricated using photo-lithography. For transfer characteristics, the source-drain (I_D) current of all GFETs was measured by sweeping the back gate voltage (V_G) from -25 V to +25 V while keeping the source-drain voltage (V_{DS}) fixed at 0.5 V. A comparison of the transfer characteristics of GFETs fabricated on SiO₂ without any treatment and SiO₂ after FGA are shown in figure B.2. GFETs fabricated on SiO₂ with FGA shows higher mobility, more symmetric I-V characteristics, as shown in figure B.2 (a), and better current stability as compared to GFETs on as grown SiO₂ without any treatment, as shown in figure B.2 (b). Hydrogen ambient annealing of SiO₂/Si eliminates the dangling bonds present the Si-SiO₂ interface and which acts as interface traps, which results in GFETs performance [157]. So, we choose SiO₂ with FGA for fabrication of all type of devices further.

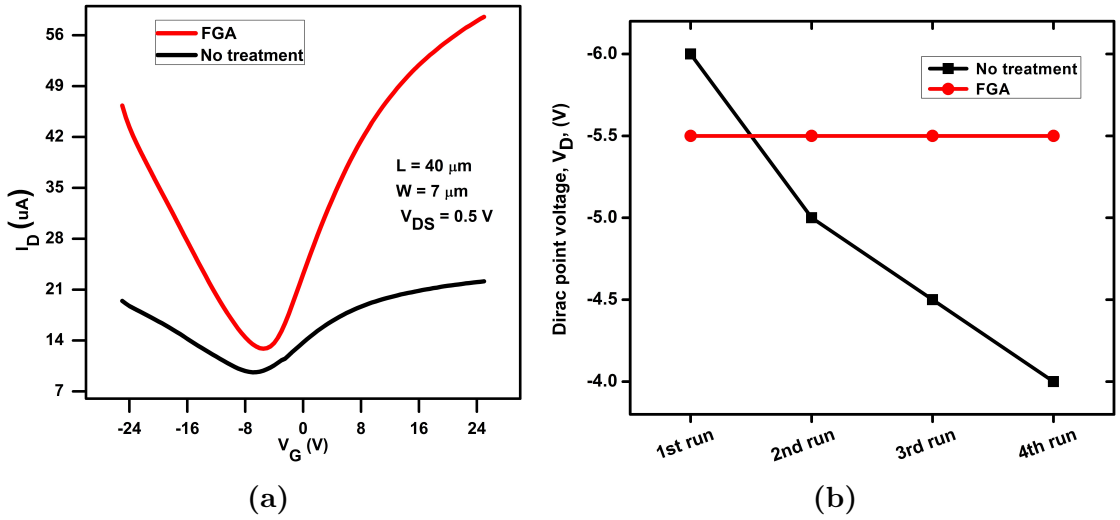


Figure B.2: (a) Comparison of the transfer characteristics of GFETs fabricated on SiO₂ without any treatment and with FGA. (b) Comparison of shift in Dirac point position with multiple measurement runs back-to-back on the same device.

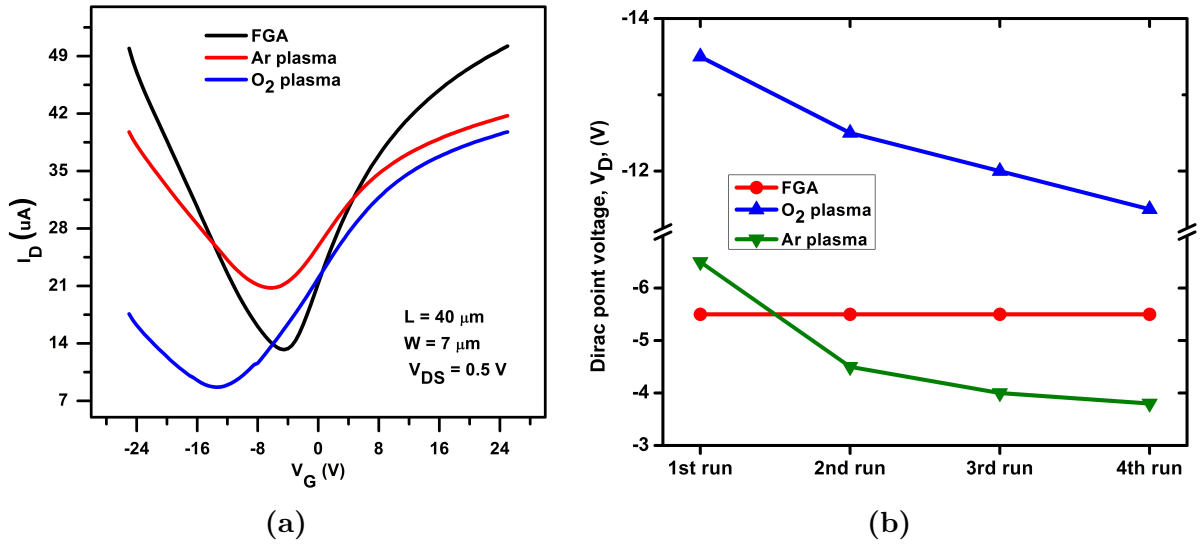


Figure B.3: (a) Transfer characteristics of GFETs fabricated on three types of SiO₂ - FGA, O₂ plasma treated and Ar plasma treated (b) shift in CNP with multiple measurement runs back-to-back.

Figure B.3(a) shows the comparison of transfer characteristics of GFETs on three types of samples - FGA, O₂ plasma treated and Ar plasma treated. Mobility of GFETs decreases after O₂ and Ar plasma treatments, as the slope of I_D vs V_G curve decreases, figure B.3(a). Both the electron and hole mobility reduces for plasma treated samples. Reduction in mobility is mainly due to scattering of the charge carriers at the graphene/SiO₂ interface. Charge neutrality point (CNP) for the Ar plasma treated sample occurs at Dirac voltage (V_D) equal to -6.5 V and for O₂ plasma treated sample of $V_D = -12.5$ V whereas for FGA sample it is -5.5 V. This shift in CNP after plasma treatment shows n-doping of graphene by plasma treated SiO₂ surface. The Raman spectra of graphene transferred onto FGA, O₂ plasma treated and Ar plasma treated SiO₂, shown in figure B.4, shows a signature of p-type doping (not n-type doping), as G peak position shows blue shift [51], for graphene transferred onto Ar plasma and O₂ plasma treated SiO₂. This suggests that the graphene-SiO₂ interface is responsible for a negative shift of CNP.

CNP point for O₂ plasma and Ar plasma devices shift toward positive voltage with every measurement when tested for multiple measurements runs back-to-back on the same device, whereas in case of FGA SiO₂, CNP is more stable and there is no shift in CNP

with back-to-back measurements, shift in CNP with back-to-back measurements is shown in figure B.3 (b). This shift in CNP may be because of doping of graphene by SiO₂ surface, the charge trap at the graphene/SiO₂ interface, and change in chemical composition of SiO₂ after plasma treatments.

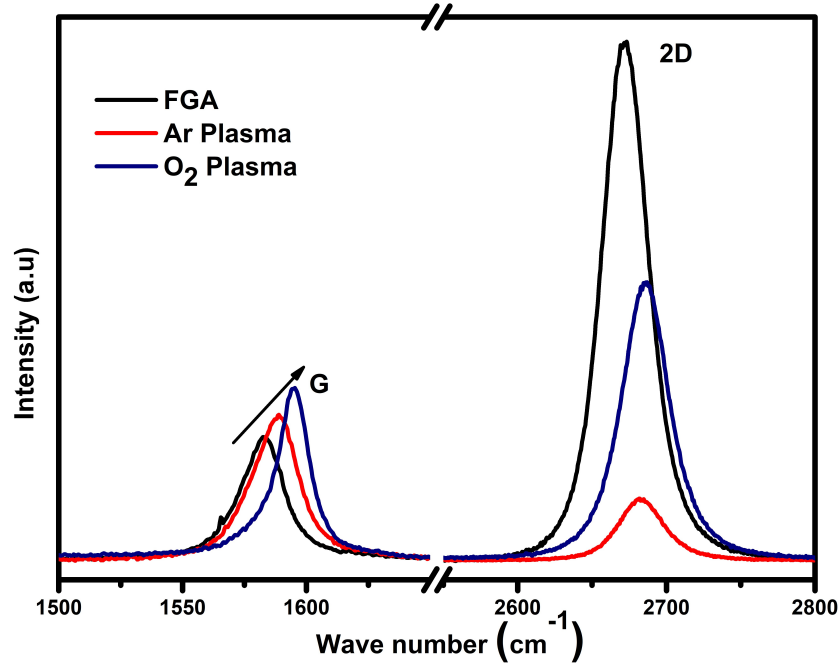


Figure B.4: Raman spectra of graphene transferred onto three types of SiO₂

B.2 Characterization of SiO₂ Surface After Treatment

B.2.1 Contact Angle Measurement

Contact angle on the SiO₂ surface was measured by $\theta/2$ method ($\theta = \frac{\theta_L + \theta_R}{2}$) by looking at the photographic image of 1 μ L droplet of DI water on the SiO₂ surface, as shown in inset of figure B.5. Contact angle (θ) for FGA SiO₂ was 72° which reduces to 36° after O₂ plasma treatment and 25° after Ar plasma treatment, which means SiO₂ become more hydrophilic after Ar and O₂ plasma treatment. Figure B.5 shows values of contact angle. Increase in wettability means that more water molecules incorporated at the graphene/SiO₂ interface. The instability in current-voltage characteristics with

back-to-back measurements is mainly due to polarization of water molecule adsorbed at the graphene/SiO₂ interface for plasma treated samples [153].

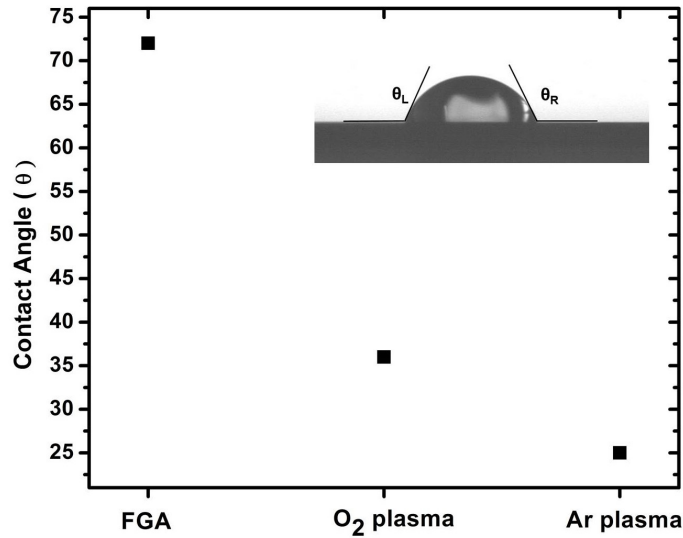


Figure B.5: Contact angles for different samples prepared with different types of SiO₂ surface treatment.

B.2.2 AFM Characterization

Table B.1 shows values of RMS roughness and maximum height calculated by AFM operated in contact mode for a 5 μm × 5 μm scan on SiO₂ surface before and after O₂ and Ar plasma treatments. This increase in roughness indicates increases in the hydrophilicity of the SiO₂ surface, and the same was confirmed by contact angle measurement also.

Table B.1: RMS roughness and max height values for three samples calculated through 5 μm AFM scan

Sample	RMS Roughness (nm)	Max. Height (nm)
FGA	0.584	7.76
Ar Plasma	0.615	9.93
O ₂ Plasma	1.03	21.8

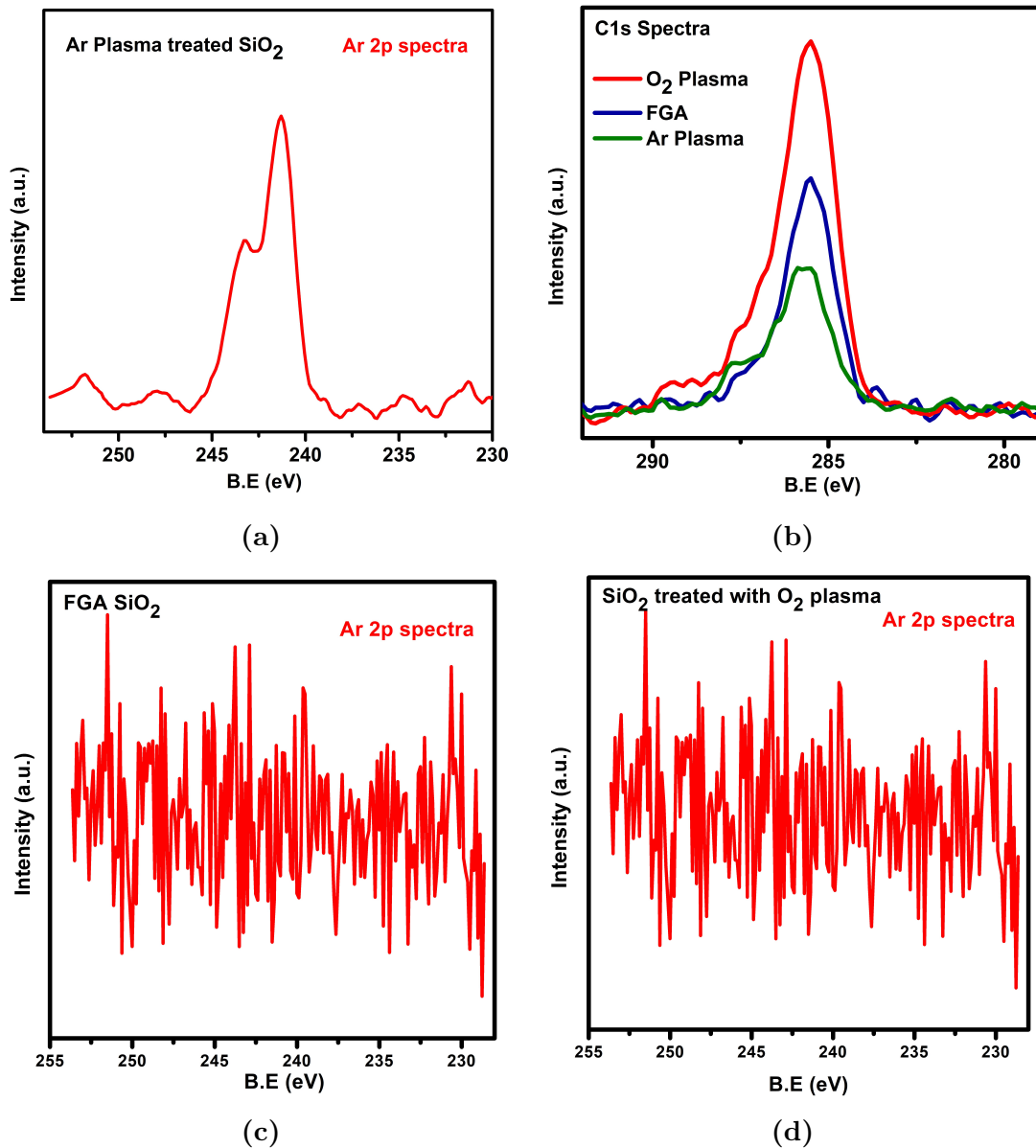


Figure B.6: (a) Ar 2p XPS spectra of the sample treated with Ar plasma (b) Comparison of C 1s XPS spectrum of the surface of SiO₂ for the FGA, O₂ plasma and Ar plasma treated, (c) Ar 2p spectra for FGA SiO₂, and (d) Ar 2p spectra for O₂ plasma treated SiO₂.

B.2.3 XPS Characterization

Figure B.6 (a) shows Ar 2p XPS spectrum for the SiO₂ sample treated with Ar plasma. For Ar plasma treated sample a clear Ar 2p peak can be seen, whereas this signature was absent for FGA and O₂ plasma treated samples, as shown in figure B.6 (c) and (d) respectively. This shows argon embedded inside the SiO₂/Si substrate which may

results in increase of positive charges and deep acceptor type interface state generation [158].

Figure B.7 shows deconvoluted O 1s XPS spectrum for all three samples. Before deconvolution of O 1s spectrum, the O peak was shifted to 531.9 eV [159] to compensate for charging effect. O 1s spectra deconvoluted mainly into three peaks Si(-OH)_x, Si(-O)₂ and Si(-O)₄, at 531.1 eV, 531.9 eV and 532.9 eV respectively [159]. Values shown in figure B.7

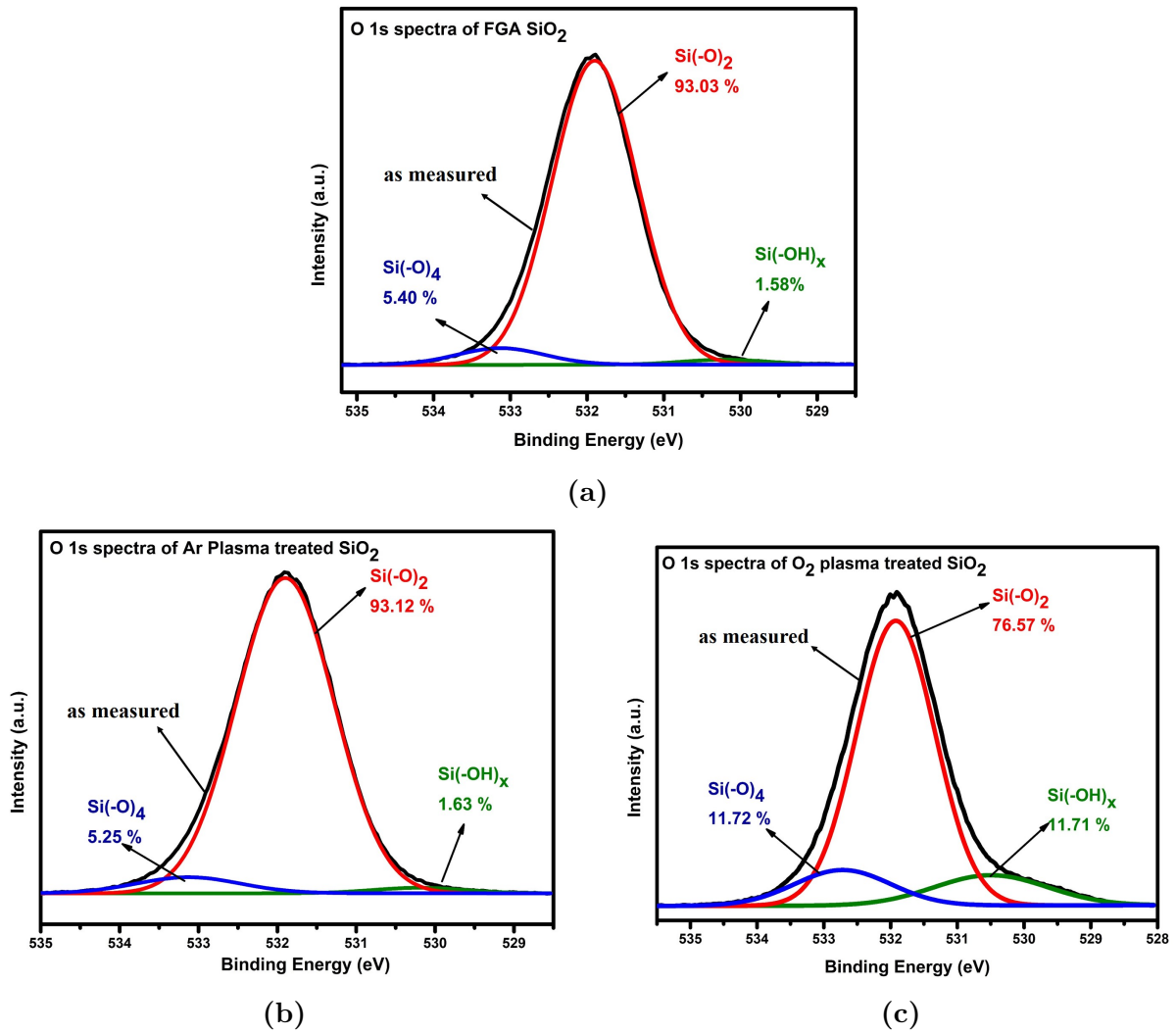


Figure B.7: Deconvoluted O 1s XPS spectrum of the surface of SiO₂ for (a) FGA, (b) Ar plasma and (c) O₂ plasma treated samples.

are the area percentage of corresponding peaks after deconvolution and the comparison of area percentage of different deconvoluted peak for each sample is shown in figure B.8. For the FGA SiO₂ sample, the contribution of the Si(-O)₂ is 93.03 %, Si(-O)₄ contribute

5.40 % and Si(-OH)_x contribute 1.58 % to the total O 1s spectrum. These values are almost same of the Ar plasma sample, which means Ar plasma is not disturbing silicon - oxygen bond configuration and the instability in I-V characteristics is only because of argon embedded inside the SiO₂/Si substrate which results in increase of positive charges and deep acceptor type interface state generation and Ar plasma creates defects which act as scattering centers [158]. After O₂ plasma treatment there is a huge increase in

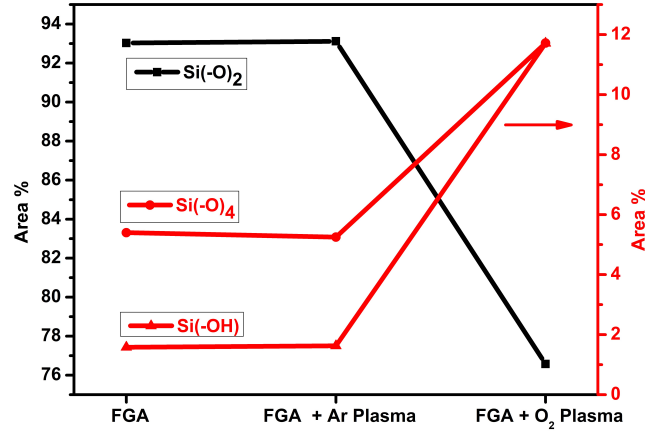
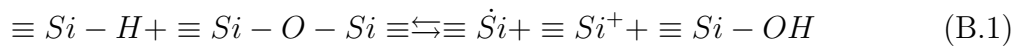


Figure B.8: Comparison of area percentage values of deconvoluted peaks of O 1s XPS spectrum of the surface of SiO₂ for FGA, Ar plasma and O₂ plasma treated.

the area percentage of Si(-O)₄ and Si(-OH)_x peaks. Si(-O)₄ area percentage increases to 11.4% which acts as donors and Si(-OH)_x area percentage increases to 11.71% which acts as electron traps [160] in our samples and results in CNP shifting and instability in I-V characteristics.

Breaking of the siloxane bonds and making of silanol bonds is explained by the equation B.1 [160].



Comparison of different surface treatment techniques reported in literature till date is shown in table B.2. Contact angle value of our FGA sample is similar to contact angle of H₂O and Acetone/IPA sonicated SiO₂ reported in [155], as we also cleaned our FGA samples with acetone, IPA and DI water before contact angle measurement. Similar to

other reported work, we also observed a decrease in mobility and increase of instability of current in GFETs after plasma treatment of SiO₂ before graphene transfer. Goniszewski et al. [155] had correlated changes in contact angle with the changes they observed in electrical characteristics but the reason behind the changes is not explained. k. Nagashio et al. [153] Tried to explained the reason for changes in electrical characteristics for HF etching, O₂ plasma and re-oxidation of SiO₂ surface but they have not discussed the asymmetry and instability in IV characteristics. Lafkioti et al. [156] showed improvement in hysteresis by depositing HMDS layer between graphene and SiO₂. But reason behind the improvement was not explained. In our study FGA samples without any plasma treatment shows better results with an increase in mobility, symmetric IV and stability in current as compare to (i) without any treatment as grown SiO₂, (ii) O₂ plasma treated, and (iii) Ar plasma treated SiO₂ samples.

Table B.2: Comparison of different surface treatment techniques reported in literature. FGA sample without any surface treatment shows better results

Type of treatment	Contact Angle Measurement	Roughness	Mobility	V _{Dirac} shift	Hysteresis/ Instability in IV
H ₂ O sonication	75-80 [155]	-	-	+ve [155]	-
Acetone/IPA sonication	75 [155]	-	-	+ve [155]	-
O ₂ plasma	60 [155], ~ 0 [153] 36 (this work)	increases [153] increases (this work)	reduces [153] reduces (this work)	+ve [155], -ve [153] -ve (this work)	increases [153] increases (this work)
UV-Ozone	40 [155]	-	-	+ve [155]	-
Re-oxidation	42.6 [153]	reduces [153]	increases [153]	-ve [153]	reduces [153]
HMDS	-	-	increases [156]	-ve [156]	reduces [156]
FGA (this work)	72	-	increases	+ve	reduces
Ar Plasma (this work)	25	increases	reduces	-ve	increases

Argon plasma and oxygen plasma treatment of SiO₂ surface before graphene transfer results in the increase of hydrophilicity and roughness of SiO₂. There is a shift in CNP and instability in transfer characteristics of GFETs made on plasma treated SiO₂/Si substrate as compared to only forming gas annealed SiO₂.

Ar plasma treatment cleans the surface and doesn't affect the Si-SiO₂ bond configuration. But Ar atoms gets embedded into SiO₂/Si substrate as confirmed by XPS, which results in the increase of positive charges, and the defects created by Ar plasma acts as scattering centers.

Oxygen plasma treatment make the SiO₂ surface more rough and there is an increase in

the percentage of Si(-O)₄ and Si(-OH)_x, which acts as donors and electron traps which results in instability in I-V characteristics and decrease in mobility. Still there is a need to optimize the plasma parameters like power and time of exposure and compare it with the literature.

Appendix C

Mobility Extraction by FTM Method

From the I-V characteristics of the GFETs, the total resistance R_{total} is extracted from the slope of drain current (I_D) vs drain voltage (V_D) curve for different gate voltages (V_G). Mobility for GFETs are calculated by fitting the R_{total} vs V_G curve using the following relation.

$$R_{total} = R_{contact} + \frac{L}{W} \times \frac{1}{q \times \mu \times \sqrt{n_o^2 + \left\{ \frac{2(V_G - V_{Dirac})b + a^2 + a\sqrt{a^2 + 4(V_G - V_{Dirac})b}}{2b^2} \right\}^2}} \quad (C.1)$$

where

$R_{contact}$ = contact resistance (Ω)

μ = mobility ($\text{cm}^2/\text{V.s}$)

n_o = charge carrier density (cm^{-2})

V_G = gate voltage (V)

V_{Dirac} = gate voltage at Dirac point (V)

C_{ox} = oxide gate capacitance = 3.86×10^{-4} F m^{-2} for 90 nm thick oxide

q = charge (C)

V_{Fermi} = Fermi velocity (m s^{-1})

L = graphene channel length (μm)

W = graphene channel width (μm)

$$a = \frac{\hbar V_{Fermi} \sqrt{\pi}}{q} = \frac{\frac{1}{2\pi} \times 6.626 \times 10^{-34} \times 10^{-6} \times \pi}{1.6 \times 10^{-19}} = 1.168 \times 10^{-19} m^3 kg A^{-1} s^{-3} \quad (C.2)$$

$$b = \frac{q}{C_{ox}} = \frac{1.6 \times 10^{-19} C}{3.86 \times 10^{-4} F/m^2} = 4.17 \times 10^{-6} m^3 kg A^{-1} s^{-3} \quad (C.3)$$

As an example, R_{total} vs V_G curve was fitted for pristine graphene FET, when I-V is measured in air, is shown in figure C.1. Fitting gives hole mobility value of $\mu = 3833 \text{ cm}^2 \text{ V}^{-1} \text{ s}^{-1}$.

here goodness of fit are:-

The Sum of Square due to Error (SSE): 1.25e+04

R-square: 0.9999

Adjusted R-square: 0.9999

Root Mean Square Error (RMSE): 33.71

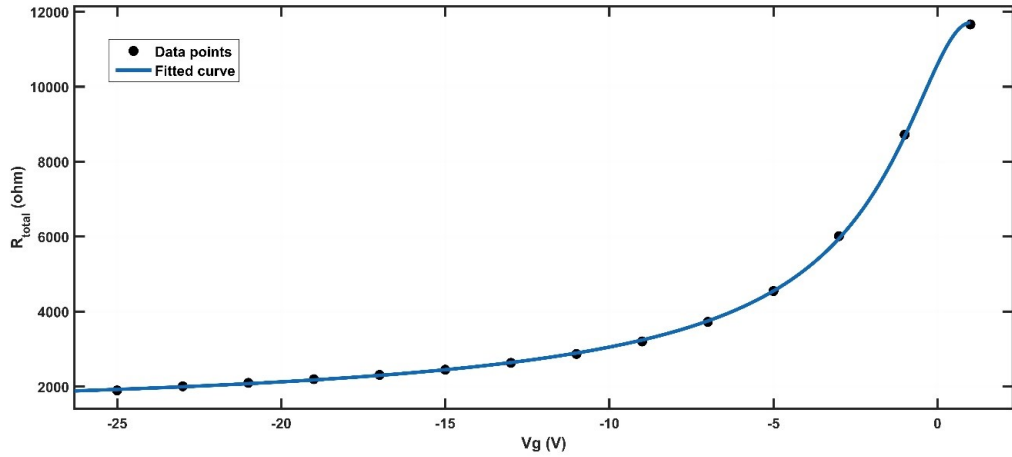


Figure C.1: R_{total} vs V_G curve fitted for pristine graphene FET, when I-V is measured in air.

References

- [1] K. S. Novoselov, A. K. Geim, S. V. Morozov, D. Jiang, Y. Zhang, S. V. Dubonos, I. V. Grigorieva, and A. A. Firsov, “Electric field effect in atomically thin carbon films,” *Science*, vol. 306, no. 5696, pp. 666–669, 2004. [Online]. Available: <https://doi.org/10.1126/science.1102896>
- [2] A. Geim and K. Novoselov, “The rise of graphene.” *Nature Materials*, vol. 6, pp. 183–191, 2007. [Online]. Available: <https://doi.org/10.1038/nmat1849>
- [3] S. Chen, L. Brown, M. Levendorf, W. Cai, S. Y. Ju, J. Edgeworth, X. Li, C. W. Magnuson, A. Velamakanni, R. D. Piner, J. Kang, J. Park, and R. S. Ruoff, “Oxidation resistance of graphene-coated Cu and Cu/Ni alloy,” *ACS Nano*, vol. 5, no. 2, pp. 1321–1327, 2011. [Online]. Available: <https://doi.org/10.1021/nn103028d>
- [4] M. Sepioni, R. R. Nair, S. Rablen, J. Narayanan, F. Tuna, R. Winpenny, A. K. Geim, and I. V. Grigorieva, “Limits on intrinsic magnetism in graphene,” *Physical Review Letters*, vol. 105, no. 20, pp. 1–4, 2010. [Online]. Available: <https://doi.org/10.1103/PhysRevLett.105.207205>
- [5] D. C. Elias, R. R. Nair, T. Mohiuddin, S. Morozov, P. Blake, M. Halsall, A. Ferrari, D. Boukhvalov, M. Katsnelson, A. Geim, and K. S. Novoselov, “Control of graphene’s properties by reversible hydrogenation: evidence for graphane,” *Science*, vol. 323, no. 5914, pp. 610–613, 2009. [Online]. Available: <https://doi.org/10.1126/science.1167130>

-
- [6] H. Liu, Y. Liu, and D. Zhu, “Chemical doping of graphene,” *Journal of Materials Chemistry*, vol. 21, no. 10, pp. 3335–3345, 2011. [Online]. Available: <https://doi.org/10.1039/C0JM02922J>
- [7] Y. Liu, Q. Feng, N. Tang, X. Wan, F. Liu, L. Lv, and Y. Du, “Increased magnetization of reduced graphene oxide by nitrogen-doping,” *Carbon*, vol. 60, pp. 549–551, 2013. [Online]. Available: <https://doi.org/10.1016/j.carbon.2013.03.060>
- [8] J. Zhu, H. Park, R. Podila, A. Wadehra, P. Ayala, L. Oliveira, J. He, A. A. Zakhidov, A. Howard, J. Wilkins, and A. M. Rao, “Magnetic properties of sulfur-doped graphene,” *Journal of Magnetism and Magnetic Materials*, vol. 401, pp. 70–76, 2016. [Online]. Available: <https://doi.org/10.1016/j.jmmm.2015.10.012>
- [9] L. Xie, X. Wang, J. Lu, Z. Ni, Z. Luo, H. Mao, R. Wang, Y. Wang, H. Huang, D. Qi, R. Liu, T. Yu, Z. Shen, T. Wu, H. Peng, B. Özyilmaz, K. Loh, A. T. Wee, Ariando, and W. Chen, “Room temperature ferromagnetism in partially hydrogenated epitaxial graphene,” *Applied Physics Letters*, vol. 98, no. 19, pp. 2009–2012, 2011. [Online]. Available: <https://doi.org/10.1063/1.3589970>
- [10] H. Liu, J. Gao, M. Xue, N. Zhu, M. Zhang, and T. Cao, “Processing of graphene for electrochemical application: Noncovalently functionalize graphene sheets with water-soluble electroactive methylene green,” *Langmuir*, vol. 25, no. 20, pp. 12 006–12 010, 2009. [Online]. Available: <https://doi.org/10.1021/la9029613>
- [11] R. R. Nair, W. Ren, R. Jalil, I. Riaz, V. G. Kravets, L. Britnell, P. Blake, F. Schedin, A. S. Mayorov, S. Yuan, M. I. Katsnelson, H. M. Cheng, W. Strupinski, L. G. Bulusheva, A. V. Okotrub, I. V. Grigorieva, A. N. Grigorenko, K. S. Novoselov, and A. K. Geim, “Fluorographene: A two-dimensional counterpart of Teflon,” *Small*, vol. 6, no. 24, pp. 2877–2884, 2010. [Online]. Available: <https://doi.org/10.1002/sml.201001555>
- [12] Y. C. Lin, C. Y. Lin, and P. W. Chiu, “Controllable graphene N-doping with ammonia plasma,” *Applied Physics Letters*, vol. 96, no. 13, 2010. [Online].

- Available: <https://doi.org/10.1063/1.3368697>
- [13] M. Baraket, S. G. Walton, E. H. Lock, J. T. Robinson, and F. K. Perkins, “The functionalization of graphene using electron-beam generated plasmas,” *Applied Physics Letters*, vol. 96, no. 23, pp. 10–12, 2010. [Online]. Available: <https://doi.org/10.1063/1.3436556>
- [14] A. Nourbakhsh, M. Cantoro, T. Vosch, G. Pourtois, F. Clemente, M. H. van der Veen, J. Hofkens, M. M. Heyns, S. D. Gendt, and B. F. Sels, “Bandgap opening in oxygen plasma-treated graphene,” *Nanotechnology*, vol. 21, no. 43, p. 435203, oct 2010. [Online]. Available: <https://doi.org/10.1088%2F0957-4484%2F21%2F43%2F435203>
- [15] B. Guo, Q. Liu, E. Chen, H. Zhu, L. Fang, and J. R. Gong, “Controllable N-doping of graphene,” *Nano Letters*, vol. 10, no. 12, pp. 4975–4980, 2010. [Online]. Available: <https://doi.org/10.1021/nl103079j>
- [16] A. H. C. Neto, F. Guinea, N. M. R. Peres, K. S. Novoselov, and A. K. Geim, “The electronic properties of graphene,” *Reviews of Modern Physics*, vol. 81, no. 1, p. 109, 2009. [Online]. Available: <https://doi.org/10.1103/RevModPhys.81.109>
- [17] A. Misra, “Novel floating gate materials for flash memory,” 2014. [Online]. Available: <http://www.ee.iitb.ac.in/~anilkg/Abhishek-Misra-thesis.pdf>.
- [18] A. Misra, H. Kalita, and A. Kottantharayil, “Work function modulation and thermal stability of reduced graphene oxide gate electrodes in MOS devices,” *ACS Applied Materials and Interfaces*, vol. 6, no. 2, pp. 786–794, 2014. [Online]. Available: <https://doi.org/10.1021/am404649a>
- [19] W. S. Hummers and R. E. Offeman, “Preparation of graphitic oxide,” *Journal of the American Chemical Society*, vol. 80, no. 6, pp. 1339–1339, 1958. [Online]. Available: <https://doi.org/10.1021/ja01539a017>
- [20] D. W. Boukhvalov and M. I. Katsnelson, “Chemical functionalization of graphene,”

- Journal of Physics: Condensed Matter*, vol. 21, pp. 344 205–16, 2009. [Online]. Available: <https://doi.org/10.1088/0953-8984/21/34/344205>
- [21] V. Georgakilas, M. Otyepka, A. B. Bourlinos, V. Chandra, N. Kim, K. C. Kemp, P. Hobza, R. Zboril, and K. S. Kim, “Functionalization of graphene: Covalent and non-covalent approaches, derivatives and applications,” *Chemical Reviews*, vol. 112, no. 11, pp. 6156–6214, 2012. [Online]. Available: <https://doi.org/10.1021/cr3000412>
- [22] A. C. Dillon and M. J. Heben, “Hydrogen storage using carbon adsorbents : past , present and future,” *Applied Physics A*, vol. 72, pp. 133–142, 2001. [Online]. Available: <https://doi.org/10.1007/s003390100788>
- [23] A. C. Dillon, K. M. Jones, T. A. Bekkedahl, C. H. Kiang, D. S. Bethune, and M. J. Heben, “Storage of hydrogen in single-walled carbon nanotubes,” *Nature*, vol. 386, no. 1995, pp. 377–379, 1997. [Online]. Available: <https://doi.org/10.1038/386377a0>
- [24] D. Soriano, N. Leconte, P. Ordejón, J. C. Charlier, J. J. Palacios, and S. Roche, “Magnetoresistance and magnetic ordering fingerprints in hydrogenated graphene,” *Physical Review Letters*, vol. 107, no. 1, pp. 1–4, 2011. [Online]. Available: <https://doi.org/10.1103/PhysRevLett.107.016602>
- [25] P. Mallet, M. Moaied, J. J. Palacios, F. Yndurain, C. Salgado, H. Gonzalez-Herrero, J. M. Gomez-Rodriguez, J.-Y. Veullen, I. Brihuega, and M. M. Ugeda, “Atomic-scale control of graphene magnetism by using hydrogen atoms,” *Science*, vol. 352, no. 6284, pp. 437–441, 2016. [Online]. Available: <https://doi.org/10.1126/science.aad8038>
- [26] H. Huang, Z. Li, J. She, and W. Wang, “Oxygen density dependent band gap of reduced graphene oxide,” *Journal of Applied Physics*, vol. 111, no. 5, p. 054317, 2012. [Online]. Available: <https://doi.org/10.1063/1.3694665>
- [27] M. Lundie, Z. Sljivancanin, and S. Tomic, “Electronic and optical properties of reduced graphene oxide,” *Journal of Materials Chemistry C*, vol. 3, no. 29, pp.

- 7632–7641, 2015. [Online]. Available: <https://doi.org/10.1039/c5tc00437c>
- [28] D. Li, M. B. Müller, S. Gilje, R. B. Kaner, and G. G. Wallace, “Processable aqueous dispersions of graphene nanosheets,” *Nature Nanotechnology*, vol. 3, no. 2, pp. 101–105, 2008. [Online]. Available: <https://doi.org/10.1038/nnano.2007.451>
- [29] C. H. Chuang, Y. F. Wang, Y. C. Shao, Y. C. Yeh, D. Y. Wang, C. W. Chen, J. W. Chiou, S. C. Ray, W. F. Pong, L. Zhang, J. F. Zhu, and J. H. Guo, “The effect of thermal reduction on the photoluminescence and electronic structures of graphene oxides,” *Scientific Reports*, vol. 4, pp. 1–7, 2014. [Online]. Available: <https://doi.org/10.1038/srep04525>
- [30] G. Eda, G. Fanchini, and M. Chhowalla, “Large-area ultrathin films of reduced graphene oxide as a transparent and flexible electronic material,” *Nature Nanotechnology*, vol. 3, no. 5, pp. 270–274, 2008. [Online]. Available: <https://doi.org/10.1038/nnano.2008.83>
- [31] V. Georgakilas, A. B. Bourlinos, R. Zboril, T. A. Steriotis, P. Dallas, A. K. Stubos, and C. Trapalis, “Organic functionalisation of graphenes,” *Chemical Communications*, vol. 46, no. 10, p. 1766, 2010. [Online]. Available: <https://doi.org/10.1039/b922081j>
- [32] M. Nasrollahzadeh, F. Babaei, P. Fakhri, and B. Jaleh, “Synthesis,, characterization structural, optical properties and catalytic activity of reduced graphene oxide/copper nanocomposites,” *RSC Advances*, vol. 5, pp. 10 782–10 789, 2015. [Online]. Available: <http://dx.doi.org/10.1039/C4RA12552E>
- [33] S. S. Varghese, S. Lonkar, K. K. Singh, S. Swaminathan, and A. Abdala, “Recent advances in graphene based gas sensors,” *Sensors and Actuators, B: Chemical*, vol. 218, pp. 160–183, 2015. [Online]. Available: <http://dx.doi.org/10.1016/j.snb.2015.04.062>
- [34] S. Basu and P. Bhattacharyya, “Recent developments on graphene and graphene

- oxide based solid state gas sensors,” *Sensors and Actuators, B: Chemical*, vol. 173, pp. 1–21, 2012. [Online]. Available: <http://dx.doi.org/10.1016/j.snb.2012.07.092>
- [35] K. Toda, R. Furue, and S. Hayami, “Recent progress in applications of graphene oxide for gas sensing: A review,” *Analytica Chimica Acta*, vol. 878, pp. 43–53, 2015. [Online]. Available: <http://dx.doi.org/10.1016/j.aca.2015.02.002>
- [36] H. J. Shin, K. K. Kim, A. Benayad, S. M. Yoon, H. K. Park, I. S. Jung, M. H. Jin, H. K. Jeong, J. M. Kim, J. Y. Choi, and Y. H. Lee, “Efficient reduction of graphite oxide by sodium borohydride and its effect on electrical conductance,” *Advanced Functional Materials*, vol. 19, no. 12, pp. 1987–1992, 2009. [Online]. Available: <https://doi.org/10.1002/adfm.200900167>
- [37] H. C. Schniepp, J. L. Li, M. J. McAllister, H. Sai, M. Herrera-Alonson, D. H. Adamson, R. K. Prud’homme, R. Car, D. A. Seville, and I. A. Aksay, “Functionalized single graphene sheets derived from splitting graphite oxide,” *Journal of Physical Chemistry B*, vol. 110, no. 17, pp. 8535–8539, 2006. [Online]. Available: <https://doi.org/10.1021/jp060936f>
- [38] S. Chen, W. Cai, R. D. Piner, J. W. Suk, Y. Wu, Y. Ren, J. Kang, and R. S. Ruoff, “Synthesis and characterization of large-area graphene and graphite films on commercial Cu-Ni alloy foils,” *Nano Letters*, vol. 11, no. 9, pp. 3519–3525, 2011. [Online]. Available: <http://dx.doi.org/10.1021/nl201699j>
- [39] J. T. Robinson, J. S. Burgess, C. E. Junkermeier, S. C. Badescu, T. L. Reinecke, F. K. Perkins, M. K. Zalalutdniov, J. W. Baldwin, J. C. Culbertson, P. E. Sheehan, and E. S. Snow, “Properties of fluorinated graphene films,” *Nano Letters*, vol. 10, no. 8, pp. 3001–3005, 2010. [Online]. Available: <https://doi.org/10.1021/nl101437p>
- [40] L. Yan, M. Lin, C. Zeng, Z. Chen, S. Zhang, X. Zhao, A. Wu, Y. Wang, L. Dai, J. Qu, M. Guo, and Y. Liu, “Electroactive and biocompatible hydroxyl-functionalized graphene by ball milling,” *Journal of Materials Chemistry*, vol. 22, no. 17, p. 8367, 2012. [Online]. Available: <https://doi.org/10.1039/c2jm30961k>

- [41] M. Lin, R. Zou, H. Shi, S. Yu, X. Li, R. Guo, L. Yan, G. Li, Y. Liu, and L. Dai, "Ocular biocompatibility evaluation of hydroxyl-functionalized graphene," *Materials Science and Engineering C*, vol. 50, pp. 300–308, 2015. [Online]. Available: <https://doi.org/10.1016/j.msec.2015.01.086>
- [42] W.-H. Zhang, P.-P. He, S. Wu, J. Xu, Y. Li, G. Zhang, and X.-Y. Wei, "Graphene oxide grafted hydroxyl-functionalized ionic liquid: A highly efficient catalyst for cycloaddition of CO₂ with epoxides," *Applied Catalysis A: General*, vol. 509, pp. 111–117, 2016. [Online]. Available: <https://doi.org/10.1016/j.apcata.2015.10.038>
- [43] D. Majumdar and S. Pal, "Hydroxyl-Functionalized Graphene : A Proficient Energy Storage Material," *Journal of Fundamentals of Renewable Energy Applications*, vol. 6, no. 3, 2016. [Online]. Available: <http://dx.doi.org/10.4172/20904541.1000209>
- [44] L. Wu, B. Zhang, H. Lu, and C.-Y. Liu, "Nanoscale ionic materials based on hydroxyl-functionalized graphene," *Journal of Material Chemistry A*, vol. 2, no. 5, pp. 1409–1417, 2014. [Online]. Available: <http://dx.doi.org/10.1039/C3TA14424K>
- [45] N. Ghaderi and M. Peressi, "First-principle study of hydroxyl functional groups on pristine, defected graphene, and graphene epoxide," *Journal of Physical Chemistry C*, vol. 114, no. 49, pp. 21 625–21 630, 2010. [Online]. Available: <https://doi.org/10.1021/jp108688m>
- [46] A. Sinitskii, A. Dimiev, D. a. Corley, A. a. Fursina, D. V. Kosynkin, and J. M. Tour, "Kinetics of diazonium functionalization of chemically converted graphene nanoribbons," *ACS Nano*, vol. 4, no. 4, pp. 1949–1954, 2010. [Online]. Available: <https://doi.org/10.1021/nn901899j>
- [47] a. J. M. Giesbers, U. Zeitler, S. Neubeck, F. Freitag, K. S. Novoselov, and J. C. Maan, "Nanolithography and manipulation of graphene using an atomic force microscope," *Solid State Communications*, vol. 147, no. 9-10, p. 11, 2008. [Online]. Available: <https://doi.org/10.1016/j.ssc.2008.06.027>

- [48] B. Ik-Su, Y. Duhee, C. Jin Sik, H. Inrok, H. L. Duk, L. Mi Jung, K. Tomoji, S. Young-Woo, J. Quanxi, C. Hyeonsik, and P. Bae Ho, “Nanoscale lithography on monolayer graphene using hydrogenation and oxidation,” *ACS Nano*, vol. 5, no. 8, pp. 6417–6424, 2011. [Online]. Available: <https://doi.org/10.1021/nn201601m>
- [49] A. C. Ferrari and D. M. Basko, “Raman spectroscopy as a versatile tool for studying the properties of graphene,” *Nature Nanotechnology*, vol. 8, no. 4, pp. 235–246, 2013. [Online]. Available: <https://doi.org/10.1038/nnano.2013.46>
- [50] A. C. Ferrari, “Raman spectroscopy of graphene and graphite: Disorder, electron-phonon coupling, doping and nonadiabatic effects,” *Solid State Communications*, vol. 143, no. 1-2, pp. 47–57, 2007. [Online]. Available: <https://doi.org/10.1016/j.ssc.2007.03.052>
- [51] J. H. Bong, O. Sul, A. Yoon, S.-Y. Choi, and B. J. Cho, “Facile graphene n-doping by wet chemical treatment for electronic applications.” *Nanoscale*, vol. 6, no. 15, pp. 8503–8, 2014. [Online]. Available: <https://doi.org/10.1039/c4nr01160k>
- [52] J. Wei, B. Liang, Q. Cao, H. Ren, Y. Zheng, and X. Ye, “Understanding asymmetric transfer characteristics and hysteresis behaviors in graphene devices under different chemical atmospheres,” *Carbon*, vol. 156, pp. 67–76, 2019. [Online]. Available: <https://doi.org/10.1016/j.carbon.2019.09.038>
- [53] H. Wang, T. Maiyalagan, and X. Wang, “Review on recent progress in nitrogen-doped graphene: Synthesis, characterization, and its potential applications,” *ACS Catalysis*, vol. 2, no. 5, pp. 781–794, 2012. [Online]. Available: <http://doi.org/10.1021/cs200652y>
- [54] J. Hutfles, C. Lumley, X. Chen, Z. Jason, and J. Pellegrino, “Graphene-integrated polymeric membrane as a flexible , multifunctional electrode,” *Chemical Engineering Science*, vol. 209, p. 115221, 2019. [Online]. Available: <http://dx.doi.org/10.1016/j.ces.2019.115221>

- [55] J. H. Jeong, G. W. Lee, Y. H. Kim, Y. J. Choi, K. C. Roh, and K. B. Kim, "A holey graphene-based hybrid supercapacitor," *Chemical Engineering Journal*, vol. 378, p. 122126, 2019. [Online]. Available: <http://dx.doi.org/10.1016/j.cej.2019.122126>
- [56] H. Cheng, X. Zhou, A. Gao, F. Yi, D. Shu, X. Song, R. Zeng, C. He, S. Li, and D. Zeng, "Supermolecule polymerization derived porous nitrogen-doped reduced graphene oxide as a high-performance electrode material for supercapacitors," *Electrochimica Acta*, vol. 292, pp. 20–30, 2018. [Online]. Available: <http://dx.doi.org/10.1016/j.electacta.2018.09.092>
- [57] S. Liu, Y. Wang, and Z. Ma, "Bi₂O₃ with reduced graphene oxide composite as a supercapacitor electrode," *International Journal of Electrochemical Science*, vol. 13, no. 12, pp. 12 256–12 265, 2018. [Online]. Available: <http://dx.doi.org/10.20964/2018.12.10>
- [58] Y. Jia, L. Zhou, and J. Shao, "Electrochemical performance of flexible graphene-based fibers as electrodes for wearable supercapacitors," *Synthetic Metals*, vol. 246, no. October, pp. 108–114, 2018. [Online]. Available: <http://dx.doi.org/10.1016/j.synthmet.2018.09.016>
- [59] E. V. Castro, K. S. Novoselov, S. V. Morozov, N. M. R. Peres, J. M. B. L. Santos, J. Nilsson, A. K. Geim, and A. H. C. Neto, "Biased bilayer graphene: Semiconductor with a gap tunable by the electric field effect," vol. 216802, no. November, pp. 8–11, 2007. [Online]. Available: <https://doi.org/10.1103/PhysRevLett.99.216802>
- [60] T. Ohta, A. Bostwick, T. Seyller, K. Horn, and E. Rotenberg, "Controlling the electronic structure of bilayer graphene," *Science*, vol. 313, no. 5789, pp. 951–954, 2006. [Online]. Available: <https://doi.org/10.1126/science.1130681>
- [61] W. Zhang, C. T. Lin, K. K. Liu, T. Tite, C. Y. Su, C. H. Chang, Y. H. Lee, C. W. Chu, K. H. Wei, J. L. Kuo, and L. J. Li, "Opening an electrical band gap of bilayer graphene with molecular doping," *ACS Nano*, vol. 5, no. 9, pp. 7517–7524, 2011. [Online]. Available: <https://doi.org/10.1021/nn202463g>

- [62] G. Zhao, C. Feng, H. Cheng, Y. Li, and Z.-s. Wang, “In situ thermal conversion of graphene oxide films to reduced graphene oxide films for efficient dye-sensitized solar cells,” *Materials Research Bulletin*, vol. 120, p. 110609, 2019. [Online]. Available: <http://dx.doi.org/10.1016/j.materresbull.2019.110609>
- [63] Y. Wang, M. Myers, and J. A. Staser, “Electrochemical UV sensor using carbon quantum dot/graphene semiconductor,” *Journal of the Electrochemical Society*, vol. 165, no. 4, pp. H3001–H3007, 2018. [Online]. Available: <http://doi.org/10.1149/2.0011804jes>
- [64] A. A. Mohammed, A. B. Suriani, and A. R. Jabur, “The Enhancement of UV sensor response by zinc oxide nanorods / reduced graphene oxide bilayer nanocomposites film,” *Journal of Physics: Conference Series*, vol. 1003, no. 1, 2018. [Online]. Available: <http://doi.org/10.1088/1742-6596/1003/1/012070>
- [65] T. V. Tam, S. H. Hur, J. S. Chung, and W. M. Choi, “Ultraviolet light sensor based on graphene quantum dots/reduced graphene oxide hybrid film,” *Sensors and Actuators A: Physical*, vol. 233, pp. 368–373, 2015. [Online]. Available: <http://doi.org/10.1016/j.sna.2015.07.038>
- [66] Z. Wang, X. Zhan, Y. Wang, S. Muhammad, Y. Huang, and J. He, “A flexible UV nanosensor based on reduced graphene oxide decorated ZnO nanostructures,” *Nanoscale*, vol. 4, no. 8, pp. 2678–2684, 2012. [Online]. Available: <http://doi.org/10.1039/c2nr30354j>
- [67] J. Wen, Y. Niu, P. Wang, M. Chen, W. Wu, Y. Cao, J. L. Sun, M. Zhao, D. Zhuang, and Y. Wang, “Ultra-broadband self-powered reduced graphene oxide photodetectors with annealing temperature-dependent responsivity,” *Carbon*, vol. 153, pp. 274–284, 2019. [Online]. Available: <https://doi.org/10.1016/j.carbon.2019.07.033>
- [68] Y. Liu, T. Gong, Y. Zheng, X. Wang, J. Xu, Q. Ai, J. Guo, W. Huang, S. Zhou, Z. Liu, Y. Lin, T. L. Ren, and B. Yu, “Ultra-sensitive and plasmon-tunable

- graphene photodetectors for micro-spectrometry,” *Nanoscale*, vol. 10, no. 42, pp. 20 013–20 019, 2018. [Online]. Available: <http://doi.org/10.1039/c8nr04996c>
- [69] M. U. Rahman, F. Xie, Y. Li, X. Sun, and M. Wei, “Grafting cobalt sulfide on graphene nanosheets as a counterelectrode for dye-sensitized solar cells,” *Journal of Alloys and Compounds*, vol. 808, p. 151701, 2019. [Online]. Available: <http://dx.doi.org/10.1016/j.jallcom.2019.151701>
- [70] T. Iqbal, M. Haqnawaz, M. Sultan, M. B. Tahir, M. I. Khan, K. N. Riaz, M. Ijaz, and M. Rafique, “Novel graphene-based transparent electrodes for perovskite solar cells,” *International Journal of Energy Research*, vol. 42, no. 15, pp. 4866–4874, 2018. [Online]. Available: <http://dx.doi.org/10.1002/er.4244>
- [71] M. Vaqueiro-Contreras, C. Bartlam, R. S. Bonilla, V. P. Markevich, M. P. Halsall, A. Vijayaraghavan, and A. R. Peaker, “Graphene oxide films for field effect surface passivation of silicon for solar cells,” *Solar Energy Materials and Solar Cells*, vol. 187, pp. 189–193, 2018. [Online]. Available: <http://dx.doi.org/10.1016/j.solmat.2018.08.002>
- [72] E. Kan, Z. Li, and J. Yang, “Magnetism in graphene systems,” *Nano*, vol. 03, no. 06, pp. 433–442, 2008. [Online]. Available: <https://doi.org/10.1142/S1793292008001350>
- [73] A. L. Sharpe, E. J. Fox, A. W. Barnard, J. Finney, K. Watanabe, T. Taniguchi, M. A. Kastner, and D. Goldhaber-gordon, “Emergent ferromagnetism near three-quarters filling in twisted bilayer graphene,” *Science*, vol. 608, no. 6453, pp. 605–608, 2019. [Online]. Available: <https://doi.org/10.1126/science.aaw3780>
- [74] X. Zhang, Y. Sun, W. Gao, Y. Lin, X. Zhao, Q. Wang, X. Yao, M. He, X. Ye, and Y. Liu, “Sizable bandgaps of graphene in 3d transition metal intercalated defective graphene/WSe₂ heterostructures,” *RSC Advances*, vol. 9, no. 32, pp. 18 157–18 164, 2019. [Online]. Available: <https://doi.org/10.1039/c9ra03034d>
- [75] T. Wakamura, F. Reale, P. Palczynski, M. Q. Zhao, A. T. C. Johnson, S. Guéron,

- C. Mattevi, A. Ouerghi, and H. Bouchiat, “Spin-orbit interaction induced in graphene by transition metal dichalcogenides,” *Physical Review B*, vol. 99, p. 245402, Jun 2019. [Online]. Available: <https://doi.org/10.1103/PhysRevB.99.245402>
- [76] J. H. Garcia, M. Vila, A. W. Cummings, and S. Roche, “Spin transport in graphene/transition metal dichalcogenide heterostructures,” *Chemical Society Reviews*, vol. 47, no. 9, pp. 3359–3379, 2018. [Online]. Available: <https://doi.org/10.1039/c7cs00864c>
- [77] Y. K. Luo, J. Xu, T. Zhu, G. Wu, E. J. McCormick, W. Zhan, M. R. Neupane, and R. K. Kawakami, “Opto-valleytronic spin injection in monolayer MoS₂ /few-Layer graphene hybrid spin valves,” *Nano Letters*, vol. 17, no. 6, pp. 3877–3883, 2017. [Online]. Available: <https://doi.org/10.1021/acs.nanolett.7b01393>
- [78] J. W. McClure, “Diamagnetism of graphite,” *Physical Review*, vol. 104, pp. 666–671, Nov 1956. [Online]. Available: <https://doi.org/10.1103/PhysRev.104.666>
- [79] V. M. Pereira, F. Guinea, J. M. B. Lopes Dos Santos, N. M. R. Peres, and A. H. Castro Neto, “Disorder induced localized states in graphene,” *Physical Review Letters*, vol. 96, no. 3, pp. 27–30, 2006. [Online]. Available: <https://doi.org/10.1103/PhysRevLett.96.036801>
- [80] Y. Wang, Y. Hoang, Y. Song, X. Zhang, Y. Ma, J. Liang, and Y. Chen, “Room-temperature ferromagnetism of graphene,” *Nano Letters*, vol. 9, no. 1, pp. 220–224, 2009. [Online]. Available: <https://doi.org/10.1021/nl802810g>
- [81] O. V. Yazyev and L. Helm, “Defect-induced magnetism in graphene,” *Physical Review B: Condensed Matter and Materials Physics*, vol. 75, no. 12, pp. 1–5, 2007. [Online]. Available: <https://doi.org/10.1103/PhysRevB.75.125408>
- [82] Y. Ma, P. O. Lehtinen, A. S. Foster, and R. M. Nieminen, “Magnetic properties of vacancies in graphene and single-walled carbon nanotubes,” *New Journal of Physics*, vol. 6, pp. 1–15, 2004. [Online]. Available:

- <https://doi.org/10.1088/1367-2630/6/1/068>
- [83] G. Khurana, N. Kumar, R. K. Kotnala, T. Nautiyal, and R. S. Katiyar, “Temperature tuned defect induced magnetism in reduced graphene oxide,” *Nanoscale*, vol. 5, no. 8, pp. 3346–3351, 2013. [Online]. Available: <https://doi.org/10.1039/c3nr34291c>
- [84] S. Biswal, D. S. Bhaskaram, and G. Govindaraj, “Graphene oxide: Structure and temperature dependent magnetic characterization,” *Materials Research Express*, vol. 5, no. 8, 2018. [Online]. Available: <https://doi.org/10.1088/2053-1591/aad1cf>
- [85] S. Sarma, S. C. Ray, and A. M. Strydom, “Electronic and magnetic properties of nitrogen functionalized graphene-oxide,” *Diamond and Related Materials*, vol. 79, no. August, pp. 1–6, 2017. [Online]. Available: <https://doi.org/10.1016/j.diamond.2017.08.011>
- [86] Y. Liu, N. Tang, X. Wan, Q. Feng, M. Li, Q. Xu, F. Liu, and Y. Du, “Realization of ferromagnetic graphene oxide with high magnetization by doping graphene oxide with nitrogen,” *Scientific Reports*, vol. 3, 2013. [Online]. Available: <https://doi.org/10.1038/srep02566>
- [87] P. Błoński, J. Tuček, Z. Sofer, V. Mazánek, M. Petr, M. Pumera, M. Otyepka, and R. Zbořil, “Doping with graphitic nitrogen triggers ferromagnetism in graphene,” *Journal of the American Chemical Society*, vol. 139, no. 8, pp. 3171–3180, 2017. [Online]. Available: <https://doi.org/10.1021/jacs.6b12934>
- [88] Q. Miao, L. Wang, Z. Liu, B. Wei, F. Xu, and W. Fei, “Magnetic properties of N-doped graphene with high Curie temperature,” *Scientific Reports*, vol. 6, no. February, pp. 1–10, 2016. [Online]. Available: <https://doi.org/10.1038/srep21832>
- [89] N. Zhang, I. Geronimo, P. Paneth, J. Schindelka, T. Schaefer, H. Herrmann, C. Vogt, and H. H. Richnow, “Analyzing sites of OH radical attack (ring vs. side chain) in oxidation of substituted benzenes via dual stable isotope analysis (δ^{13}

- C and δ^2 H),” *Science of the Total Environment*, vol. 542, pp. 484–494, 2016. [Online]. Available: <https://doi.org/10.1016/j.scitotenv.2015.10.075>
- [90] S. Qin, X. Guo, Y. Cao, Z. Ni, and Q. Xu, “Strong ferromagnetism of reduced graphene oxide,” *Carbon*, vol. 78, pp. 559–565, 2014. [Online]. Available: <https://doi.org/10.1016/j.carbon.2014.07.039>
- [91] E. H. Lieb, “Two Theorems on the Hubbard Model,” *Physical Review Letters*, vol. 62, no. 10, pp. 1201–1204, 1989. [Online]. Available: <https://doi.org/10.1103/PhysRevLett.62.1201>
- [92] J. J. Palacios and F. Ynduráin, “A critical analysis of vacancy-induced magnetism in monolayer and bilayer graphene,” *Physical Review B: Condensed Matter and Materials Physics*, vol. 85, no. 24, pp. 0–8, 2012. [Online]. Available: <https://doi.org/10.1103/PhysRevB.85.245443>
- [93] S.-W. Wang, H. E. Lin, H.-D. Lin, K. Y. Chen, K.-H. Tu, C. W. Chen, J.-Y. Chen, C.-H. Liu, C.-T. Liang, and Y. F. Chen, “Transport behavior and negative magnetoresistance in chemically reduced graphene oxide nanofilms,” *Nanotechnology*, vol. 22, no. 33, p. 335701, jul 2011. [Online]. Available: <https://doi.org/10.1088/0957-4484/22/33/335701>
- [94] J. Bai, R. Cheng, F. Xiu, L. Liao, M. Wang, A. Shailos, K. L. Wang, Y. Huang, and X. Duan, “Very large magnetoresistance in graphene nanoribbons,” *Nature Nanotechnology*, vol. 5, no. 9, pp. 655–659, 2010. [Online]. Available: <https://doi.org/10.1038/nnano.2010.154>
- [95] S. Bala Kumar and J. Guo, “Modelling very large magnetoresistance of graphene nanoribbon devices,” *Nanoscale*, vol. 4, no. 3, pp. 982–985, 2012. [Online]. Available: <https://doi.org/10.1039/c2nr11507g>
- [96] Y. Liu, R. Yang, H. Yang, D. Wang, Q. Zhan, G. Zhang, Y. Xie, B. Chen, and R.-W. Li, “Anomalous anisotropic magnetoresistance effects in

- graphene,” *AIP Advances*, vol. 4, no. 9, p. 097101, 2014. [Online]. Available: <https://doi.org/10.1063/1.4894519>
- [97] X. Wang, X. Li, L. Zhang, Y. Yoon, P. K. Weber, H. Wang, J. Guo, and H. Dai, “N-doping of graphene through electrothermal reactions with ammonia,” *Science*, vol. 324, no. 5928, pp. 768–771, 2009. [Online]. Available: <https://doi.org/10.1126/science.1170335>
- [98] Y. Shi, W. Zhu, H. Shi, F. Liao, Z. Fan, and M. Shao, “Mesocrystal PtRu supported on reduced graphene oxide as catalysts for methanol oxidation reaction,” *Journal of Colloid And Interface Science*, vol. 557, pp. 729–736, 2019. [Online]. Available: <http://dx.doi.org/10.1016/j.jcis.2019.09.038>
- [99] S. Na, B. Lee, W. Young, T. Yim, and S. Hyoung, “Lead ruthenate nanocrystals on reduced graphene oxides as an efficient bifunctional catalyst for metal – air batteries,” *Journal of Industrial and Engineering Chemistry*, vol. 79, pp. 409–417, 2019. [Online]. Available: <http://dx.doi.org/10.1016/j.jiec.2019.07.015>
- [100] D. Higgins, Z. Chen, D. U. Lee, and Z. Chen, “Activated and nitrogen-doped exfoliated graphene as air electrodes for metal–air battery applications,” *Journal of Materials Chemistry A*, vol. 1, pp. 2639–2645, 2013. [Online]. Available: <http://dx.doi.org/10.1039/c2ta00944g>
- [101] J. T. Catal, S. P. Lonkar, and A. A. Abdala, “Applications of Graphene in Catalysis,” *Journal of Thermodynamics and Catalysis*, vol. 5, no. 2, pp. 5–2, 2014. [Online]. Available: <http://dx.doi.org/10.4172/2157-7544.1000132>
- [102] S. Gupta Chatterjee, S. Chatterjee, A. K. Ray, and A. K. Chakraborty, “Graphene-metal oxide nanohybrids for toxic gas sensor: A review,” *Sensors and Actuators B: Chemical*, vol. 221, no. 2, pp. 1170–1181, 2015. [Online]. Available: <http://dx.doi.org/10.1016/j.snb.2015.07.070>
- [103] G. Ko, H. Y. Kim, J. Ahn, Y. M. Park, K. Y. Lee, and J. Kim, “Graphene-based

- nitrogen dioxide gas sensors,” *Current Applied Physics*, vol. 10, no. 4, pp. 1002–1004, 2010. [Online]. Available: <http://dx.doi.org/10.1016/j.cap.2009.12.024>
- [104] M. Gautam and A. H. Jayatissa, “Adsorption kinetics of ammonia sensing by graphene films decorated with platinum nanoparticles,” *Journal of Applied Physics*, vol. 111, no. 9, 2012. [Online]. Available: <http://dx.doi.org/10.1063/1.4714552>
- [105] K. C. Lam, B. Huang, and S. Q. Shi, “Room-temperature methane gas sensing properties based on in situ reduced graphene oxide incorporated with tin dioxide,” *Journal of Materials Chemistry A*, vol. 5, no. 22, pp. 11 131–11 142, 2017. [Online]. Available: <https://doi.org/10.1039/c7ta01293d>
- [106] N. H. Ha, C. T. Long, N. H. Nam, N. T. Hue, N. H. Phuong, and H. S. Hong, “Characteristics of hydrogen sensor based on monolayer of Pt nanoparticles decorated on single-layer graphene,” *Journal of Electronic Materials*, vol. 46, no. 6, pp. 3353–3358, 2017. [Online]. Available: <http://dx.doi.org/10.1007/s11664-016-5214-x>
- [107] C. M. Yang, T. C. Chen, Y. C. Yang, M. Meyyappan, and C. S. Lai, “Enhanced acetone sensing properties of monolayer graphene at room temperature by electrode spacing effect and UV illumination,” *Sensors and Actuators B: Chemical*, vol. 253, pp. 77–84, 2017. [Online]. Available: <http://dx.doi.org/10.1016/j.snb.2017.06.116>
- [108] X. Tang, N. Mager, B. Vanhorenbeke, S. Hermans, and J. P. Raskin, “Defect-free functionalized graphene sensor for formaldehyde detection,” *Nanotechnology*, vol. 28, no. 5, 2017. [Online]. Available: <http://dx.doi.org/10.1088/1361-6528/28/5/055501>
- [109] X. Gan, C. Zhao, Q. Yuan, L. Fang, Y. Li, J. Yin, X. Ma, and J. Zhao, “High performance graphene oxide-based humidity sensor integrated on a photonic crystal cavity,” *Applied Physics Letters*, vol. 110, no. 15, 2017. [Online]. Available: <http://doi.org/10.1063/1.4980045>

-
- [110] B. Melai, P. Salvo, N. Calisi, L. Moni, A. Bonini, C. Paoletti, T. Lomonaco, V. Mollica, R. Fuoco, and F. Di Francesco, “A graphene oxide pH sensor for wound monitoring,” *Proceedings of the Annual International Conference of the IEEE Engineering in Medicine and Biology Society, EMBS*, pp. 1898–1901, 2016. [Online]. Available: <https://doi.org/10.1109/EMBC.2016.7591092>
- [111] I. Y. Sohn, D. J. Kim, J. H. Jung, O. J. Yoon, T. Nguyen Thanh, T. Tran Quang, and N. E. Lee, “pH sensing characteristics and biosensing application of solution-gated reduced graphene oxide field-effect transistors,” *Biosensors and Bioelectronics*, vol. 45, no. 1, pp. 70–76, 2013. [Online]. Available: <http://dx.doi.org/10.1016/j.bios.2013.01.051>
- [112] C. Nie, L. Ma, S. Li, X. Fan, Y. Yang, C. Cheng, W. Zhao, and C. Zhao, “Recent progresses in graphene based bio-functional nanostructures for advanced biological and cellular interfaces,” *Nano Today*, vol. 26, pp. 57–97, 2019. [Online]. Available: <https://doi.org/10.1016/j.nantod.2019.03.003>
- [113] G. Potsi, A. B. Bourlinos, V. Mouselimis, K. Poláková, N. Chalmpes, D. Gournis, S. Kalytchuk, O. Tomanec, P. Błoński, M. Medveď, P. Lazar, M. Otyepka, and R. Zbořil, “Intrinsic photoluminescence of amine-functionalized graphene derivatives for bioimaging applications,” *Applied Materials Today*, vol. 17, pp. 112–122, 2019. [Online]. Available: <http://doi.org/10.1016/j.apmt.2019.08.002>
- [114] T. N. Ly and S. Park, “Highly sensitive ammonia sensor for diagnostic purpose using reduced graphene oxide and conductive polymer,” *Scientific Reports*, vol. 8, no. 1, pp. 1–12, 2018. [Online]. Available: <http://dx.doi.org/10.1038/s41598-018-36468-z>
- [115] C. Chung, Y. K. Kim, D. Shin, S. R. Ryoo, B. H. Hong, and D. H. Min, “Biomedical applications of graphene and graphene oxide,” *Accounts of Chemical Research*, vol. 46, no. 10, pp. 2211–2224, 2013. [Online]. Available: <http://dx.doi.org/10.1021/ar300159f>
- [116] E. Morales-Narváez and A. Merkoçi, “Graphene oxide as an optical biosensing

- platform: A progress report,” *Advanced Materials*, vol. 31, no. 6, pp. 1–12, 2019. [Online]. Available: <http://doi.org/10.1002/adma.201805043>
- [117] S. Pan, Z. Qi, Q. Li, Y. Ma, C. Fu, S. Zheng, W. Kong, Q. Liu, and X. Yang, “Graphene oxide-PLGA hybrid nanofibres for the local delivery of IGF-1 and BDNF in spinal cord repair,” *Artificial Cells, Nanomedicine and Biotechnology*, vol. 47, no. 1, pp. 651–664, 2019. [Online]. Available: <https://doi.org/10.1080/21691401.2019.1575843>
- [118] A. Kurniawan, S. Muneekaew, C. W. Hung, S. H. Chou, and M. J. Wang, “Modulated transdermal delivery of nonsteroidal anti-inflammatory drug by macroporous poly(vinyl alcohol)-graphene oxide nanocomposite films,” *International Journal of Pharmaceutics*, vol. 566, no. June, pp. 708–716, 2019. [Online]. Available: <http://dx.doi.org/10.1016/j.ijpharm.2019.06.029>
- [119] M. Kazempour, H. Namazi, A. Akbarzadeh, and R. Kabiri, “Synthesis and characterization of PEG-functionalized graphene oxide as an effective pH-sensitive drug carrier,” *Artificial Cells, Nanomedicine and Biotechnology*, vol. 47, no. 1, pp. 90–94, 2019. [Online]. Available: <https://doi.org/10.1080/21691401.2018.1543196>
- [120] R. Singla, T. Warang, and A. Kottantharayil, “Functionalization of graphene,” *Indian Patent*, no. 322817, October 2019.
- [121] R. Singla and A. Kottantharayil, “Method providing hydroxylation of graphene,” *Indian Patent*, May 2019, application number - 201921018594.
- [122] W. Fang, A. L. Hsu, R. Caudillo, Y. Song, a. G. Birdwell, E. Zakar, M. Kalbac, M. Dubey, T. Palacios, M. S. Dresselhaus, P. T. Araujo, and J. Kong, “Rapid identification of stacking orientation in isotopically labeled chemical-vapor grown bilayer graphene by Raman spectroscopy,” *Nano Letters*, vol. 13, pp. 1541–1548, 2013. [Online]. Available: <https://doi.org/10.1021/nl304706j>
- [123] G. Gao, D. Liu, S. Tang, C. Huang, M. He, Y. Guo, X. Sun, and B. Gao,

- “Heat-initiated chemical functionalization of graphene,” *Scientific Reports*, vol. 6, p. 20034, 2016. [Online]. Available: <https://doi.org/10.1038/srep20034>
- [124] R. Hawaldar, P. Merino, M. R. Correia, I. Bdikin, J. Gracio, J. Mendez, J. a. Martin-Gago, and M. K. Singh, “Large-area high-throughput synthesis of monolayer graphene sheet by hot filament thermal chemical vapor deposition,” *Scientific Reports*, vol. 2, p. 682, 2012. [Online]. Available: <https://doi.org/10.1038/srep00682>
- [125] A. P. Pijpers, K. Berresheim, and M. Wilmers, “Charge compensation for XPS on polymers,” *Fresenius’ Journal of Analytical Chemistry*, vol. 346, no. 1-3, pp. 104–109, 1993. [Online]. Available: <https://doi.org/10.1007/BF00321392>
- [126] A. C. Ferrari and J. Robertson, “Interpretation of Raman spectra of disordrred and amorphous carbon,” *Physical Review B*, vol. 61, no. 20, p. 14 295, 2000. [Online]. Available: <https://doi.org/10.1103/PhysRevB.61.14095>
- [127] A. Eckmann, A. Felten, A. Mishchenko, L. Britnell, R. Krupke, K. S. Novoselov, and C. Casiraghi, “Probing the nature of defects in graphene by Raman spectroscopy,” *Nano Letters*, vol. 12, no. 8, pp. 3925–3930, 2012. [Online]. Available: <https://doi.org/10.1021/nl300901a>
- [128] R. D. Bach, P. Y. Ayala, and H. B. Schlegel, “A reassessment of the bond dissociation energies of peroxides. An ab initio study,” *Journal of American Chemical Society*, vol. 118, no. 3, pp. 12 758–12 765, 1996. [Online]. Available: <https://doi.org/10.1021/ja961838i>
- [129] G. Glockler and G. Matlack, “The O–O bond energy in hydrogen peroxide,” *The Journal of Chemical Physics*, no. 8, pp. 504–505. [Online]. Available: <https://doi.org/10.1063/1.1724182>
- [130] D. Nelson and M. Cox, *Lehninger Principles of Biochemistry: 6th Edition*. Macmillan Learning, 2012. [Online]. Available: <https://books.google.co.in/books?id=n9e1NAEACAAJ>

- [131] P. V. Kumar, M. Bernardi, and J. C. Grossman, “The impact of functionalization on the stability, work function, and photoluminescence of reduced graphene oxide,” *ACS Nano*, vol. 7, no. 2, pp. 1638–1645, 2013. [Online]. Available: <https://doi.org/10.1021/nn305507p>
- [132] R. H. J. Vervuurt, B. Karasulu, M. A. Verheijen, W. E. M. M. Kessels, and A. A. Bol, “Uniform atomic layer deposition of Al_2O_3 on graphene by reversible hydrogen plasma functionalization,” *Chemistry of Materials*, vol. 29, no. 5, pp. 2090–2100, 2017. [Online]. Available: <http://dx.doi.org/10.1021/acs.chemmater.6b04368>
- [133] Image reversal resists and their processing, microchemical website. [Online]. Available: https://www.microchemicals.com/products/photoresists/az_5214_e.html
- [134] J. H. Chen, C. Jang, S. Adam, M. S. Fuhrer, E. D. Williams, and M. Ishigami, “Charged-impurity scattering in graphene,” *Nature Physics*, vol. 4, no. 5, pp. 377–381, 2008. [Online]. Available: <https://doi.org/10.1038/nphys935>
- [135] S. Adam, E. H. Hwang, V. M. Galitski, and S. Das Sarma, “A self-consistent theory for graphene transport,” *Proceedings of the National Academy of Sciences*, vol. 104, no. 47, pp. 18 392–18 397, 2007. [Online]. Available: <https://doi.org/10.1073/pnas.0704772104>
- [136] S. Kim, J. Nah, I. Jo, D. Shahrjerdi, L. Colombo, Z. Yao, E. Tutuc, and S. K. Banerjee, “Realization of a high mobility dual-gated graphene field-effect transistor with Al_2O_3 dielectric,” *Applied Physics Letters*, vol. 94, no. 6, p. 062107, 2009. [Online]. Available: <https://doi.org/10.1063/1.3077021>
- [137] B. Chen, H. Huang, X. Ma, L. Huang, Z. Zhang, and L.-m. Peng, “How good can CVD-grown monolayer graphene be?” *Nanoscale*, vol. 6, pp. 15 255–15 261, 2014. [Online]. Available: <https://doi.org/10.1039/c4nr05664g>
- [138] D. H. Tien, J. Y. Park, K. B. Kim, N. Lee, and Y. Seo, “Characterization of graphene-based FET fabricated using a shadow mask,” *Scientific Reports*,

- vol. 6, no. December 2015, pp. 1–8, 2016. [Online]. Available: <https://doi.org/10.1038/srep25050>
- [139] R. Somphonsane, H. Ramamoorthy, G. He, J. Nathawat, and C. Kwan, “Evaluating the sources of graphene’s resistivity using differential conductance,” *Scientific Reports*, no. 10317, pp. 1–11, 2017. [Online]. Available: <https://doi.org/10.1038/s41598-017-10367-1>
- [140] B. Krishna Bharadwaj, D. Nath, R. Pratap, and S. Raghavan, “Making consistent contacts to graphene: Effect of architecture and growth induced defects,” *Nanotechnology*, vol. 27, no. 20, 2016. [Online]. Available: <https://doi.org/10.1088/0957-4484/27/20/205705>
- [141] A. Meersha, H. B. Variar, K. Bhardwaj, A. Mishra, S. Raghavan, N. Bhat, and M. Shrivastava, “Record low metal - (CVD) graphene contact resistance using atomic orbital overlap engineering,” *Technical Digest - International Electron Devices Meeting, IEDM*, pp. 5.3.1–5.3.4, 2017. [Online]. Available: <https://doi.org/10.1109/IEDM.2016.7838352>
- [142] M. Li, N. Tang, W. Ren, H. Cheng, W. Wu, W. Zhong, and Y. Du, “Quenching of fluorescence of reduced graphene oxide by nitrogen-doping,” *Applied Physics Letters*, vol. 100, no. 23, pp. 1–4, 2012. [Online]. Available: <https://doi.org/10.1063/1.4726040>
- [143] M. Wu, C. Cao, and J. Z. Jiang, “Light non-metallic atom B, N, O and F-doped graphene: a first-principles study,” *Nanotechnology*, vol. 21, no. 50, p. 505202, nov 2010. [Online]. Available: <https://doi.org/10.1088/0957-4484/21/50/505202>
- [144] Y. Li, Z. Zhou, P. Shen, and Z. Chen, “Spin gapless semiconductor-metal-half-metal properties in nitrogen-doped zigzag graphene nanoribbons,” *ACS Nano*, vol. 3, no. 7, pp. 1952–1958, 2009. [Online]. Available: <https://doi.org/10.1021/nn9003428>

-
- [145] J. J. Chen, H. C. Wu, D. P. Yu, and Z. M. Liao, “Magnetic moments in graphene with vacancies,” *Nanoscale*, vol. 6, no. 15, pp. 8814–8821, 2014. [Online]. Available: <https://doi.org/10.1039/c3nr06892g>
- [146] S. M. Mortazavi Zanjani, M. M. Sadeghi, M. Holt, S. F. Chowdhury, L. Tao, and D. Akinwande, “Enhanced sensitivity of graphene ammonia gas sensors using molecular doping,” *Applied Physics Letters*, vol. 108, no. 3, pp. 1–6, 2016. [Online]. Available: <https://doi.org/10.1063/1.4940128>
- [147] S. Zhu, H. Sun, X. Liu, J. Zhuang, and L. Zhao, “Room-temperature NH₃ sensing of graphene oxide film and its enhanced response on the laser-Textured silicon,” *Scientific Reports*, vol. 7, no. 1, pp. 1–8, 2017. [Online]. Available: <http://doi.org/10.1038/s41598-017-15270-3>
- [148] IIT Bombay nanofabrication facilities website. [Online]. Available: <http://iitbnf.iitb.ac.in/iitbnf/index.php/infrastructure?layout=edit&id=18>
- [149] SAIF IIT bombay website. [Online]. Available: <http://http://www.saif.iitb.ac.in/>
- [150] Quantun design website. [Online]. Available: <https://www.qdusa.com/products/ppms.html>
- [151] A. Boscá, J. Pedrós, J. Martínez, T. Palacios, and F. Calle, “Automatic graphene transfer system for improved material quality and efficiency.” *Scientific Reports*, vol. 6, no. October 2015, p. 21676, 2016. [Online]. Available: <https://doi.org/10.1038/srep21676>
- [152] X. S. Li, Y. W. Zhu, W. W. Cai, M. Borysiak, B. Y. Han, D. Chen, R. D. Piner, L. Colombo, and R. S. Ruoff, “Transfer of large-area graphene films for high-performance transparent conductive electrodes,” *Nano Letters*, vol. 9, no. 12, pp. 4359–4363, 2009. [Online]. Available: <https://doi.org/10.1021/nl902623y>
- [153] K. Nagashio, T. Yamashita, T. Nishimura, K. Kita, and A. Toriumi, “Electrical transport properties of graphene on SiO₂ with specific surface structures,”

- Journal of Applied Physics*, vol. 110, no. 2, 2011. [Online]. Available: <https://doi.org/10.1063/1.3611394>
- [154] X. Liang, B. A. Sperling, I. Calizo, G. Cheng, C. A. Hacker, Q. Zhang, Y. Obeng, K. Yan, H. Peng, Q. Li, X. Zhu, H. Yuan, A. R. Hight Walker, Z. Liu, L. M. Peng, and C. A. Richter, “Toward clean and crackless transfer of graphene,” *ACS Nano*, vol. 5, no. 11, pp. 9144–9153, 2011. [Online]. Available: <https://doi.org/10.1021/nn203377t>
- [155] S. Goniszewski, M. Adabi, O. Shaforost, S. M. Hanham, L. Hao, and N. Klein, “Correlation of p-doping in CVD graphene with substrate surface charges,” *Scientific Reports*, vol. 6, no. March, p. 22858, 2016. [Online]. Available: <https://doi.org/10.1038/srep22858>
- [156] M. Lafkioti, B. Krauss, T. Lohmann, U. Zschieschang, H. Klauk, K. V. Klitzing, and J. H. Smet, “Graphene on a hydrophobic substrate: Doping reduction and hysteresis suppression under ambient conditions,” *Nano Letters*, vol. 10, no. 4, pp. 1149–1153, 2010. [Online]. Available: <https://doi.org/10.1021/nl903162a>
- [157] Y. T. Yeow, D. R. Lamb, and S. D. Brotherton, “An investigation of the influence of low-temperature annealing treatments on the interface state density at the si-sio₂,” *Journal of Physics D: Applied Physics*, vol. 8, no. 13, pp. 1495–1506, sep 1975. [Online]. Available: <https://doi.org/10.1088%2F0022-3727%2F8%2F13%2F011>
- [158] J. Kassabov, E. Atanassova, and D. Dimitrov, “Argon plasma treatment effects structures on Si-SiO₂ structures,” *Solid-State Electronics*, vol. 31, no. 2, pp. 147–154, 1988. [Online]. Available: [https://doi.org/10.1016/0038-1101\(88\)90122-0](https://doi.org/10.1016/0038-1101(88)90122-0)
- [159] A. U. Alam, M. M. R. Howlader, and M. J. Deen, “Oxygen plasma and humidity dependent surface analysis of silicon, silicon dioxide and glass for direct wafer bonding,” *ECS Journal of Solid State Science and Technology*, vol. 2, no. 12, pp. P515–P523, 2013. [Online]. Available: <https://doi.org/10.1149/2.007312jss>

- [160] A. Szekeres, S. Alexandrova, and K. Kirov, “The effect of O₂ plasma on properties of the *Si – SiO₂* system,” *Physica Status Solidi (A)*, vol. 62, no. 2, pp. 727–736, 1980. [Online]. Available: <https://doi.org/10.1002/pssa.2210620247>

Publications From The Thesis

Journal Publications:

1. **Robin Singla**, and Anil Kottantharayil, “*Stable hydroxyl functionalization and p-type doping of graphene by a non-destructive photo-chemical method*”, **Carbon**, 152, 267-273, 2019.
2. **Robin Singla**, Ambika Shankar Shukla, and Anil Kottantharayil, “*Introducing Ferromagnetism and Anisotropic Magnetoresistance in Monolayer CVD Graphene*”
Under review in **Carbon**.

Patents:

1. **Robin Singla**, Trupti Warang and Anil Kottantharayil, “*Functionalization of graphene*”,
Patent number 322817. **Indian Patent**, granted on 15 October 2019.
2. **Robin Singla**, and Anil Kottantharayil, “*Method providing hydroxylation of graphene*”,
Application number - 201921018594 **Indian Patent**, 2019.
3. **Robin Singla**, and Anil Kottantharayil, “*Method Providing Nitrogen Doping and Introducing Magnetization in CVD Graphene*”, **Indian Patent**, being filled, 2020.

Conferences:

1. **Robin Singla**, and Anil Kottantharayil, “*Novel method for graphene hydroxylation*”, **Poster presentation at Graphene- 2019 Conference**, Rome, June 2019.

2. Sanchar Acharya, **Robin Singla**, Anakha V. Babu, R. Abdul Khadar, and Anil Kottantharayil, “*Field effect mobility improvement in CVD graphene by using Local Metal Side-Gate*”, **Poster presentation at Graphene-2019 Conference**, Rome, June 2019.